A Dyson-Schwinger Approach to Finite Temperature QCD

Vom Fachbereich Physik
der Technischen Universität Darmstadt

zur Erlangung des Grades
eines Doktors der Naturwissenschaften
(Dr. rer. nat.)

genehmigte Dissertation von
Dipl.-Phys. Jens Andreas Müller
aus Ottweiler

Darmstadt 2011
D17

Referent: Prof. Dr. Christian Fischer
Korreferent: Prof. Dr. Jochen Wambach

Tag der Einreichung: 16. November 2010
Tag der Prüfung: 15. Dezember 2010

Ein Dyson-Schwinger Zugang zu QCD bei endlichen Temperaturen

Zusammenfassung

Die verschiedenen Phasen der Quantenchromodynamik bei endlicher Temperatur werden untersucht. Zu diesem Zweck wird der nicht-perturbative Quark-Propagator im Matsubara Formalismus über seine Bewegungsgleichung in Form der Dyson-Schwinger Gleichung bestimmt. Es wird ein neuartiges Trunkierungsschema eingeführt, welches den nicht-störungstheoretischen, temperaturabhängigen Gluon-Propagator aus reiner Gittereichtheorie beinhaltet.

Im ersten Teil der Arbeit werden ein confinement-deconfinement Ordnungsparameter, das sogenannte Duale-Kondensat, und die kritische Temperatur aus der Abhängigkeit des Quark-Propagators von den Randbedingungen in zeitlicher Richtung bestimmt. Der chirale Übergang wird mit Hilfe des Quark-Kondensats als Ordnungsparameter untersucht. Desweiteren werden Unterschiede zwischen den Eichgruppen SU(2) und SU(3) am chiralen und deconfinement Übergang erforscht.

Im Folgenden wird der quenched Quark-Propagator bei endlicher Temperatur hinsichtlich einer möglichen Spektraldarstellung studiert. Hierbei zeigt sich, dass die analytischen Eigenschaften des Quark-Propagators unterhalb und oberhalb des deconfinement Übergangs unterschiedlich sind. Dieses Ergebnis motiviert die Betrachtung eines alternativen deconfinement Ordnungsparameters, der Positivitätsverletzung der Spektralfunktion signalisiert. Ein Kriterium für Positivitätsverletzung der Spektralfunktion, welches die Krümmung der Schwinger-Funktion benutzt, wird hergeleitet.

Das mögliche Quasiteilchen-Spektrum wird unter Verwendung einer Auswahl von Ansätzen für die Spektralfunktion hinsichtlich seiner Quarkmassen- und Impulsabhängigkeit analysiert. Die Ergebnisse motivieren eine direktere Bestimmung der Spektralfunktion im Rahmen der Dyson-Schwinger Gleichungen.

In den zwei folgenden Kapiteln werden Erweiterungen des Trunkierungsschemas betrachtet. Der Einfluss dynamischer Quark-Freiheitsgrade auf den chiralen und deconfinement Übergang wird untersucht. Dies dient als erster Schritt in Richtung einer vollständig selbstkonsistenten Behandlung dynamischer Quarkfreiheitsgrade und der Erweiterung zu endlichem chemischen Potential. Die Güte unserer Trunkierung wird zunächst bei verschwindendem chemischen Potential überprüft. Neben guter Übereinstimmung der Übergangstemperaturen mit Gitter-QCD-Rechnungen, ergeben die unterschiedlichen decon-

finement Kriterien des Dualen-Kondensats und der Schwinger-Funktion interessanterweise ähnliche Ergebnisse. Im Anschluss werden die Auswirkungen eines endlichen quarkchemischen Potentials untersucht. Diese Rechnungen erlauben einen ersten Einblick, über Molekularfeld Näherungen phenomenologischer Modelle hinausgehend, auf das Duale-Kondensat bei nichtverschwindendem Potential. Desweiteren wird eine Möglichkeit der Rückkopplung von langreichweitigen Fluktuationen in der Nähe eines Phasenübergangs zweiter Ordnung ausgearbeitet. Im Bereich der skalierenden Lösung ergeben sich aus einer analytischen Untersuchung Nebenbedingungen für eine selbstkonsistente Lösung.

A Dyson-Schwinger approach to finite temperature QCD

Abstract

The different phases of quantum chromodynamics at finite temperature are studied. To this end the nonperturbative quark propagator in Matsubara formalism is determined from its equation of motion, the Dyson-Schwinger equation. A novel truncation scheme is introduced including the nonperturbative, temperature dependent gluon propagator as extracted from lattice gauge theory.

In the first part of the thesis a deconfinement order parameter, the dual condensate, and the critical temperature are determined from the dependence of the quark propagator on the temporal boundary conditions. The chiral transition is investigated by means of the quark condensate as order parameter. In addition differences in the chiral and deconfinement transition between gauge groups SU(2) and SU(3) are explored.

In the following the quenched quark propagator is studied with respect to a possible spectral representation at finite temperature. In doing so, the quark propagator turns out to possess different analytic properties below and above the deconfinement transition. This result motivates the consideration of an alternative deconfinement order parameter signaling positivity violations of the spectral function. A criterion for positivity violations of the spectral function based on the curvature of the Schwinger function is derived.

Using a variety of ansätze for the spectral function, the possible quasi-particle spectrum is analyzed, in particular its quark mass and momentum dependence. The results motivate a more direct determination of the spectral function in the framework of Dyson-Schwinger equations.

In the two subsequent chapters extensions of the truncation scheme are considered. The influence of dynamical quark degrees of freedom on the chiral and deconfinement transition is investigated. This serves as a first step towards a complete self-consistent consideration of dynamical quarks and the extension to finite chemical potential. The goodness of the truncation is verified first at vanishing chemical potential. Interestingly, besides good agreement of the transition temperatures with lattice QCD calculations, the different deconfinement criteria of the dual condensate and of the Schwinger-function yield similar results. In the following, the effects of a finite quark chemical potential are studied. These calculations allow for a first insight on the dual condensate at finite chemical potential beyond mean-field calculations in phenomenological models. In addition, a possibility to

include the back-reaction of long-range fluctuations in the vicinity of a second order phase transition is elaborated. In the scaling region constraints for a self-consistent solution arise from an analytic investigation.

Contents

1 Introduction **1**

2 Aspects of Finite Temperature QCD **6**

2.1 The QCD Partition Function 6
2.2 Global Symmetries 12
2.3 Finite Temperature QCD Phase Transitions 17
2.4 Dyson-Schwinger Equations in the Vacuum 19
2.5 Dyson-Schwinger Equations at Finite T 23

3 Chiral and Deconfinement Transition from the Quark Propagator **31**

3.1 The Dual Quark Condensate 32
3.2 The Truncation Scheme 35
3.3 Numerical Results 41
3.4 Summary 48

4 Quark Spectral Properties above T_c **50**

4.1 Matsubara Propagator below and above T_c 51
4.2 Quark Spectral Function and Representation 53
4.3 Quark Spectral Function at Zero Momentum 55
4.4 Momentum Dependence of the Spectral Function in the Chiral Limit . . . 62
4.5 Summary 66

5 A Hard Thermal Loop Truncation **68**

5.1 The Truncation Scheme 68
5.2 Numerical Results at Vanishing μ_q 71
5.3 Numerical Results at Non-Vanishing μ_q 75
5.4 Summary 80

6 Critical Modes and the Chiral Phase Transition **81**

6.1 Quark Propagator and Pion Effects 82

6.2 Goldstone Modes in QCD 84
6.3 Summary 89

7 Conclusions and Outlook **90**

A Conventions **95**

B Derivation of the Quark DSE **100**

C Gluon Propagator and Quark-Gluon Vertex **102**

D Analytic Expression of the Meson Exchange **106**

E Numerical Implementation **110**

Chapter 1

Introduction

Quantum chromodynamics (QCD) is the theory describing the strong interaction between the nucleon constituents. Confidence for QCD as the correct theory of the strong interaction was gained from the success of perturbative calculations at high energy transfer. The peculiarity of asymptotic freedom [1–3], meaning that the interaction strength tends to zero at small distances, makes these calculations possible. However, at large distances above 0.1 fm the interaction strength becomes strong and perturbation theory fails. A large part of today's fascination in QCD is founded in this nonperturbative, strongly coupled regime which accommodates a large variety of physical phenomena. To these phenomena belong among others the wealth of observable bound state objects, the hadrons, and corresponding hadron observables. The agreement of the hadron spectrum calculated in the framework of lattice QCD with known experimental results indeed confirms the theory also beyond perturbation theory. Nevertheless, details as to how the complex 'macroscopic' physics emerges from the very assessable and plain microscopic description of QCD still remain unclear.

The quantitative derivation of 'macroscopic' physics governed by simple microscopic physical laws is one of the major challenges of theoretical physics. In this respect QCD states a prime example; though, a special role is granted to QCD due to particular properties. One of the most striking is the fact that the only fundamental elements of the theory, the quarks and gluons, are notoriously not directly observable. Moreover, the physical spectrum may only contain color neutral objects and there are no long-range forces. This is referred to as confinement. No less fascinating, QCD provides the mechanism generating 95 percent of the observable mass of the universe. This mechanism of mass generation is the direct consequence of dynamical chiral symmetry breaking, which is besides confinement the other important phenomenon of relevance in this work.

Interestingly, both phenomena, confinement and chiral symmetry breaking, seem to be interlinked. Although the theoretical search in this direction has brought many interesting ideas, the understanding of their connection is still elusive.

Great interest is also dedicated to QCD at finite temperature and chemical potential. For example the physics of the early universe seconds after the Big Bang can almost certainly be described by a hot quark-gluon plasma with low density. On the other hand, the interior of neutron stars is determined by QCD at high densities and low temperatures. Besides these two regimes the domain at moderate chemical potential is probed by experiments at the Relativistic Heavy Ion Collider (RHIC) and in the future at the LHC and by the FAIR facility. Thus, a theoretical description of QCD thermodynamics is highly demanded. A sketch of the QCD phase diagram, as it is expected nowadays, is shown in fig. 1.1. At low temperatures and densities QCD is in the chiral symmetry broken, confining phase with hadron bound states and resonances present. At large enough temperatures and chemical potentials, hadron matter undergoes transitions into a deconfining and approximately chiral symmetric state of quarks and gluons, the quark-gluon plasma. This state is still strongly interacting, as the experiments at RHIC revealed. It is therefore not accessible by perturbation theory. The diagram also indicates possible quark-matter states with superconducting phases at low temperatures and high densities. For investigations of these states and corresponding phase transitions nonperturbative methods are necessary.

Though there are several nonperturbative approaches, these studies turn out to be a difficult task and it seems that combined effort using different methods is a promising possibility. In this thesis, we will apply Dyson-Schwinger equations for QCD correlation functions at finite temperatures. The goal of the thesis is to provide the framework of Dyson-Schwinger equations as a reliable tool for an analysis of the QCD phase diagram at non-vanishing chemical potential. Thereby, the here presented analysis mainly focusing at vanishing chemical potential, constitutes an important intermediate step. In the regime of vanishing chemical potential we can also compare with results from lattice QCD calculations.

Lattice QCD is the formulation of the theory on a finite space-time lattice. In principle it allows the direct ab initio calculation of expectation values. In numerical computations a statistical interpretation of the partition function is necessary. However, the space-time discretization as well as the need of the statistical interpretation lead to apparent limitations of this approach. Important in view of this work is the fact that the statistical interpretation breaks down when considering QCD thermodynamics at finite chemical potential. This can be traced back to the fermion determinant becoming complex and is

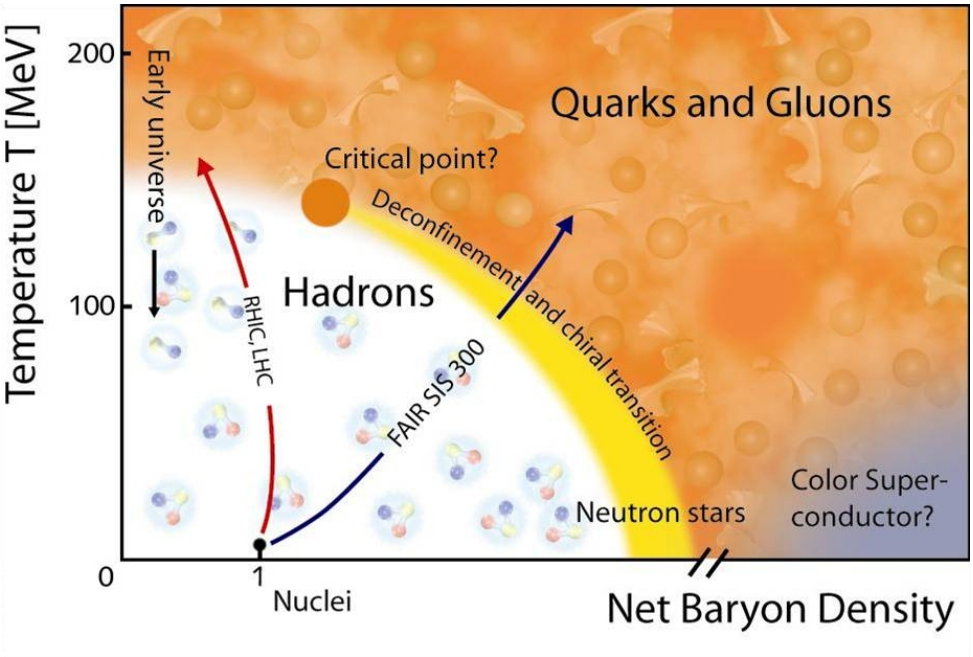

Figure 1.1: Sketch of the QCD phase diagram [4].

referred to as the sign problem. Different methods have been proposed and studied to overcome this problem. One of these is the analytic continuation of calculations performed at imaginary chemical potential [5, 6]. The calculations at imaginary chemical potential can be carried out in the usual way on the lattice since there is no sign problem. Two other approaches are the so-called reweighting method [7, 8] and the Taylor expansion method [8, 9]. However, the reliability of all these approaches is still under discussion and in any case, their applicability is limited to certain parts of the QCD phase diagram, see refs. [10–12].

At vanishing chemical potential lattice QCD simulations ascertained beyond doubt that the chiral and deconfinement transitions correspond to crossover transitions [13, 14]. For a long time there were conflicting results concerning the questions of whether or not both transitions take place in a narrow temperature range and which value one can assign to the crossover temperatures [15–17]. Preliminary results seem to offset these discrepancies largely. From the inflection point of the chiral susceptibilities, chiral crossover temperatures of $T^\chi = 147$ MeV [17] and $T^\chi = 164$ MeV [18] are independently determined. The deconfinement transition temperatures determined from the strange number susceptibility seem to agree even better [17, 18].

Many questions remain however unsolved, in particular when considering finite chemical

potential. Most prominent is the question of the location of the critical point respectively if it even exists [5, 19–22]. Also the nature of the quark-gluon plasma close to the transition temperature is subject of intense investigations [23–27]. Furthermore, the possibility of inhomogeneous phases and so-called quarkyonic phases is under discussion [28–30]. In addressing these questions functional methods which are not affected by the sign problem and whose analytic continuation is possible in principle, might prove powerful.

Dyson-Schwinger equations are successfully applied in phenomenological investigations of hadron observables as well as for fundamental questions concerning confinement in Yang-Mills theory [31–34]. There are also efforts applying them to investigations at finite temperature [35–37]. Usually, parameter model ansätze for the quark-gluon interaction are employed and therefore less can be said about the fidelity of the truncation and the results. In this thesis, we present a truncation scheme at finite temperature which goes beyond simple phenomenological rainbow approximations. This includes important nonperturbative finite temperature effects of gauge theory. The approach serves as a starting point for extensions also regarding the effects of dynamical quark degrees of freedom. A first step in this direction will also be considered here. The thesis is organized as follows:

Basic aspects of QCD with special emphasis on the thermodynamic formulation and associated properties will be reviewed in the next chapter. We discuss chiral symmetry and center symmetry and outline the quark Dyson-Schwinger equation representing our quantity of interest.

Chapter 3 is devoted to the chiral and the deconfinement transition at finite temperature. To this end, we outline our truncation scheme for the quark Dyson-Schwinger equation at finite temperature using SU(2) and SU(3) lattice results for the temperature dependent gluon propagator and a temperature dependent ansatz for the quark-gluon vertex as input. Besides the conventional quark condensate as an order parameter for chiral symmetry, we consider the dual quark condensate as a gauge invariant order parameter for deconfinement. Our results strongly indicate that the mechanism for chiral symmetry restoration in Landau gauge is connected to the nonperturbative, temperature dependent behavior of the electric sector of Yang-Mills theory. Hence, we also locate a link between deconfinement and chiral symmetry since the electric sector is of most relevance for the deconfinement transition.

In chapter 4, we consider a possibility towards the determination of quark spectral functions at finite temperature. We apply a method proposed in refs. [38, 39] utilizing a given shape of the quark spectral function including a few fitting parameters to be determined from the numerical data. As an interesting byproduct we obtain hints for a

strong temperature dependence of the quark-gluon vertex by comparison with the lattice data. Furthermore, we also study analytic properties of the quark propagator above and below the deconfinement transition temperature. Our results show that these analytic properties also distinguish the confining and deconfining phases and thus serve as an alternative deconfinement order parameter.

Extensions of the truncation scheme including dynamical quark effects and critical fluctuations are studied in chapters 5 and 6. We first consider the effects of quark degrees of freedom on the gluon propagator in chapter 5. These constitute an important source of medium modifications and have a strong influence on the nature of the chiral and the deconfinement transitions. In order to demonstrate the capabilities of this approach we also present results at non-vanishing chemical potential. Details of the chiral phase transition in the limit of vanishing quark masses are further investigated in chapter 6. We focus in particular on the role of long-range modes close to a chiral second order phase transition and introduce a truncation including these critical fluctuations.

Our results are summarized in chapter 7 where also stimuli for possible further investigations are outlined.

Part of this work has already been published. Chapter 3 is based on ref. [40]. Note that there exists also an earlier published work on this where we had to rely on less detailed input data [41]. The content of chapter 4 is the subject of ref. [42].

Chapter 2

Aspects of Finite Temperature QCD

The aim of this thesis is to study strongly interacting matter at high temperatures. As a starting point we review some facets of QCD and its properties in thermodynamic equilibrium.

The first part of this chapter summarizes selected aspects of the quantization and renormalization of the theory. We then consider global symmetries of the action and discuss the realization of the theory in phases with different symmetries. The concepts introduced in these sections are also valid for most special unitary gauge groups. We particularly mention the validity for the $SU(2)$ Lie-group which we will also consider in this thesis. In the remaining section of this chapter, we will introduce the Dyson-Schwinger formalism for Green's functions.

2.1 The QCD Partition Function

QCD Lagrangian

The QCD Lagrangian density can be obtained solely from a few fundamental principles. These principles are Poincaré invariance, locality, P and T symmetry, $SU(3)$ gauge symmetry and renormalizability. In a dense notation the resulting QCD Lagrangian density reads

$$\mathcal{L}_{QCD}[\psi, \bar{\psi}, A] = \bar{\psi}\,(i\,\not{D} - m)\,\psi - \frac{1}{2\,g_s^2}\,\mathrm{Tr}_c\,(F_{\mu\nu}\,F^{\mu\nu}) \tag{2.1}$$

where ψ, $\bar{\psi}$ denote the quark fields and $F_{\mu\nu}$ the field strength tensor. We used the abbreviation $\not{D} = \gamma^\mu D_\mu$ with Dirac γ-matrices and the covariant derivative $D_\mu = \partial_\mu + A_\mu$. The coupling constant g_s is absorbed in the gluon field A_μ; it can be restored by replacing A_μ by

$g_s\, A_\mu$. The mass matrix $m = \mathrm{diag}(m_u, m_d, \dots)$ denotes the current-quark masses generated in the electroweak sector. For a gauge transformation the spinors of the quark fields transform under the action of an element in the fundamental representation of $SU(3)$. The gauge fields, A_μ are Lie algebra-valued and thus may be written as $A_\mu = -i\, t^a A^a_\mu$. The generators of the Lie group t^a form an orthonormal set $\mathrm{Tr}_c\,(t^a t^b) = \frac{1}{2}\,\delta_{a\,b}$. The field strength tensor $F_{\mu\nu}$ is defined in analogy to the Riemann curvature tensor by

$$F_{\mu\nu} = [D_\mu, D_\nu] = -i\, t^a F^a_{\mu\nu}\,. \tag{2.2}$$

Partition function

The partition function of a canonical ensemble qualifies to describe a quantum many-particle system in thermodynamic equilibrium. With a complete set of orthonormal states $|n\rangle$ it is given by

$$\mathcal{Z} = \mathrm{Tr}\, e^{-\beta \hat{H}} = \sum_n \langle n|e^{-\beta \hat{H}}|n\rangle \tag{2.3}$$

with the inverse temperature $\beta = 1/(k_B\, T)$ and the Hamiltonian $\hat{H}$. We use a common unit convention with the Boltzmann factor k_B set to one and consider in the following scalar particles for simplicity. A grand canonical ensemble takes into account also conserved quantities $\mathcal{N}_i$. This is done by replacing $\exp[-\beta\, \hat{H}]$ with $\exp[-\beta\,(\hat{H} - \sum_i \mu_i\, \mathcal{N}_i)]$ where μ_i are the chemical potentials. To obtain a functional integral representation of the partition function, one may compare the Boltzmann factor $\exp(-\beta \hat{H})$ with the time-evolution operator $\exp(-i\hat{H}t)$. This yields a correspondence of the partition function with an evolution in imaginary time $t = -i\beta$. Thus a functional integral representation of the partition function can be received from the path integral representation of

$$\langle \varphi'|e^{-i\hat{H}t'}|\varphi\rangle = \int [d\varphi]\, \exp\left(i \int_0^{t'} dt\, d^3x\, \mathcal{L}(t)\right) \tag{2.4}$$

by analytic continuation to imaginary time $t' \to -i\beta$. Here $\mathcal{L}(t)$ is the Lagrangian density, $|\varphi\rangle$, $\langle\varphi'|$ denote coherent states and the boundary condition $\varphi(t=0) = \varphi$ and $\varphi(t) = \varphi'$ has to be considered. Performing the analytic continuation $t \to -i\tau$ with $0 \le \tau \le \beta$ and taking the trace provides

$$\mathcal{Z} = \int_{\mathrm{PBC}} [d\varphi]\ \ \exp\left(-\int_0^{\beta} d\tau d^3x\ \mathcal{L}_E\right) \tag{2.5}$$

with the Euclidean Lagrangian defined by $\mathcal{L}_E = -\mathcal{L}(t = -i\tau)$. The subscript PBC denotes the implementation of the periodic boundary conditions $\varphi(\tau = \beta) = \varphi(\tau = 0)$ in

the τ-direction due to the trace. The preceding result can also be applied to fermions. In this case the trace over the anti-commuting fermion fields yields anti-periodic boundary conditions $\psi(\tau = \beta) = -\psi(\tau = 0)$.

For the QCD partition function we then find

$$\mathcal{Z}[J_\mu, \bar{\eta}, \eta] = \int [d\psi d\bar{\psi} dA] \exp\Big\{ - \mathcal{S}_E[\bar{\psi}, \psi, A_\mu] + \int_0^\beta d\tau d^3x \, (A^a_\mu J^a_\mu + \bar{\eta}\psi + \bar{\psi}\eta) \Big\} \quad (2.6)$$

with the Euclidean action

$$S_E[\bar{\psi}, \psi, A_\mu] = \int_0^\beta d\tau d^3x \, \mathcal{L}_E = \int_0^\beta d\tau d^3x \left\{ \bar{\psi}(-i\not{D} + m)\psi + \frac{1}{2\, g_s^2} \mathrm{Tr}_c \, (F_{\mu\nu} F_{\mu\nu}) \right\}. \quad (2.7)$$

Here, the gluons obey periodic boundary conditions $A_\mu(\tau) = A_\mu(\tau + \beta)$ and the quarks anti-periodic boundary conditions $\psi(\tau) = -\psi(\tau + \beta)$. We also introduced Grassmann valued source terms $\bar{\eta}$, η for the fermions and a source term J^a_μ for the gauge fields. In writing eq. (2.7) we used Euclidean conventions $\gamma^0 \to -i\gamma_4$, $A_0 \to -iA_4$ and $\not{D} = \gamma_\mu D_\mu$ (μ, $\nu = 1, \ldots, 4$) which yields (see appendix A for details)

$$\{\gamma_\mu, \gamma_\nu\} = -2\delta_{\mu\,\nu} \quad \text{and} \quad D_\mu = \partial_\mu - A_\mu \,. \quad (2.8)$$

From now on we will work in Euclidean space-time also when we refer to the vacuum theory.

Gauge fixing

Gauge symmetry, i.e invariance of the Lagrangian density under gauge transformations

$$\begin{array}{rcl} A & \longrightarrow & A^{(g)} = g A_\mu g^\dagger - (\partial_\mu g) g^\dagger \\ \psi & \longrightarrow & \psi^{(g)} = g\psi \end{array} \quad ; \qquad g(x) \in SU(N_c)$$

is the guiding principle for the construction of the action (2.7). The set of potentials $A^{(g)}$ emerging from A by a gauge transformation forms a gauge orbit: $\mathcal{O} = \{A^{(g)} \mid g \in SU(N_c)\}$. Potentials from one gauge orbit are physically the same. In the way the partition function is written in (2.6) the functional integration extends also over such physically equivalent potentials. Thus the expression (2.6) is of practical use only if expectation values of gauge invariant quantities are calculated without relying on gauge variant quantities. The explicit evaluation of the functional integral on a space-time lattice provides such a possibility. Many methods however, as for instance perturbation theory and functional methods need gauge variant quantities, such as propagators as an intermediate step for the calculation of physical observables. One therefore needs to

constrain the integration over the gauge fields to one representative out of the physically equivalent fields. This is done by imposing a condition on the gauge fields (gauge fixing condition)

$$f^a(A) - \omega^a(x) = 0 \tag{2.9}$$

where the function ω^a is arbitrary and independent of A.[1] The gauge fixing condition can be implemented in the functional integral via the Fadeev-Popov method. For the linear covariant condition $f^a(A) = \partial_\mu A^a_\mu$ the Fadeev-Popov quantization yields

$$\begin{aligned}\mathcal{Z}[J,\sigma,\bar{\sigma},\bar{\eta},\eta] = \int [d\psi d\bar{\psi} dA dc d\bar{c}] \\ \exp\Big(- \int d\tau d^3x \left\{ \mathcal{L}_{E,\alpha} - (A^a_\mu J^a_\mu + \bar{\eta}\psi + \bar{\psi}\eta + \bar{\sigma}^a c^a + \bar{c}^a \sigma^a) \right\} \Big)\end{aligned} \tag{2.10}$$

with

$$\begin{aligned}\mathcal{L}_{E,\alpha} &= \mathcal{L}_E + \frac{1}{2g_s^2\alpha}(\partial_\mu A_\mu)^2 + (\partial_\mu \bar{c}^a)\, D^{ac}_\mu\, c^c \\ &= \bar{\psi}(-i\not{D} + m)\psi + \frac{1}{2g_s^2}\mathrm{Tr}_c(F_{\mu\nu}F_{\mu\nu}) + \frac{1}{2\alpha g_s^2}(\partial_\mu A^a_\mu)^2 - (\partial_\mu \bar{c}^a)\, D^{ac}_\mu\, c^c\,.\end{aligned} \tag{2.11}$$

We introduced the Lie algebra-valued ghost fields c^a and $\bar{c}^a$ which are anti-commuting spin-zero fields. They do not obey the spin-statistics theorem and cannot be related to physical particles. The differential operator D^{ab} is the covariant derivative for the adjoint representation. The condition (2.9) with $f^a(A) = \partial_\mu A^a_\mu$ is reflected in the term $(\partial_\mu A^a_\mu)^2/(2\alpha g_s^2)$ with an additional parameter α. We work in Landau gauge, i.e. $\alpha = 0$ and thus the gauge fields have to rigorously obey $\partial_\mu A_\mu = 0$.

For completeness we mention that the gauge-fixed action (2.11), though no longer invariant under local gauge transformations, possesses the so-called BRST-symmetry and is still invariant under global gauge transformations. The BRST transformations are essentially gauge transformations with the gauge parameter replaced by the ghost field c. Global gauge symmetry and BRST-symmetry are the remnants of local gauge symmetry and play a vital role in considerations with regard to formal confinement criteria of vacuum QCD.

[1] In general the gauge fixing condition should be chosen such that it is fulfilled exactly once on each gauge orbit. In a non-Abelian theory this cannot be established by a local condition as noted by Singer and leads to the problem of Gribov copies.

Renormalization

The theory defined by the action (2.11) is multiplicatively renormalizable. This implies that the UV-divergences can be absorbed by a finite number of renormalization constants. Furthermore the divergences occur only in monomials already present in the initial Lagrangian (2.11). This can be shown by means of the Ward-Takahashi identities for BRST-symmetry. Thus multiplying the composite field and coupling terms of the unrenormalized Lagrangian with arbitrary renormalization parameters yields the renormalized Lagrangian given by

$$\begin{aligned}\mathcal{L}_{E,\alpha} &= Z_2\,\bar{\psi}(-i\partial\!\!\!/ + Z_m\,m)\psi + Z_{1F}\,g_s\,\bar{\psi}\gamma_\mu t^a \psi A^a_\mu + \frac{Z_3}{4}(\partial_\mu A^a_\nu - \partial_\nu A^a_\mu)^2 \\ &\quad + \frac{Z_1\,g_s}{2}\,f^{abc}\,A^b_\mu A^c_\nu(\partial_\mu A^a_\nu - \partial_\nu A^a_\mu) + \frac{Z_4\,g_s^2}{4}\,f^{abc}\,f^{ade}\,A^b_\mu A^c_\nu A^d_\mu A^e_\nu \\ &\quad - \tilde{Z}_3(\partial_\mu \bar{c}^a)\,(\partial_\mu c^a) + g_s\,\tilde{Z}_1\;f^{abc}(\partial_\mu \bar{c}^a)A^b_\mu c^c + \frac{\lambda}{2\alpha}(\partial_\mu A^a_\mu)^2\,. \end{aligned} \tag{2.12}$$

We restored the coupling constant g_s by $A^a_\mu \to g_s\,A^a_\mu$ which is convenient for discussing multiplicative renormalizability. The quark sector is of main interest in this thesis therefore we will later concentrate on the rescaling transformations

$$\bar{\psi}\psi \to Z_2\bar{\psi}\psi \qquad m_{bare} \to Z_m m_R \qquad g_{s,bare}\bar{\psi}A\!\!\!/\psi \to Z_{1F}g_{s,R}\,\bar{\psi}A\!\!\!/\psi \tag{2.13}$$

with the quark wave function Z_2, the mass renormalization constant Z_m and the quark-gluon vertex renormalization constant Z_{1F}. In addition six more constants Z_3, Z_1, Z_4, $\tilde{Z}_3$ and λ occur in the Yang-Mills and gauge-fixing term. In the classical theory the gauge principle restricts the coupling constant g_s to be the same in all interaction terms. In the gauge-fixed theory the gauge symmetry is reflected in BRST-invariance which relates the seven renormalization factors Z_1, Z_2, Z_3, Z_4, $\tilde{Z}_1$, $\tilde{Z}_3$, Z_{1F} by

$$\frac{Z_4}{Z_1} = \frac{Z_1}{Z_3} = \frac{\tilde{Z}_1}{\tilde{Z}_3} = \frac{Z_{1F}}{Z_2}\,. \tag{2.14}$$

It follows that consistency is obtained when introducing a coupling rescaling transformation $g_{s,bare} \to Z_g\,g_{s,R}$ since then the interaction terms rescale according to their coupling and field content

$$\tilde{Z}_1 = Z_g\,\tilde{Z}_3\,Z_3^{1/2}\,, \qquad Z_{1F} = Z_g\,Z_2\,Z_3^{1/2}\,, \qquad Z_1 = Z_g\,Z_3^{3/2}\,, \qquad Z_4 = Z_g^2\,Z_3^2 \tag{2.15}$$

with relations (2.14) preserved. This shows that BRST-symmetry constrains the coupling constants of all interaction terms to rescale in the same way.

Correlation functions

In the following φ_i may combine the set of fields present in an action and the index i labels the different fields, e.g. for QCD $\varphi_i = \{A^a_\mu, \bar{c}^a, c^a, \bar{\psi}, \psi\}$. We denote expectation values of products of field operators as correlation, Green's or n-point functions: $C^{(i,j,\ldots,k)}(x_1, x_2, \ldots, x_n) = \langle T_\tau \; \varphi_i(x_1)\, \varphi_j(x_2) \ldots \varphi_k(x_n)\rangle$. The symbol T_τ denotes 'time'-ordering. These functions encode all of the physics of the quantum theory and they constitute the basis of the functional approach applied in this thesis. Connected n-point functions can be generated from the functional $W[J] := \ln Z[J]$ by successive differentiation:

$$\langle T_\tau \; \varphi_i(x_1)\, \varphi_j(x_2) \ldots \varphi_k(x_n)\rangle_c = \frac{\delta}{\delta J_i(x_1)} \frac{\delta}{\delta J_j(x_2)} \cdots \frac{\delta}{\delta J_k(x_n)} W[J]\bigg|_{J=0} \tag{2.16}$$

where J_i denotes the sources associated to the fields. The Legendre transform of $W[J]$ yields the effective action:

$$\Gamma[\Phi] := \sup_J \left(-W[J] + \int J\Phi \right) . \tag{2.17}$$

Here $J = J[\Phi]$ is chosen as the supremum of $\int J\Phi - W[J]$, i.e. as the inversion of $\Phi_i[J] = (\delta\, W[J])/(\delta J_i)$. The effective action is a functional of the field expectation values $\Phi_i = \langle \varphi_i \rangle$ and generates the 1PI Green's functions by differentiation with respect to Φ_i:

$$\langle T_\tau \; \varphi_i(x_1)\, \varphi_j(x_2) \ldots \varphi_k(x_n)\rangle_{1\mathrm{PI}} = \frac{\delta}{\delta\Phi_i(x_1)} \frac{\delta}{\delta\Phi_j(x_2)} \cdots \frac{\delta}{\delta\Phi_k(x_n)} \Gamma[\Phi]\bigg|_{\Phi^0} . \tag{2.18}$$

The expression has to be evaluated at

$$\Phi^0_i = \frac{\delta W}{\delta J_i}\bigg|_{J=0} \tag{2.19}$$

for vanishing external sources.

In the course of the renormalization process a regulator, e.g. a high momentum cutoff Λ, is introduced to make otherwise divergent quantum corrections to n-point functions finite. The unrenormalized respectively bare Green's functions calculated from the regularized integrals depend on the cutoff parameter Λ. The renormalized Green's functions should be independent of Λ but will depend on a renormalization scale μ, respectively the values of the physical parameters at this scale. The physical parameters at the scale μ are input parameters determined from experiment. The renormalization constants introduced in this section relate the unrenormalized Λ dependent Green's functions to the renormalized ones and the bare parameters to the physical parameters. We denote in the following the

connected n-point functions by G and the 1PI n-point functions by Γ. That is to say $G^{(n,m,l)}$ ($\Gamma^{(n,m,l)}$) is the connected (1PI) Green's function with n quark fields, m gluon fields and l ghost fields. Then the relations between the renormalized and the bare Green's functions read

$$G_R^{(n,m,l)}(\mu) = Z_2^{-n/2}(\mu,\Lambda)\, Z_3^{-m/2}(\mu,\Lambda)\, \tilde{Z}_3^{-l/2}(\mu,\Lambda)\; G_{bare}^{(n,m,l)}(\Lambda)\,, \tag{2.20}$$

$$\Gamma_R^{(n,m,l)}(\mu) = Z_2^{n/2}(\mu,\Lambda)\, Z_3^{m/2}(\mu,\Lambda)\, \tilde{Z}_3^{l/2}(\mu,\Lambda)\; \Gamma_{bare}^{(n,m,l)}(\Lambda)\,. \tag{2.21}$$

For simplicity we only specified the cutoff and renormalization scale dependence of the correlators and omitted momentum or space-time arguments. Renormalization constants at different renormalization points or cutoffs obey $Z_i(\mu_1,\mu_3) = Z_i(\mu_1,\mu_2)Z_i(\mu_2,\mu_3)$.

Finally we will mention two peculiarities of Landau gauge making it particularly interesting for numerical investigations in nonperturbative functional approaches. The ghost-gluon vertex is not divergent in Landau gauge and it is possible to choose $\tilde{Z}_1 = 1$. Furthermore, since $\partial_\mu A_\mu = 0$ is not affected by a rescaling of the fields, Landau gauge constitutes a renormalization group fixed point.

2.2 Global Symmetries

Chiral symmetry

For vanishing quark masses the matter sector of (2.7) possesses chiral symmetry. In nature this symmetry is explicitly broken by the electroweak interactions generating quark masses. However the light quark masses, being of the order of a few MeV, are small compared to the relevant scale of the strong interaction which is of the order of 1 GeV. For such a small explicit chiral symmetry breaking one would expect approximate chiral symmetry to hold and to find almost degenerate parity partners in the meson spectrum. A prominent counterexample is the mass splitting of the ρ ($m_\rho = 0.77$ GeV) and the a_1 ($m_{a1} = 1.26$ GeV). Chiral symmetry is broken in many ways and its symmetry breaking pattern plays an important role for the understanding of QCD at low energies.

We introduce the left-handed and right-handed Weyl spinors

$$\psi_L = \frac{1-\gamma^5}{2}\,\psi\,, \qquad \psi_R = \frac{1+\gamma^5}{2}\,\psi\,.$$

Then the quark part of the QCD Lagrangian (2.11) with N_f flavors can be decomposed as

$$\bar{\psi}(-i\not{D}+m)\psi = \bar{\psi}_L(-i\not{D})\psi_L + \bar{\psi}_R(-i\not{D})\psi_R + \bar{\psi}_L m\psi_R + \bar{\psi}_R m\psi_L \tag{2.22}$$

where m is a diagonal $N_f \times N_f$ matrix. For $m = 0$, it is evident that left- and right-handed quarks do not mix and the resulting Lagrangian is invariant under global $U_L(N_f) \times U_R(N_f)$ transformations. In view of the symmetry breaking pattern it is convenient to define axial- and vector-transformations acting on ψ, which generate the currents

$$\begin{aligned} J_\mu &= \bar{\psi}\,\gamma_\mu\,\psi\,, \\ J^5_\mu &= \bar{\psi}\,\gamma_\mu\gamma_5\psi\,, \\ J^a_\mu &= \bar{\psi}\,\gamma_\mu\frac{t^a}{2}\psi\,, \\ J^{5a}_\mu &= \bar{\psi}\,\gamma_\mu\gamma_5\frac{t^a}{2}\psi\,, \end{aligned} \tag{2.23}$$

where t^a denotes generators of $SU(N_f)$ subgroups. In the chiral limit these currents are conserved on the classical level. The underlying symmetry is $SU_A(N_f) \times SU_V(N_f) \times U_A(1) \times U_B(1)$. Several effects however break this symmetry and spoil current conservation.

- The quark masses generated by the electroweak interaction break the symmetry explicitly. For equal masses $m = m_0\mathbb{1}$ only axial symmetries are broken and the unbroken subgroup is $SU_V(N_f) \times U_B(1)$.

- Differing masses ($m = \mathrm{diag}(m_u, m_d, \dots)$) in addition also break $SU_V(N_f)$.

- Quantizing the theory breaks axial $U_A(1)$ symmetry explicitly even in the chiral limit. This is due to an anomalous term arising from a non-trivial transformation of the functional integration measure. As an important outcome the $U_A(1)$ anomaly provides an explanation [2] for the mass of the η'.

- In addition chiral symmetry is spontaneously broken. This is effected by gluon interactions generating quark masses dynamically. Note that spontaneous chiral symmetry breaking in QCD has to preserve vector-like symmetries according to a theorem of Vafa and Witten [43].

The dynamical quark mass generation and the $U_A(1)$-anomaly break chiral symmetry strongest. The pattern of this strong symmetry breaking explains the existence of eight pseudo-Goldstone bosons and the relatively large η' mass. It is furthermore in agreement

[2] Interestingly enough the conventional explanation relies on the non-Abelian nature of the gauge fields breaking the symmetry. In fact the anomaly term can be written as a total divergence and therefore only certain gauge transformations, associated with instantons, contribute to the charge [44].

with low-energy relations like PCAC and Goldberger-Treiman and is the sound basis for low-energy effective theories.

Including explicit symmetry breaking terms the divergences of the currents (2.23) is given by

$$\begin{aligned}
\partial_\mu J_\mu &= 0\,, \\
\partial_\mu J^5_\mu &= 2i\,\bar{\psi}\,m\,\gamma_5\,\psi + \frac{N_f}{8\pi^2}\,\mathrm{Tr}_c\,(F_{\mu\nu}\tilde{F}_{\mu\nu})\,, \\
\partial_\mu J^a_\mu &= i\bar{\psi}\left[m, \frac{t^a}{2}\right]\psi\,, \\
\partial_\mu J^{5a}_\mu &= i\bar{\psi}\,\gamma_5\left\{m, \frac{t^a}{2}\right\}\psi\,.
\end{aligned} \tag{2.24}$$

The current J_μ associated with the $U_B(1)$ transformation is the only current not affected by explicit symmetry breaking terms. In the case of degenerate masses, J^a_μ is also conserved since the commutator vanishes.

In close analogy to the transition of magnetic materials from ferro-magnetism to para-magnetism there is a transition from the spontaneously chiral symmetry broken phase to a chiral restored phase when raising the temperature. The quantity in QCD analogous to the magnetization, is the chiral condensate defined by $\langle\bar{\psi}\psi\rangle$. It transform non-trivially under $SU_L(N_f)\times SU_R(N_f)$ and defines an order parameter for chiral symmetry restoration. The chiral condensate is non-vanishing below the critical temperature

$$\langle\bar{\psi}\psi\rangle \neq 0,\ T < T_c \tag{2.25}$$

and vanishes above the critical temperature in the chiral limit ($m \to 0$)

$$\langle\bar{\psi}\psi\rangle = 0,\ T \geq 0\,. \tag{2.26}$$

We discuss this asymptotic symmetry restoration in more detail in the next section.

Center symmetry

The gauge transformed expressions of fields transforming in the adjoint representation are independent of a change of the gauge transformation by an element of the center of the gauge group. This invariance is the basis of center symmetry of pure gauge theory. To discuss this symmetry at finite temperature we recall that the gauge fields obey periodic boundary conditions

$$A_\mu(\tau) = A_\mu(\tau + \beta)\,. \tag{2.27}$$

The boundary condition must certainly not be affected by local gauge transformations

$$A_\mu^{(g)} = g A_\mu \, g^{-1} - (\partial_\mu \, g) g^{-1} \tag{2.28}$$

with $g \in SU(N_c)$ space-time dependent. Besides periodic gauge transformations there are further gauge transformations satisfying this requirement. These can be written as

$$g(\tau, \vec{x}) = \boldsymbol{z} \, g(\tau + \beta, \vec{x}) \tag{2.29}$$

where $\boldsymbol{z}$ is an element of the center of the gauge group Z_{N_c}. The elements of Z_{N_c} are given by $\boldsymbol{z} = \{\mathbb{1}z \equiv \mathbb{1}\exp((2\pi \, k \, i)/N_c) : \; k = 0, \ldots, N_c - 1\}$ and commute with all other elements of the group. Working out a gauge transformation of the type (2.29)

$$A_\mu^{(g)}(\tau + \beta) = \boldsymbol{z}^{-1} \, A_\mu^{(g)}(\tau) \, \boldsymbol{z} \tag{2.30}$$

and requiring periodic boundary conditions we find the commuting feature to be the defining property of $\boldsymbol{z}$. Furthermore the action and the measure of the Yang-Mills functional integral are invariant under gauge transformations (2.29). Hence we may equally allow for these gauge transformations.

The symmetry is explicitly broken in the presence of dynamical fermion fields. Fermions obey anti-periodic temporal boundary conditions

$$\psi(\tau + \beta) = -\psi(\tau) \, . \tag{2.31}$$

These would be altered under center gauge transformations

$$\psi^{(g)}(\tau + \beta) = -\boldsymbol{z}^{-1} \, \psi^{(g)}(\tau) \text{ with } \boldsymbol{z} \neq \mathbb{1} \tag{2.32}$$

where $\psi^{(g)} = g\psi$ denotes the gauge transformed fields. Center symmetry is therefore only an exact symmetry in the absence of dynamical quark fields, respectively $m \to \infty$. Apparently this is the opposite limit then for exact chiral symmetry $m \to 0$.

Much of the motivation to study the center symmetry of $SU(N_c)$ gauge theories lies in its connection to quark confinement in QCD. The presence of center symmetry signals confinement of quarks whereas the spontaneous breaking of center symmetry at high temperatures implies deconfinement. To investigate center symmetry breaking we are interested in a quantity that transforms non-trivially under center transformations. Such a quantity that also clarifies the connection to quark confinement is the Polyakov loop

$$L(\vec{x}) \;\; = \;\; \frac{1}{N_c} \mathrm{Tr}_c \, \mathcal{P} \exp\!\left(\int_0^\beta d\tau \, A_4(\vec{x}, \tau) \right) \tag{2.33}$$

with the symbol $\mathcal{P}$ indicating path ordering. Under a center transformation (2.29) the Polyakov loop is not invariant and picks up a factor:

$$L(\vec{x}, A_4^{(g)}) = z^{-1} L(\vec{x}, A_4)\,. \tag{2.34}$$

The expectation value of the Polyakov loop can be interpreted as

$$\langle L(\vec{x}) \rangle \sim \exp(-\beta F_q) \tag{2.35}$$

where F_q denotes the free energy of an infinitely heavy test quark. A vanishing Polyakov loop is therefore equivalent to an infinite amount of free energy of the test quark and in this respect to quark confinement. In pure $SU(N_c)$ gauge theories a phase transition occurs from a center symmetric, confining phase at low temperatures to a center symmetry broken, deconfining phase at high temperatures. Thus the Polyakov loop is vanishing below the critical temperature

$$\langle L(\vec{x}) \rangle = 0,\ T < T_c\,, \tag{2.36}$$

and non-vanishing above the critical temperature

$$\langle L(\vec{x}) \rangle \neq 0,\ T > T_c\,. \tag{2.37}$$

It is also non-vanishing in the presence of dynamical fermions due to explicit breaking. Since center symmetry is a discrete symmetry Goldstones theorem does not apply.

We note that center symmetry is still present after covariant gauge fixing. To understand this it is convenient to classify the gauge transformations according to their periodicity: $g^z \in SU(N_c)$ with $g^z(\tau) = z\, g^z(\tau + \beta)$. The set of gauge transformations g^z generates a sub-orbit $\mathcal{O}^z$ of the gauge orbit $\mathcal{O}$. It is clear that the Polyakov loop operator stays the same within one sub-orbit but differs by a center element on different sub-orbits. Center symmetry remains as a residual, global symmetry in case of gauge fixing conditions that stay within one sub-orbit thus singling out one representative from each $\mathcal{O}^z$ rather than from $\mathcal{O}$. The center transformations then relate representatives from different sub-orbits, respectively representatives with Polyakov loops differing by z.

As a last comment in this section we stress that one should carefully distinguish between different confinement criteria. Throughout this work we consider the presence of center symmetry and thus infinite quark free energy as confinement. In chapter 5 we will in addition see that the realization of confinement via the violation of reflection positivity is in agreement with this. In contrast, there are other confinement scenarios like e.g. the Kugo-Ojima confinement scenario [45, 46]. In this scenario the physical Hilbert space is

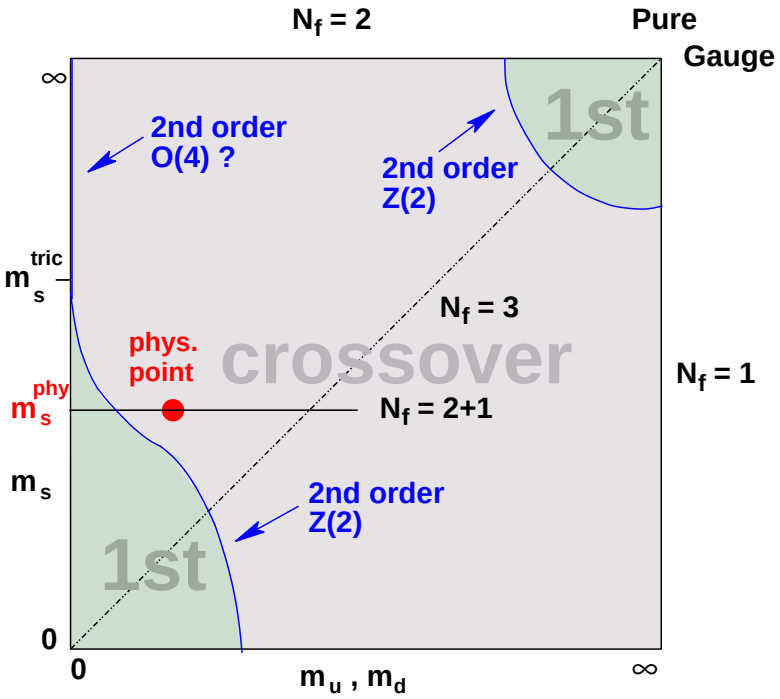

Figure 2.1: Expected phase diagram at vanishing quark chemical potential taken from Ref. [47]. The location of the tri-critical strange quark mass, above or below the physical strange quark mass, is among other questions not yet settled [48].

confined to a state space containing only colorless states in the first place. The relationship between different confinement scenarios and their different implications is certainly an interesting issue but we will not discuss this further.

2.3 Finite Temperature QCD Phase Transitions

In this section we review aspects of the chiral and the deconfinement transitions. Their quark mass and flavor dependencies lead to a rich and complex phase structure and yield new insight about chiral symmetry, confinement and their interplay. The main features at vanishing quark chemical potential are summarized in the so-called Columbia plot in fig. 2.1. The plot shows chiral and deconfinement phase transitions at the same time. The gray area and the blue line in the left part of the diagram, i.e. light up and down quark masses, refer to the chiral phase transition whereas the upper right part concerns the deconfinement phase transition.

Chiral phase transition

The general pattern of chiral symmetry restoration as shown in fig. 2.1 was first exposed by Pisarski and Wilczek [49] employing the universality argument. This argument allows us to consider simple models instead of QCD. Furthermore as an important prerequisite $SU(N_f)_{L+R} \to SU_L(N_f) \times SU_R(N_f)$ symmetry restoration is considered. This implicitly assumes that temperature effects in the $U_A(1)$ anomaly can be neglected which however might not be the case. Though, assuming this, one expects a crossover for a single massless quark, a first order phase transition for three degenerate chiral flavors and a second order phase transition in the case of two massless flavors. The region of the first order transition for three light quarks ends at a second order phase transition line. The second order phase transition line belongs to the Ising universality class with $Z(2)$ symmetry [50]. The location of this line in terms of quark masses is however less ascertained. The phase transition for $N_f = 2$ chiral quarks is suggested to be a second order phase transition with $O(4)$ critical behavior. This result strongly relies on the symmetry group $SU_L(2) \times SU_R(2) \simeq O(4)$ spontaneously breaking to $SU(2)_{L+R} \simeq O(3)$, as already noted in [49]. Assuming for example effective $U_A(1)$ restoration at temperatures below or close to the chiral critical temperature would rather lead to a first order phase transition. The reason is that the pseudo-scalar flavor singlet meson which would obtain a topological mass from the $U_A(1)$ anomaly, in this case becomes very light and drives the transition first order. Although a first order transition could not be settled unequivocally [51] also the $O(4)$ critical behavior has not been proved reliable, see [48] and references therein. The transition of the $O(4)$ critical line to the $Z(2)$ critical line is located at the tri-critical strange quark mass m_s^{tric}. It is an interesting and yet unresolved question as to where the tri-critical point[3] is located, and respectively whether it even exists [48].

Deconfinement phase transition

In the absence of quarks (respectively in the limit of infinitely heavy quarks) there is a first order phase transition in SU(3) gauge theory. This is signaled in the upper right part of fig. 2.1 and is safely confirmed by lattice gauge theory computations [52]. The first order deconfinement phase transition region ends at a second order deconfinement phase transition line lying in the $Z(2)$ universality class. The appropriate model is the three state Potts model with a complex scalar field and invariance under $2\pi/3$ rotations in the complex plane. In addition, we also consider SU(2) gauge group in this thesis. Recall that the discussion of the Polyakov loop order parameter in the previous section does not

[3] At the tricritical point the universality class is mean field.

rely on the number of colors. The phase transition for SU(2) gauge theory is second order in the universality class of the $Z(2)$-Ising model [53–55]. The transition is inverted in the Ising model in the sense that whereas the Ising model is in the symmetry broken phase at low temperatures, SU(2) gauge theory is $Z(2)$ center symmetric at low temperatures and vice versa at high temperatures.

At intermediate values of the quark masses the transitions are crossovers rather than strict phase transitions. The physical quark mass values are expected to lie in the crossover regime. Nevertheless the would be order parameters, the chiral condensate and the Polyakov loop show a rapid change in some narrow temperature range. As already mentioned in the introduction the transition temperatures are stated with $T^{\chi} = 147$ MeV [17] respectively $T^{\chi} = 164$ MeV [18] for the chiral transition and $T_{\text{dec}} \sim 165$ MeV [17, 18] for the deconfinement transition.

Roberge-Weiss periodicity

We briefly discuss the Roberge-Weiss periodicity. In the deconfined phase of pure SU(N_c) gauge theory there are N_c degenerate vacua. These differ from each other by their Polyakov loop value, i.e. by a center element. The inclusion of dynamical quarks singles out one ground state by tilting the potential in one direction whereas the others remain metastable. In this case, the true ground state is the one with a real valued Polyakov loop expectation value. However, it can be shown that a center transformation transferring from one vacuum to another is identical to an imaginary quark chemical potential μ_I where the value $\mu_I = 2\pi kT/N_c$ is determined from the center transformation [56]. Hence, there is periodicity in μ_I with period $\mu_I = 2\pi T/N_c$. Due to the potential barrier between the minima in the deconfining phase the transition is first order with a critical value $\mu_I^c = \pi T/N_c$. At low temperatures the transition is a smooth crossover [5, 56].

2.4 Dyson-Schwinger Equations in the Vacuum

So far we discussed general aspects of finite temperature QCD. We motivated a gauge-fixed expression for the partition function which is appropriate for our purposes. Next we introduce the Dyson-Schwinger equations (DSE). These may be interpreted as the equations of motion for exact propagators and exact vertices. The DSE's correspond to a functional, continuum approach to the quantum theory beyond perturbation theory. As an introduction we will first discuss the quark propagator Dyson-Schwinger equation (qDSE) in the vacuum.

Dyson-Schwinger equations

DSE's can be derived from the assumption that the functional integral of a derivative vanishes

$$0 = \int [d\varphi] \, \frac{\delta}{\delta \varphi} \exp\left[- S[\varphi] + \int J\varphi \right] . \tag{2.38}$$

A rearrangement yields the following expression (see appendix B for details)

$$\frac{\delta \Gamma}{\delta \Phi_i}[\Phi] = \frac{\delta S}{\delta \varphi_i}\left[\varphi_j \to \left(\frac{\delta^2 W}{\delta J_j \delta J_k} \right) \frac{\delta}{\delta \Phi_k} + \Phi_j \right] . \tag{2.39}$$

which is advantageous to obtain the DSE's for 1PI correlation functions. The indices i, j, k collect space-time degrees of freedom, color degrees of freedom, Dirac and vector indices and may also denote different fields. Summation over k is carried out. We indicated that the argument φ_j is replaced by $\frac{\delta^2 W}{\delta J_j \delta J_k} \frac{\delta}{\delta \Phi_k} + \Phi_j$. The connected two-point functions $\frac{\delta^2 W}{\delta J_j \delta J_k} = \langle T_\tau \varphi_j \varphi_k \rangle_c^J$ are considered in the presence of the source J. Arbitrary 1PI correlators are obtained from (2.39) by further differentiation with respect to the fields and then setting the sources to zero. For a general interacting QFT the DSE's of n-point functions yield integral equations containing (n+1)-point vertices and/or higher correlators. Hence one receives an infinite tower of coupled integral equations that needs to be truncated at a certain level. We note that perturbation theory is obtained by truncating the equations at the appropriate loop level.

Quark Dyson-Schwinger equation

The full quark propagator is defined as the second derivative of the effective action evaluated at the expectation values of the fields for vanishing sources:

$$S(x,y) \equiv \langle T \, \psi(x) \bar{\psi}(y) \rangle_c = \left(\frac{\delta^2 \Gamma}{\delta \Psi(y) \delta \bar{\Psi}(x)} \bigg|_{\Phi^0} \right)^{-1} . \tag{2.40}$$

From eq. (2.21) we find that the renormalized and unrenormalized quark propagators are related by

$$S(p;\Lambda) = Z_2(\mu, \Lambda) \, S(p;\mu) \tag{2.41}$$

where Λ denotes the cutoff parameter and μ the renormalization point. We also transformed to momentum space. The DSE for the full, renormalized quark propagator is given by (see appendix B for details)

$$S^{-1}(p;\mu) = Z_2(\mu, \Lambda) \, S_0^{-1}(p;\Lambda) + \Sigma(p;\mu) \tag{2.42}$$

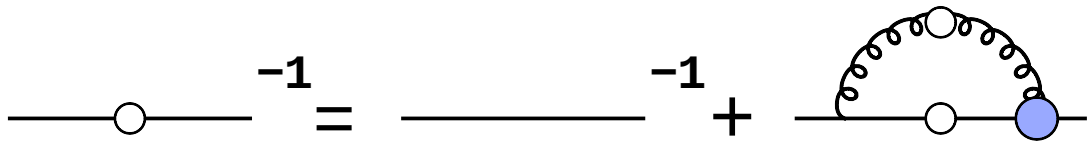

Figure 2.2: Diagrammatic representation of the qDSE. The straight lines illustrate quark propagators, the curly line is the gluon propagator. Empty circles indicate full propagators and the filled circle is the 1PI quark-gluon vertex.

where the superscript (0) indicates the bare propagator and $\Sigma(p;\mu)$ denotes the self-energy. The bare propagator reads

$$S_0^{-1}(p;\Lambda) = \not{p} + m_{bare}(\Lambda) \quad \text{with} \quad m_{bare}(\Lambda) = Z_m(\mu,\Lambda) m_R(\mu)\,. \tag{2.43}$$

The self-energy describes the quark-gluon interaction and is determined by

$$\Sigma(p;\mu) = Z_{1F}(\mu,\Lambda)\, g_s(\mu)^2\, C_f \int \frac{d^4q}{(2\pi)^4} \gamma_\mu\, S(q;\mu) \Gamma_\nu(k,l;\mu) D_{\mu\nu}(k;\mu) \tag{2.44}$$

with the factor $C_f = (N_c^2-1)/(2N_c)$ from the color trace. This constitutes a loop integral with an integral kernel composed of the Dirac matrix γ_μ, the full quark propagator $S(q;\mu)$, the 1PI $q\bar{q}g$-vertex $g_s(\mu)\,\Gamma_\nu(k,l,\mu)$ and the full gluon propagator $D_{\mu\nu}(k)$. We denote the gluon momentum by $k = (q-p)$ and the average momentum by $l = (q+p)/2$. The qDSE is diagrammatically shown in fig. 2.2. Since the full quark propagator occurs on both sides of the qDSE a self-consistent solution is mandatory. In general the loop integral needs to be regularized in numerical computations. We employ the MOM-regularization scheme and evaluate the integrals with a sharp cutoff Λ. This constitutes an $O(4)$-invariant regularization where the loop integration is restricted to momenta $q^2 \leq \Lambda^2$.

The renormalized and unrenormalized 1PI $q\bar{q}g$-vertices are related according to (2.21) by

$$\Gamma^{(2,1,0)}(\mu) = Z_2(\mu,\Lambda)\, Z_3^{1/2}(\mu,\Lambda) \Gamma^{(2,1,0)}(\Lambda)\,, \quad \text{where} \quad \Gamma^{(2,1,0)} = \frac{\delta^3\,\Gamma}{\delta\Psi\,\delta\bar{\Psi}\,\delta A}\,. \tag{2.45}$$

We omitted all indices. The dressed vertex appearing in the qDSE denotes the 1PI vertex divided by the strong coupling constant

$$\Gamma := \frac{1}{g_s}\Gamma^{(2,1,0)}\,. \tag{2.46}$$

From this the rescaling transformation of the vertex Γ can be derived:

$$\Gamma_\nu(k,l;\mu) = \frac{Z_2(\mu,\Lambda)}{\tilde{Z}_3(\mu,\Lambda)}\,\Gamma_\nu(k,l;\Lambda) \tag{2.47}$$

where we used the relation $Z_g = 1/(\tilde{Z}_3\, Z_3^{1/2})$ which is valid in Landau gauge ($\tilde{Z}_1 = 1$). It follows from the above that the unrenormalized and renormalized self-energies are related by

$$\Sigma(p;\Lambda) = Z_2^{-1}(\mu,\Lambda)\Sigma(p;\mu)\,. \tag{2.48}$$

This is of course necessary for a consistent rescaling of the left- and right-hand side of the qDSE.

Quark and gluon propagators and the $q\bar{q}g$-vertex

The fundamental buildings blocks in the qDSE are the full quark and gluon propagators and the proper $q\bar{q}g$-vertex. For the practical application of the qDSE we need explicit expressions for the propagators and the vertex.

A general parametrization of the quark propagator is given by

$$S(p) = \frac{1}{A(p)\not{p} + B(p)} = \frac{Z_f(p)}{\not{p} + M(p)} \tag{2.49}$$

with the vector dressing function $A(p)$ and the scalar dressing function $B(p)$. We also stated an often used notation in terms of the wave function renormalization $Z_f(p) = 1/A(p)$ and the mass function $M(p) = B(p)/A(p)$. The mass function $M(p)$ is renormalization point independent since vector and scalar dressing functions transform in the same way. Having decomposed the propagator in scalar and vector dressing functions one may use the same decomposition for the self-energy

$$\Sigma(p;\mu) = \not{p}\Sigma_A(p;\mu) + \Sigma_B(p;\mu) \tag{2.50}$$

where $\Sigma_A(p;\mu)$ denotes the vector self-energy and $\Sigma_B(p;\mu)$ the scalar self-energy. In the course of the regularization and renormalization procedure we impose the renormalization condition

$$A(p,\mu)\big|_{p^2=\mu^2} = 1\,. \tag{2.51}$$

If chiral symmetry is explicitly broken we additionally choose the condition

$$M(p)\big|_{p^2=\mu^2} = m_R(\mu)\,. \tag{2.52}$$

Z_2 and Z_m are determined from these conditions as will become clear later. From the former condition it follows that $Z_2(\mu,\Lambda) = A^{-1}(\mu,\Lambda)$.

Having discussed the quark propagator we will now continue with the gluon propagator and the $q\bar{q}g$-vertex. In the vacuum the Landau gauge gluon propagator and the $q\bar{q}g$-vertex can be parametrized by

$$D_{\mu\nu}(k) = \frac{Z(k)}{k^2}\left(\delta_{\mu\nu} - \frac{k_\mu k_\nu}{k^2}\right) \tag{2.53}$$

$$\Gamma_\mu(k,l;\mu) = \sum_i \left(f_i^{(1)}(k,l;\mu)\,\gamma_\mu + f_i^{(2)}(k,l;\mu)\,l_\mu + f_i^{(3)}(k,l;\mu)\,k_\mu\right) b_i \tag{2.54}$$

where $Z(k)$ is the gluon dressing function and $f_i^{(j)}(k,l;\mu)$ are the vertex dressing functions. Here $b_i = \{\mathbb{1}, \not{l}, \not{k}, [\not{l}, \not{k}]\}$ denotes basis elements. The four components of the vertex with k_μ (gluon momentum) will vanish in the qDSE in Landau gauge due to the transverse projector of the gluon propagator. The gluon and vertex dressing functions need to be specified to determine the quark propagator from the qDSE.

2.5 Dyson-Schwinger Equations at Finite T

Matsubara formalism

After having reviewed DSE's in the vacuum we will now discuss features at finite temperature. In section 2.1 we argued that the partition function can be represented by a generating functional with Euclidean action and compactified imaginary-time direction. The circumference in the imaginary-time direction is $1/T$. Due to this we define the Fourier transformation of functions periodic in imaginary-time direction, $f(\tau) = f(\tau + 1/T)$, by

$$f(\tau) = T\sum_{n=-\infty}^{\infty} e^{-i\tilde{\omega}_n\tau} f(i\tilde{\omega}_n)\,, \tag{2.55}$$

$$f(i\tilde{\omega}_n) = \int_0^{1/T} d\tau\, e^{i\tilde{\omega}_n\tau} f(\tau) \tag{2.56}$$

where $\tilde{\omega}_n = \pi T\, 2n$ refers to as Matsubara frequency. In the case of anti-periodic boundary conditions in imaginary-time direction, $\psi(\tau) = -\psi(\tau + 1/T)$, the Matsubara frequencies are of the form $\omega_n = \pi T(2n+1)$. With these conventions the fourth component of Euclidean momenta p_4 is to be identified with Matsubara frequencies $-\omega_n$ or $-\tilde{\omega}_n$. Thus for fermions,

$$p_4 \rightarrow -\omega_n \tag{2.57}$$

$$\text{and} \quad \not{p} = -\omega_n\gamma_4 + \gamma\cdot\boldsymbol{p}\,. \tag{2.58}$$

Due to the minus sign the analytic continuation to Minkowski space is obtained by $i\omega_n \to p_0$ respectively $i\tilde{\omega}_n \to p_0$.

The definition of the Fourier transformation in the Matsubara formalism yields sums over Matsubara frequencies instead of integrals over the fourth component of the Euclidean four vector in self-energies calculations

$$\int \frac{d^4p}{(2\pi)^4}\, f(-ip_4, \boldsymbol{p}) \longrightarrow -T\sum_{n_p} \int \frac{d^3p}{(2\pi)^3}\, f(i\omega_{n_p}, \boldsymbol{p})\,. \tag{2.59}$$

Here and in the following we explicitly use imaginary arguments for the energy in all functions. For the qDSE at finite temperature we then obtain ($P_\mu = (p_4, \boldsymbol{p}) = (-\omega_{n_p}, \boldsymbol{p})$)

$$S^{-1}(i\omega_{n_p}, \boldsymbol{p}; \mu) = Z_2(\mu, \Lambda)\, S_0^{-1}(i\omega_{n_p}, \boldsymbol{p}; \Lambda) + \Sigma(i\omega_{n_p}, \boldsymbol{p}; \mu) \tag{2.60}$$

with the self-energy

$$\Sigma(i\omega_{n_p}, \boldsymbol{p}; \mu) = -Z_{1F}(\mu, \Lambda)\, g_s(\mu)^2\, C_f\, T \sum_{n_q} \int \frac{d^3q}{(2\pi)^3}\, \gamma_\mu\, S(Q; \mu)\, \Gamma_\nu(K, L; \mu)\, D_{\mu\nu}(K; \mu)\,. \tag{2.61}$$

where $S(Q;\mu) = S(i\omega_{n_p}, \boldsymbol{p}; \mu)$ and correspondingly for $\Gamma_\nu(K, L; \mu)$ and $D_{\mu\nu}(K;\mu)$. Here $D_{\mu\nu}$ and Γ_ν are the gluon propagator and $q\bar{q}g$-vertex at finite temperature. In writing (2.61) it is assumed that the gluon propagator is color-diagonal in accordance with lattice gauge theory calculations [57].

In general there are no new UV-divergences arising at finite temperature compared to the vacuum. One may therefore implement the vacuum regularization and renormalization procedure. To this end we employ a sharp cutoff Λ for the computation of the self-energy eq. (2.61). This means that the integration and summation extends to momenta and frequencies with $\omega_{n_q}^2 + q^2 \leq \Lambda^2$. The Matsubara frequency summation is explicitly performed for frequencies $|n_q| \leq 39$ and the remaining sum is approximated by an integral. We checked that the results are insensitive to a change of the number of explicitly summed Matsubara modes. Furthermore the renormalization is carried out in a MOM-renormalization scheme as outlined in section 2.4. For the renormalization conditions we choose $C(i\omega_0, \boldsymbol{\mu}) = 1$ and $B(i\omega_0, \boldsymbol{\mu}) = m(\mu)$ and $\omega_0^2 + \boldsymbol{\mu}^2 = \mu^2$ with renormalization point μ; consequently all dressing functions are independent of the cutoff Λ. More details concerning the numerical procedure can be found in the appendix E.

Finite temperature vertex and propagators

At finite temperature there is a preferred rest frame which is specified by the heat bath. This is in contrast to the vacuum and will affect the general tensor structures for the propagators and vertices. The quark propagator at finite temperature is described by two vector dressing functions, A and C and one scalar dressing function B,

$$S(P) = \frac{1}{-\gamma_4\,\omega_{n_p}\,C(P) + \gamma\cdot\boldsymbol{p}\,A(P) + B(P)} = \frac{Z_f(P)}{-\gamma_4\,\omega_{n_p} + U(P)\,\gamma\cdot\boldsymbol{p} + M(P)}\,. \tag{2.62}$$

In the last equation we generalized the notation in terms of the wave function renormalization and the mass function to finite temperature. We chose to refer to $Z_f(P) = 1/C(P)$ as the wave function renormalization and hence $M(P) = B(P)/C(P)$ as the mass function. Additionally we encounter a term $U(P) = A(P)/C(P)$ that we will call the velocity function in a slight abuse of terminology. Sometimes a third term proportional to $\sigma_{\mu\nu} = \frac{i}{2}[\gamma_\mu, \gamma_\nu]$ is considered. This can be ruled out by imposing $\mathcal{P}\mathcal{T}$-invariance [58]. For a purely vectorial interaction as is used in this thesis $\mathcal{P}\mathcal{T}$-invariance is present.

A general parametrization of the Landau gauge gluon propagator at finite temperature can be written in terms of two dressing functions Z_T and Z_L as ($K = (k_4, \boldsymbol{k}) = (-\tilde{\omega}_{n_k}, \boldsymbol{k})$)

$$D_{\mu\nu}(K) = \left(P^T_{\mu\nu}(K)\,\frac{Z_T(K)}{K^2} + P^L_{\mu\nu}(K)\,\frac{Z_L(K)}{K^2}\right). \tag{2.63}$$

Hereby we introduced the projectors

$$P^T_{\mu\nu}(K) \;=\; (1-\delta_{4\mu})\,(1-\delta_{4\nu})\left(\delta_{\mu\nu} - \frac{K_\mu\,K_\nu}{\boldsymbol{k}^2}\right), \tag{2.64}$$

$$P^L_{\mu\nu}(K) \;=\; \left(\delta_{\mu\nu} - \frac{K_\mu K_\nu}{K^2}\right) - P^T_{\mu\nu}(K) \tag{2.65}$$

with the short-hand notation $K_\mu = (-\tilde{\omega}_{n_k}, \boldsymbol{k})_\mu$ and $K^2 = \tilde{\omega}^2_{n_k} + \boldsymbol{k}^2$. The projectors are transverse respectively longitudinal to the heat bath where the heat bath rest frame is specified by the four-velocity $U_\mu = (1, \mathbf{0})$. Both projectors are transverse to the gluon four momentum. The longitudinal part of the Landau gauge gluon propagator is also referred to as (chromo-)electric propagator and the transverse part as (chromo-)magnetic propagator.

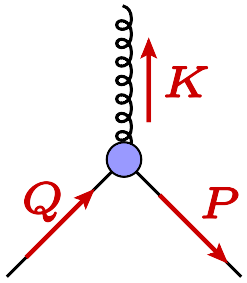

Figure 2.3: Kinematics of the $q\bar{q}g$-vertex.

For the sake of completeness we also present a general tensor decomposition of the $q\bar{q}g$-vertex at finite temperature. This can be obtained from the decomposition in the vacuum by extension with the four-velocity U_μ. Using the Dirac basis $b_i = \{\mathbb{1}, \not{L}\,, \not{K}\,, \not{U}\,, [\not{L}\,, \not{K}], [\not{L}\,, \not{U}]\,, [\not{K}\,, \not{U}]\,, \not{L}\not{K}\not{U}\}$ the vertex can be written as

$$\Gamma_\mu(K,L;\mu) = \sum_i \Big(\gamma_\mu\, f_i^{(1)}(K,L;\mu) + L_\mu\, f_i^{(2)}(K,L;\mu) + K_\mu\, f_i^{(3)}(K,L;\mu) + U_\mu\, f_i^{(4)}(K,L;\mu) \Big) b_i\,. \tag{2.66}$$

For the vertex we obtain in summary 32 possible tensor components at finite temperature. By way of comparison there are 12 components in the vacuum. Note that additional symmetry constraints might reduce the number of allowed tensor components considerably. As in the vacuum the longitudinal components $\sim K_\mu$ are projected out by the transverse projector of the Landau gauge gluon propagator.

Solution Strategies

In this section we will outline our strategy in order to obtain a closed set of equations for the quark propagator. Figure 2.4 shows diagrammatically the DSE for the gluon propagator and the $q\bar{q}g$-vertex. In addition also the equations for the ghost and the quark propagators are displayed. We observe that this system of equations is not closed since it involves also the dressed ghost-gluon, three-gluon, four-gluon and two-gluon-two-quark vertex.

Depending on the purpose there are different ways to proceed. Analytic investigations can be performed in certain regimes, as e.g. in the infrared limit of the correlators. This is of particular interest in order to verify the confinement requirements of Kugo-Ojima [45] or Gribov-Zwanziger [59, 60]. Alternatively one may be tempted to obtain a consistent solution for general momenta by numerical computations. In doing so a sensible truncation of the set of equations has to be accomplished. The gluon propagator

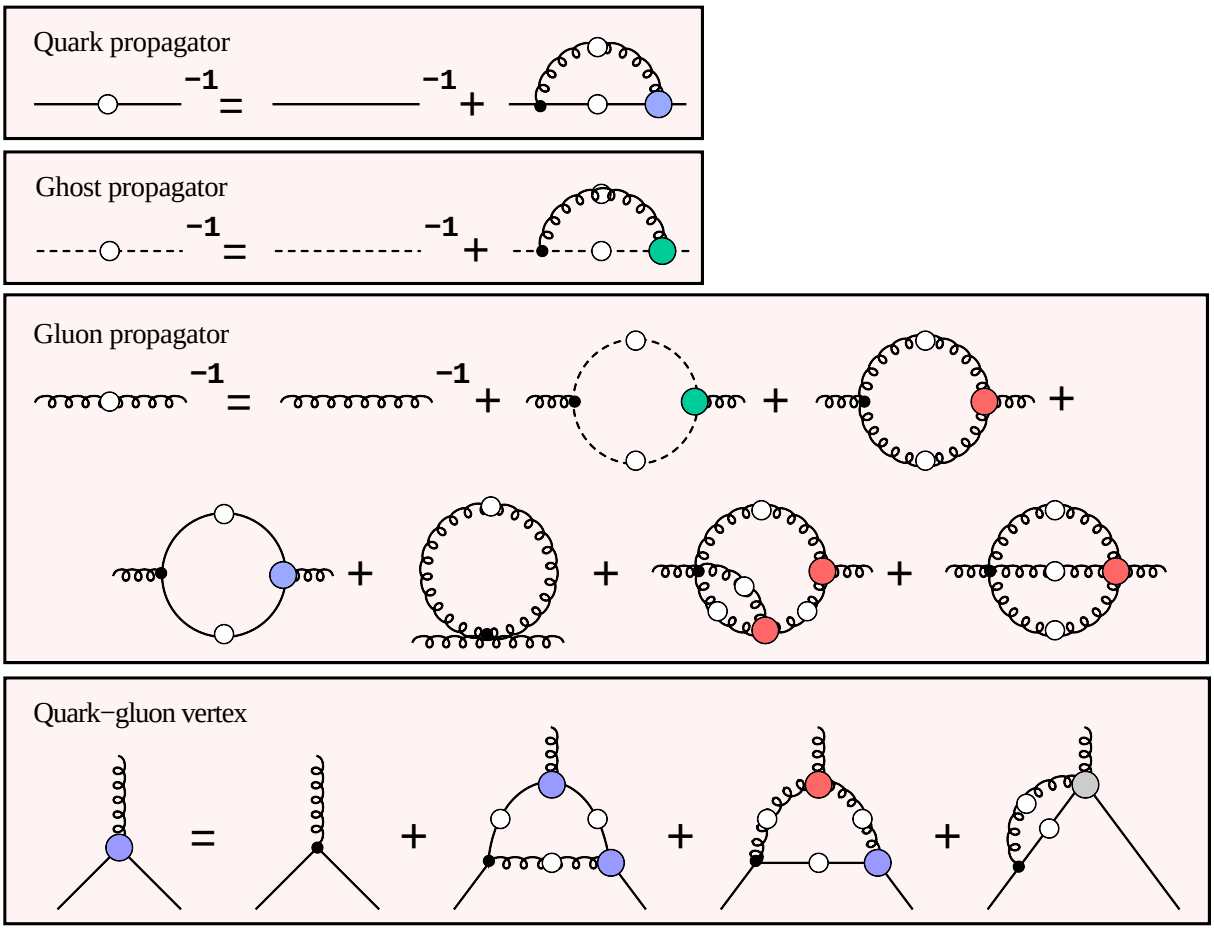

Figure 2.4: Diagrammatic representation of propagator DSE's and the $q\bar{q}g$-vertex DSE. The empty circles represent full propagators. The filled circles denote 1PI (proper) vertices.

being a major ingredient in the quark DSE, may in principle be obtained in quenched approximation from corresponding DSE's [61–64]. At finite temperature however, this turns out to be a formidable task and the results are still on a qualitative level only. In our approach we therefore use results from lattice gauge theory as input. In the Dyson-Schwinger framework these correspond to solutions of the gluon propagator Dyson-Schwinger equation in fig. 2.4 with the only truncation of neglecting the quark loop. Such calculations have been performed recently yielding results for a fine temperature grid over a temperature range from 0 to 2.2 T_c [40]. We present and discuss the outcome in detail in section 3.2. The details of the second ingredient for a closed quark DSE, namely the quark-gluon vertex, are yet to be explored. First exploratory results on the mass and momentum dependence of the vertex at zero temperature have been reported from lattice

calculations and Dyson-Schwinger equations, see [65–71] and Refs. therein. However, not much is known about its temperature dependence. In such a situation a viable strategy is to use phenomenological model ansätze for the vertex which are then justified by comparing results with other approaches. This strategy has been successful in previous works, see Refs. [31–33], and will therefore also be adopted here. In the construction of model ansätze we are guided by expediency under consideration of constraints. We outline constraints and general considerations in the following and postpone the specification of the detailed expression for the vertex to section 3.2. Necessary boundary conditions for the vertex are:

- spontaneous breaking of chiral symmetry should be obtained
- the mass function should have the correct ultraviolet (UV) behavior with its anomalous dimension γ_m
- eq. (2.47) for multiplicative renormalizability should be fulfilled implying renormalization point independence of the quark mass function

The first condition is associated to nonperturbative properties of the $q\bar{q}g$-vertex. It basically means that the $q\bar{q}g$-vertex has to provide a certain amount of interaction strength at low momenta. The latter two constraints are known from perturbative QCD. The UV-behavior of the mass function as known from the operator product expansion is given by [72]

$$M(p) \overset{p^2\to\infty}{\simeq} -\frac{4\pi\langle\bar{\psi}\psi\rangle}{3p^2}\frac{\alpha(\mu)^{\gamma_m}}{\alpha(p)^{\gamma_m-1}} + M(\mu)\left(\frac{\alpha(p)}{\alpha(\mu)}\right)^{\gamma_m}. \tag{2.67}$$

Here we used the one loop perturbative form of the running coupling constant

$$\alpha(p) = \frac{\gamma_m\pi}{\ln\left(p^2/\Lambda_{QCD}^2\right)} \quad \text{and} \quad \gamma_m = \frac{12}{11N_c - 2N_f}\,. \tag{2.68}$$

The same result should certainly also be obtained from the Dyson-Schwinger equations [73]. A UV-analysis of the qDSE shows that this is established for a vertex with the asymptotic behavior

$$\Gamma^a_\mu(k,l;\mu) \xrightarrow{k\to\infty} \frac{Z_2(\mu,\Lambda)\tilde{Z}_3(\mu,\Lambda)}{Z(k,\mu)}\,\frac{\alpha(k)}{\alpha(\mu)}\gamma_\mu\, t^a\,. \tag{2.69}$$

This expression also implies renormalization point independence of the mass function as can be verified using $\alpha(\mu) = \alpha(\Lambda)/Z_g^2(\mu,\Lambda)$ and $Z(k,\mu) = Z(k,\Lambda)/Z_3(\mu,\Lambda)$.

We will employ these properties also at finite temperature[4]. Therefore we use a vertex ansatz effectively composed as follows:

[4]Of course we only demand spontaneous chiral symmetry breaking at low temperatures.

$$\Gamma^a_\mu(K,L;\mu) = \tilde{Z}_3(\mu,\Lambda)\, V_\mu(L+K/2, L-K/2;\mu)\, \hat{\Gamma}(K;\mu)\, t^a \tag{2.70}$$

where the large letters for the momenta indicate finite temperature and V_μ and $\hat{\Gamma}$ reveal the asymptotic behavior

$$V_\mu(L+K/2, L-K/2;\mu) \xrightarrow{K\to\infty} Z_2(\mu,\Lambda)\gamma_\mu\,, \tag{2.71}$$

$$\hat{\Gamma}(K;\mu) \xrightarrow{K\to\infty} \frac{\alpha(K)}{Z(K)\alpha(\mu)}\,. \tag{2.72}$$

The function $\hat{\Gamma}$ will essentially be a combination of the running coupling constant at high momenta with an additional ansatz for low momenta accounting for spontaneous chiral symmetry breaking. It may be considered as the non-Abelian contribution to the vertex. For V_μ we use parts of an Abelian vertex construction deduced by Ball and Chiu [74] from the QED Ward-Takahashi identity (WTI) of the vertex. This is motivated by a comparison of the Slavnov-Taylor identity (STI) with the WTI and by the observation that the non-Abelian ghost terms in the STI disappear in the high temperature limit (see e.g. [75]). The QED WTI reads

$$\begin{aligned} K_\mu\, \Gamma_\mu(K,L;\mu) &= S^{-1}(L+K/2) - S^{-1}(L-K/2) \\ &= K_\mu\Big(2L_\mu\Big[-\Delta_C\,\gamma_4\omega_{n_L} + \Delta_A\,\gamma\cdot\boldsymbol{l} + \Delta_B\Big]\Big) - \gamma_4\,\omega_{n_K}\,\Sigma_C + \gamma\cdot\boldsymbol{k}\,\Sigma_A \end{aligned} \tag{2.73}$$

where we used the relative and average momenta $K = Q - P$ and $L = (Q+P)/2$ and the abbreviations

$$\Delta_F = \frac{F(Q)-F(P)}{Q^2-P^2} \quad \text{and} \quad \Sigma_F = \frac{F(P)+F(Q)}{2}\,. \tag{2.74}$$

This yields the following generalization of the Ball-Chiu vertex to finite temperature[5]:

$$\Gamma_\mu(K,L;\mu) = \delta_{\mu4}\gamma_4\,\Sigma_C + (1-\delta_{4\mu})\gamma_\mu\,\Sigma_A + 2L_\mu\big[-\Delta_C\,\gamma_4\omega_{n_L} + \Delta_A\,\gamma\cdot\boldsymbol{l} + \Delta_B\big]\,. \tag{2.75}$$

Note that in the limit of vanishing bare quark masses in the chiral restored phase Δ_B vanishes.

[5] Note that in principle the WTI as stated in (2.73) only projects on the longitudinal part of the vertex. Since the longitudinal components of the vertex vanish in the qDSE the WTI seems to provide no useful constraints for the vertex. However the vertex given in (2.75) is not purely longitudinal. In fact in constructing the vertex we also took care that the differential Ward identity $\Gamma_\mu(0,L;\mu) = (\partial S^{-1}(L))/(\partial L_\mu)$ is fulfilled. This ensures that the vertex has no kinematic singularity for vanishing gluon momentum and thereby also restricts transverse components.

For comparison we state the STI for the $q\bar{q}g$-vertex. It is given by

$$G^{-1}(K)\, K_\mu\, \Gamma^a_\mu(K,L;\mu) = H^a(L,K;\mu)\, S^{-1}(L+K/2) - S^{-1}(L-K/2)\, H^a(L,K;\mu) \quad (2.76)$$

where $G^{-1}(K)$ is the inverse ghost dressing function and $H^a(L,K)$ denotes the ghost-quark scattering kernel. Our ansatz (2.70) thus implicitly implicates $H^a(K,L,\mu) \sim f(K)t^a$ for the quark-ghost scattering kernel with some function $f(K)$. As already mentioned this identity reduces to the QED like identity

$$K_\mu\, \delta\tilde{\Gamma}_\mu(K,L) = \delta\Sigma(L+K/2) - \delta\Sigma(L-K/2) \quad (2.77)$$

when considering the leading behavior in temperature, i.e. in the course of the HTL approximation [75]. Here $\delta\tilde{\Gamma}_\mu$ and $\delta\Sigma$ denote the vertex and quark self-energies in the HTL approximation. This reduction is basically due to the vanishing of the self-energies to Green's functions with external ghost legs within the HTL approximation.

Chapter 3

Chiral and Deconfinement Transition from the Quark Propagator

In this chapter, we will investigate the chiral and the deconfinement transition at finite temperature in SU(2) and SU(3) Yang-Mills theory. The chiral transition is studied by means of the quark condensate. This quantity can easily be calculated from the nonperturbative quark propagator in momentum space [76]. In contrast to chiral order parameters it is usually not easy to access quantities that qualify as deconfinement order parameters when using functional methods. Progress on this issue has been made in the past years. For instance in refs. [77, 78], the ghost and gluon propagators of Landau gauge Yang-Mills theory have been used to determine the Polyakov loop potential within an effective action approach. In a different approach in ref. [79] the analyticity properties of the quark propagator were exploited to distinguish between the confining and deconfining phases.

In this work, we will follow an alternative strategy by calculating the dual quark condensate or dressed Polyakov loop. This quantity is sensitive to center gauge transformations and thus constitutes an order parameter for deconfinement. One important aim of this chapter is to show that this observable is well suited for functional continuum methods. Furthermore, we will investigate (potentially gauge-dependent) mechanisms linking deconfinement and chiral symmetry restoration. Since the dual quark condensate is extracted from a generalized quark propagator, connections between dynamical chiral symmetry breaking and quark confinement in QCD can be established [80–86]. In this respect, the study presented here, in particular highlights the role of the longitudinal, electric part of the Landau gauge gluon propagator. Eventually, this investigation also serves as an important intermediate step towards an analysis of the QCD phase diagram at non-vanishing

quarkchemical potential. Due to the notorious sign problem of lattice QCD in that realm there is great demand for other methods beyond model calculations. Functional methods like Dyson-Schwinger equations [32, 33, 36] and the functional renormalization group [87–89] are ready to fill this gap. To obtain meaningful results at non-zero chemical potential it is, however, first necessary to provide the applicable theoretical framework at zero chemical potential, where one can compare with the results from lattice QCD. In this sense, we first employ a truncation scheme avoiding complications that might arise with dynamical quarks. This amounts to neglecting quark loop contributions in the calculation and corresponds to an approximation of quenched lattice theory. In the quenched theory the deconfinement transition is a strict phase transition. Hence, as a further advantage of this truncation we expect a clear signal for the deconfinement transition. This also allows to gain as much insight as possible into the fidelity of our truncation.

This chapter is organized as follows: We first outline our order parameter for the confinement-deconfinement transition. Here we consider the dual quark condensate as defined in ref. [84]. This quantity is extracted from the momentum dependence of the quark propagator and is therefore accessible from the quark-DSE. In the subsequent section we employ the truncation scheme for the quark-DSE. To this end, we use SU(2)- and SU(3)-lattice results for the temperature dependent gluon propagator and a temperature dependent Ansatz for the quark-gluon vertex as input. We then study the gauge-invariant order parameters for the chiral and deconfinement transition and present the results.

3.1 The Dual Quark Condensate

The dual quark condensate as order parameter for center symmetry has emerged from a series of works connecting spectral sums of the Dirac propagator with Polyakov loops and their correlators [80–83]. Within the framework of lattice gauge theory the dual condensate has been introduced in ref. [90] and its usefulness within functional methods was first explored in ref. [85].

Before discussing the dual quark condensate we introduce the chiral quark condensate defined by [76]

$$\langle\bar{\psi}\psi\rangle := Z_m\, Z_2\, N_c\, T \sum_{n_p} \int^{\Lambda} \frac{d^3p}{(2\pi)^3}\, \mathrm{tr}_D\, S(i\omega_{n_p}, \boldsymbol{p})\,. \tag{3.1}$$

It may be computed from the momentum behavior of the nonperturbative quark propagator and constitutes an order parameter for chiral symmetry. In the limit of vanishing bare quark masses the integral is well behaved and delivers the chiral condensate. At finite

bare quark mass it is quadratically divergent and needs to be regularized as indicated at the integral, see ref. [95] for a recent discussion.

In order to obtain the dual quark condensate we consider non-standard, $U(1)$-valued boundary conditions in temporal direction for the quark fields. These can be parametrized by

$$\psi(\beta, \boldsymbol{x}) = e^{i\varphi}\psi(0, \boldsymbol{x}) \tag{3.2}$$

where the boundary angle φ varies between $\varphi \in [0, 2\pi[$, with $\varphi = 0$ for periodic and $\varphi = \pi$ for the usual, physical antiperiodic boundary conditions for the fermionic quark fields. In momentum space, these $U(1)$-valued boundary conditions correspond to generalized, φ-dependent Matsubara frequencies

$$\omega_{n_p}^{\varphi} = \pi T\big(2n_p + \varphi/\pi\big). \tag{3.3}$$

From the φ-dependent, nonperturbative quark propagator $S(i\omega_{n_p}^{\varphi}, \boldsymbol{p})$ one can then extract the φ-dependent quark condensate according to

$$\langle\bar{\psi}\psi\rangle_{\varphi} := Z_2\, N_c\, T \sum_{n_p} \int^{\Lambda} \frac{d^3p}{(2\pi)^3}\, \mathrm{tr}_D\, S(i\omega_{n_p}^{\varphi}, \boldsymbol{p}) \tag{3.4}$$

where the conventional condensate is obtained for the special case $\varphi = \pi$ and multiplication of this expression with Z_m. The corresponding dual observable, the dual quark condensate or dressed Polyakov loop, is obtained by a Fourier-transformation of the φ-dependent condensate with respect to the winding number n,

$$\Sigma_n = \int_0^{2\pi} \frac{d\varphi}{2\pi}\, e^{-i\varphi n}\, \langle\overline{\psi}\psi\rangle_{\varphi} \tag{3.5}$$

and specializing to the case $n = 1$. The dual condensate or dressed Polyakov loop Σ_1 represents an order parameter for deconfinement. The two order parameters, (3.4) with $\varphi = \pi$ and (3.5), can be extracted from the dressed, temperature dependent quark propagator calculated from functional methods [40, 41, 85, 86].

Within a lattice formulation the physical meaning of Σ_n and its connection to Polyakov loops can be clarified using a geometric series expansion of the propagator for large quark mass. The expansion yields a representation of the φ-dependent condensate as a sum over all possible closed loops l:

$$\langle\overline{\psi}\psi\rangle_{\varphi} = \sum_{l\in\mathcal{L}} \frac{e^{i\varphi n(l)}}{(am)^{|l|}}\, U(l) \tag{3.6}$$

where $\mathcal{L}$ denotes the set of all closed loops l with length $|l|$ on a lattice with lattice spacing a. Furthermore, m is the quark mass and $U(l)$ stands for the expectation value of the

product of link variables in a loop l multiplied with appropriate sign and normalization factors (see ref. [84] for details). Each loop that closes around the temporal boundary picks up factors of $e^{\pm i\varphi}$ according to its winding number $n(l)$. The Fourier transform in (3.5) projects out those loops with winding number n. The dual condensate Σ_1, then corresponds to loops that wind exactly once around the temporal direction [84]. The loops are in general dressed with spatial fluctuations. The dual condensate transforms under center transformation identically as the conventional Polyakov loop [91, 92] and is therefore an order parameter for center symmetry. The numerical agreement between the dressed and conventional Polyakov loop has been established for gauge groups $SU(3)$ [93] and, remarkably, also for the centerless $G(2)$ [94].

Below, we will determine the dual condensate Σ_1 from Dyson-Schwinger equations in the infinite volume and continuum limit. As aforementioned, the quark condensate at non-vanishing quark mass is quadratically divergent and needs to be regularized. Correspondingly, the loop expansion eq. (3.6) breaks down for $a \to 0$. In this work, we will employ an ultraviolet regulator in the form of a simple cutoff. For large enough cutoffs the regulator dependent part of the condensate is independent of temperature and therefore does not affect the chiral and the deconfinement transition temperatures.

A remark concerning the Roberge-Weiss periodicity seems appropriate here. The modification to $U(1)$-valued boundary conditions for dynamical quark fields in fact corresponds to the introduction of an imaginary chemical potential. However, through out this thesis we only consider the modification of the temporal boundary conditions of valence (test) quarks, without altering the dynamics of the theory. This amounts to an explicit breaking of Roberge-Weiss symmetry and we therefore do not encounter the pattern of Roberge-Weiss periodicity [56]. Such a formulation avoids the complications associated with the introduction of nontrivial boundary conditions into the generating functional of QCD. For a different approach explicitly taking into account Roberge-Weiss periodicity, we refer to a renormalization group study in ref. [86].

In the following, we summarize important properties of the φ-dependent condensate and the dressed Polyakov loop Σ_1. We also discuss the relation to the usual thin Polyakov loop and highlight findings acquired within this thesis:

- ✦ $\langle\bar{\psi}\psi\rangle_\varphi$ may be interpreted as a sum over closed loops winding around the temporal direction. For large quark masses loops with large length $|l|$ respectively large winding numbers $n(l)$ are suppressed by a factor $1/m^{|l|}$.
  - ➢ For smaller quark masses also loops with higher winding numbers contribute to $\langle\bar{\psi}\psi\rangle_\varphi$. We find the expansion (3.6) to break down in the chiral limit where

loops of all length contribute.

- $\langle\bar{\psi}\psi\rangle_{\varphi=\pi}$ yields the conventional quark condensate and is thus an order parameter for chiral symmetry.

- Σ_n is the projection of $\langle\bar{\psi}\psi\rangle_{\varphi}$ onto loops winding n-times around the temporal direction. Like the Polyakov loop, Σ_1 winds exactly once around the temporal direction. Hence, Σ_1 serves as an order parameter for deconfinement.

  ➢ We show that the dressed Polyakov loop is a well suited deconfinement order parameter for functional continuum methods.

- In contrast to the thin Polyakov loop, Σ_1 contains loops with spatial fluctuations and therefore, it is also called dressed Polyakov loop.

- Σ_1 turns into the thin Polyakov loop for large quark masses due to the mass factor $1/m^{|l|}$.

- From the above it follows that a connection is established between an order parameter for chiral symmetry and deconfinement.

  ➢ Our analysis sheds light on a mechanism linking confinement and chiral symmetry restoration by locating the change of the electric gluon propagator around T_c as the source for chiral symmetry restoration in Landau gauge.

Having discussed our order parameters for chiral symmetry and deconfinement we will now employ the truncation scheme.

3.2 The Truncation Scheme

Gluon propagator

As discussed in section 2.5, we will use insight from lattice gauge theory calculations for the input of the gluon propagator in the quark Dyson-Schwinger equation. In reference [40], results for the gluon dressing functions, Z_T and Z_L, calculated in quenched lattice theory were presented. Besides gauge group SU(3) also SU(2) gauge group was considered and the dressing functions were extracted for 16 temperatures between 0 and $2.2\,T_c$ ($T_c = 303$ MeV for SU(2) and $T_c = 277$ MeV for SU(3)). In the quark Dyson-Schwinger equation, we also need to evaluate these dressing functions for momenta not identically to the ones of the lattice calculation. Therefore, we use temperature dependent fits to these

data. In fig. 3.1 we show results for the soft modes of SU(3), $\tilde{\omega}_{n_p} = 0$, for a variety of temperatures. The lattice data are denoted by points and the corresponding fit functions are represented by straight lines. The fit functions for the soft transverse and longitudinal dressing functions $Z_{T,L}$ of the gluon propagator are given by

$$Z_{T,L}(P) = \frac{P^2\Lambda^2}{(P^2+\Lambda^2)^2}\left\{\left(\frac{c}{P^2+\Lambda^2 a_{T,L}(T)}\right)^{b_{T,L}(T)} + \frac{P^2}{\Lambda^2}\left(\frac{\beta_0\alpha(\mu)\ln[P^2/\Lambda^2+1]}{4\pi}\right)^{\gamma}\right\} \tag{3.7}$$

where $a_{T,L}(T)$ and $b_{T,L}(T)$ are temperature dependent and gauge group dependent fit parameters. The first term in the curly bracket determines the low momentum behavior whereas the second one reflects the asymptotic UV-behavior. We introduced a temperature independent scale parameter $\Lambda = 1.4$ GeV and the coefficient $c = 11.5\,\mathrm{GeV}^2$. Furthermore, $\beta_0 = 4/\gamma_m = (11\,N_c - 2\,N_f)/3$ is given by the known perturbative UV-behavior as well as the gluon anomalous dimension $\gamma = (-13\,N_c + 4\,N_f)/(22\,N_c - 4\,N_f)$. Thus, for the quenched theory which we consider in this chapter, $\beta_0 = 11N_c/3$ and $\gamma = -13/22$ and we renormalize at $\alpha(\mu) = 0.3$. The details of the temperature dependent fit parameters are relegated to the appendix C. The fit function, eq. (3.7), generalizes the one used in refs. [41, 85], where the temperature dependent exponent $b_{T,L}(T)$ has been kept fixed, i.e. $b_{T,L}(T) = 2$. Since we now have more accurate lattice gluon data at our disposal we found it useful to relax this condition and thus provide an even better representation of the lattice data. In general, our fits are optimized in particular in the mid-momentum regime, which is most important in the quark-DSE. One may speculate whether an irrational exponent $b_{T,L}(T)$ with the corresponding temperature dependent cut in the p^2-plane signals quantitative changes also in the analytic structure of the gluon, as suggested in [61, 62].

As found in the lattice calculation, the hard modes, $\tilde{\omega}_{n_p} \neq 0$, can be very well approximated by $Z_{T,L}(i\tilde{\omega}_{n_p}, \boldsymbol{p}) = Z_{T,L}(0, |P|)$ with $|P| = \sqrt{\tilde{\omega}_{n_p}^2 + \boldsymbol{p}^2}$. We use this approximation for the fit functions of the hard modes in the qDSE and restrict the discussion to the soft modes in the following. As can be seen in the upper part of fig. 3.1, the transverse, chromomagnetic gluon dressing function shows no indication of the deconfinement phase transition. Over the whole temperature range a suppression in the infrared, particularly of the bump at around 1 GeV, is obtained for increasing temperature. In contrast to this, a more pronounced temperature dependence of the longitudinal, chromoelectric gluon dressing function is discernible from the lower part of fig. 3.1. Note the different scale. More importantly Z_L shows a special behavior around the deconfinement phase transition temperature. In the confined phase, it increases in the infrared with increasing temperature before it suddenly decreases at the transition to the deconfining phase. In fact, as will become clear in the following, the phase transition temperature may be determined

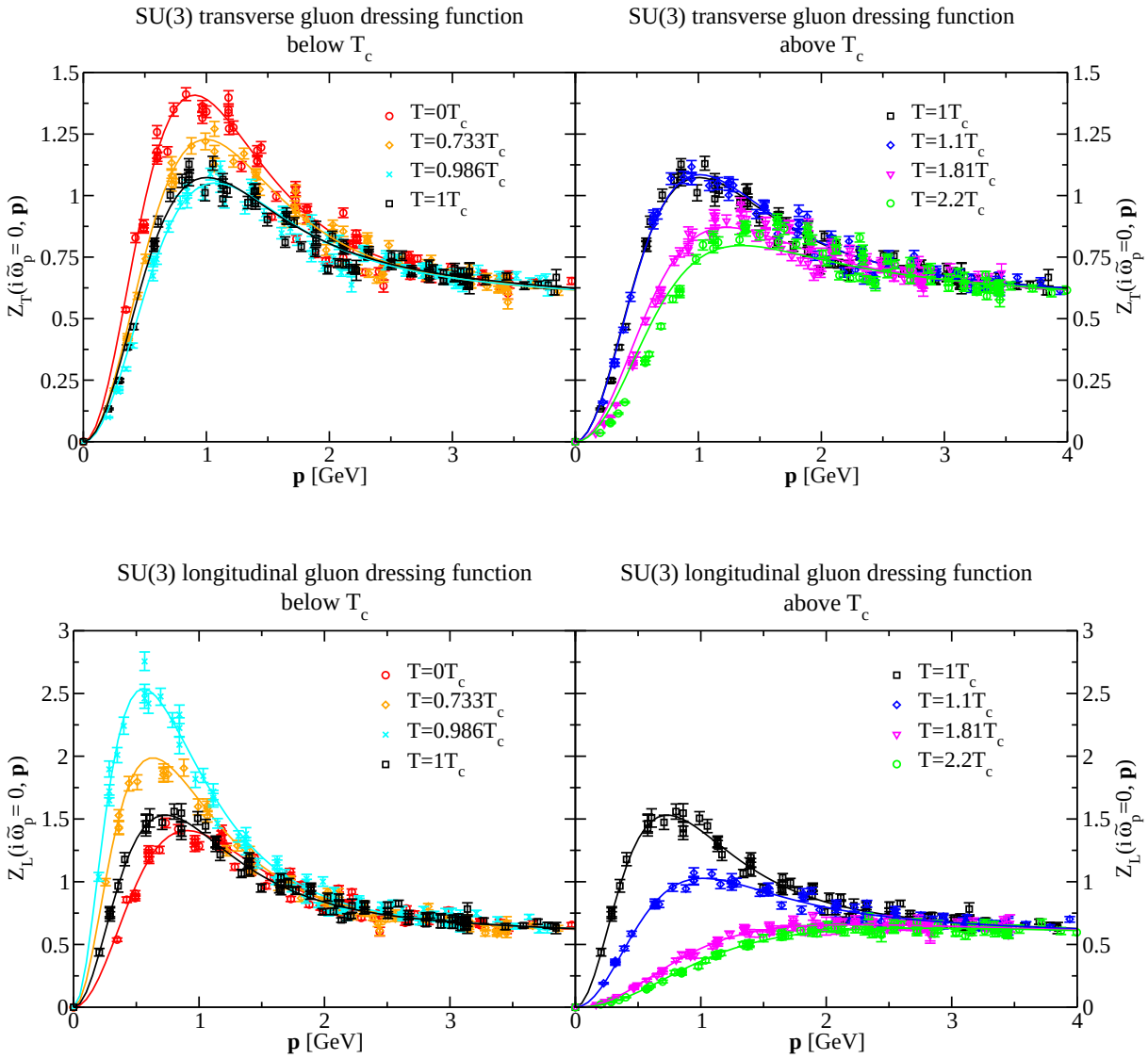

Figure 3.1: Transverse (upper plot) and longitudinal (lower plot) temperature dependent gluon dressing functions for the lowest Matsubara frequency from SU(3) lattice calculations compared with our fits. The left part shows results below the critical temperature (0 T_c, 0.733 T_c, 0.986 T_c, 1 T_c) and the right part above the critical temperature (1 T_c, 1.1 T_c , 1.81 T_c , 2.2 T_c).

by this sudden decrease. This behavior is seen for both gauge groups, SU(2) and SU(3), although it is less pronounced for SU(2). The corresponding figure for gauge group SU(2) can be found in appendix C.

A quantity allowing for a quantitative analysis and indicating an important difference

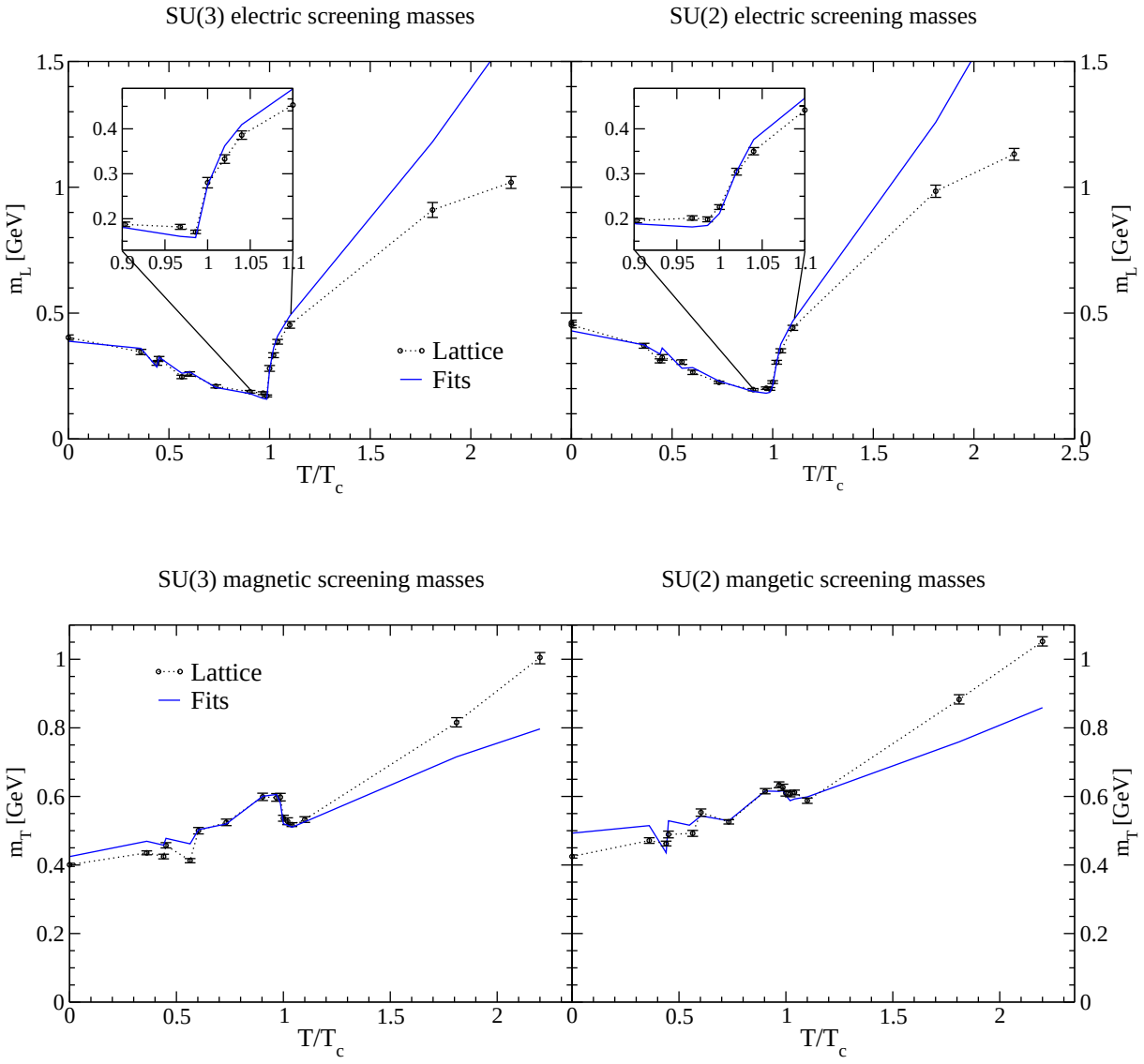

Figure 3.2: SU(3) (left) and SU(2) (right) temperature dependent scale parameters in our fits for the lattice gluon propagator compared with the lattice results for the electric (upper part) and magnetic (lower part) screening masses of the gluons.

between the gauge groups is the electric screening mass

$$m_L = \left(\frac{Z_L(P)}{P^2} \bigg|_{P^2=0} \right)^{-1/2} \tag{3.8}$$

shown in the upper part of fig. 3.2. For comparison, we also display the screening mass as extracted from the infrared behavior of the fit functions. The results for the magnetic

screening mass

$$m_T = \left(\frac{Z_T(P)}{P^2} \bigg|_{P^2=0} \right)^{-1/2}, \tag{3.9}$$

are depicted in the lower part of fig. 3.2. Below the phase transition temperature we find the electric screening mass decreasing with increasing temperature, reaching its minimum value at the phase transition temperature. At this temperature a strong reaction of the mass expressing itself in a sudden increase is discernible. We stress that the critical temperature determined using the Polyakov loop as order parameter coincides with the temperature determined from the change in the electric screening mass within the employed temperature resolution [40]. As opposed to this, there is no pronounced reaction to the phase transition of the magnetic screening mass. For the electric screening mass we also show a magnification of the temperature range around the critical temperature. The SU(3) data show a more rapid change for the screening mass than the SU(2) data. One may speculate if the rapid change in the SU(3) case signals the nature of the first-order phase transition whereas the smoother behavior for SU(2) may indicate the second-order phase transition.

The comparison with the screening masses as extracted from the fit functions shows a very satisfactory fit quality except for the screening masses at the largest temperatures. Here the lattice results suffer mostly from systematic artifacts due to the restricted number of points in the time direction [63]. This may be reflected in the mismatch of the screening masses with the ones extracted from our fit. Indeed, one may even argue that the electric screening masses from the fits are more accurate in the large temperature regime since they nicely reproduce the expected proportionality of the screening mass with temperature, $m_L \sim T$, known from hard thermal loop results. We also note that at the two highest temperatures available the fit function describes the low and mid momentum behavior of the electric gluon propagator very precise. On the other hand, the fit function is not capable to describe the qualitative mid-momentum dependence of the magnetic propagator in this temperature range, as can be seen in the right upper plot of fig. 3.1 and C.1 (see appendix C). We checked that this momentum behavior can be described precisely using in addition a momentum dependent screening term in the fit function. Anyway, in the important region around the critical temperature both fits work perfectly well and represent therefore a trustable input for the Dyson-Schwinger equation of the quark propagator.

Note, that as a significant difference to the fits used in refs. [41, 85] it turns out that the transition of the electrical screening mass from its decreasing behavior below the critical temperature T_c to the increase above T_c is much sharper. This sharp change around T_c

was not resolved by the then available lattice data of ref. [63]. As a consequence of the much improved temperature resolution available now we will see that the corresponding deconfinement transition extracted from the quark propagator is also much more pronounced than the one seen in [41, 85]. This will be discussed in more detail in the next section.

$q\bar{q}g$-vertex

Before turning to the results it remains to specify the dressed quark-gluon vertex employed in our truncation. Similar to refs. [41, 85] we employ the following temperature dependent model

$$\begin{aligned}\Gamma_\nu(K,L;\mu) &= \widetilde{Z}_3\left(\delta_{4\nu}\gamma_4\frac{C(Q)+C(P)}{2}+(1-\delta_{4\nu})\gamma_\nu\frac{A(Q)+A(P)}{2}\right)\\ &\times\left(\frac{d_1}{d_2+K^2}+\frac{K^2}{\Lambda^2+K^2}\left(\frac{\beta_0\alpha(\mu)\ln[K^2/\Lambda^2+1]}{4\pi}\right)^{2\delta}\right),\end{aligned}\tag{3.10}$$

where $Q=L+K/2$ and $P=L-K/2$ denote the quark and antiquark momenta, K the gluon momentum and $L=(Q+P)/2$ the average momentum. Furthermore, for N_c colors and N_f flavors the anomalous dimension of the vertex is given by $\delta=-9\,N_c/(44\,N_c-8\,N_f)$. Thus in the quenched approximation, i.e. $N_f=0$, the anomalous dimension $\delta=-9/44$ is independent of the number of colors. Both together, the gluon dressing function and the quark-gluon vertex behave like the running coupling at large momenta as we demanded in (2.72) since it is a necessary boundary condition for any model interaction in the quark DSE. The dependence of the vertex on the quark dressing functions A and C corresponds to the first terms of the right hand side of eq. (2.75) which represents the generalization of the Ball-Chiu vertex to finite temperature. As explained in section 2.5, this is motivated by the Slavnov-Taylor identity for the vertex. We thus obtain a non-trivial temperature dependence of the vertex. Note however, that this also prevents the calculation of pressure differences from the Cornwall-Jackiw-Tomboulis (CJT) formalism [96]. The remaining fit function is purely phenomenological, see e.g. [97] where an elaborate version of such an ansatz has been used to describe meson observables. We use $d_2=0.5\,\mathrm{GeV}^2$ for both gauge groups, but $d_1=7.6\,\mathrm{GeV}^2$ for SU(2) and $d_1=4.6\,\mathrm{GeV}^2$ for SU(3). The change in parameter d_1 from SU(2) to SU(3) is again motivated by the Slavnov-Taylor identity. At high temperatures it is expected that it reduces to the QED Ward-Takahashi identity multiplied with the nonperturbative ghost dressing function. A comparison of SU(2) and SU(3) ghost dressing functions in the infrared calculated on the lattice shows that for small momenta, $G(p)$ of SU(3) is reduced by roughly half compared to SU(2), see ref. [40]. Even though the quantitative values for the ghost dressing functions at low

momenta from the lattice might contain considerable uncertainties, we assume the ratio of SU(2) to SU(3) to be reliable. In addition, we also checked that a moderate variation of these parameters does not shift the critical temperatures of both, the chiral and the deconfinement transition.

Finally we wish to repeat a word of caution as concerns the chiral limit in our approximation scheme [41]. A prominent feature of the quenched theory not reproduced by our framework is the appearance of quenched chiral logarithms in the chiral condensate. These are well-known to be generated by η' hairpin diagrams, which are not represented by our vertex ansatz. For the present investigation we believe this is more an advantage than a drawback. Quenched chiral logarithms are most notable in the chiral limit, where they lead to a singularity in the chiral condensate. Since we do not encounter this singularity, we are in a position to investigate both, the ordinary condensate and the dressed Polyakov loop also in the chiral limit.

3.3 Numerical Results

Angular dependence of the quark condensate

In fig. 3.3 we study the angular dependence of the condensate which can be understood from the loop expansion of the condensate, eq. (3.6). The loop expansion is applicable at finite, non-vanishing quark masses and under presence of an ultraviolet regulator for the condensate. From (3.6) we deduce that loops winding n-times around the temporal direction contribute a factor $\cos(n\varphi)$ to the condensate. Hence, the condensate may be written as a series in $\cos(n\varphi)$: $\langle\bar{\psi}\psi\rangle_\varphi = \sum_{n=0}^{N} a_n \cos(n\varphi)$. Indeed, this is what we see in the left diagram of fig. 3.3. Below the phase transition temperature the condensate is practically angular independent and above the phase transition temperature we find a clear cosine-type shape, in agreement with the expectation from the series expansion and lattice results of ref. [84]. Furthermore, at sufficiently large quark masses we expect large loops to be suppressed by powers of $1/m$. As a result only loops winding once around the temporal direction should contribute in (3.6) and the resulting angular behavior of the condensate should be proportional to $\cos(\varphi)$. For our largest quark mass the result can be well fitted by terms up to $n \leq 2$ and the first term is by far the largest contribution. For the smaller quark mass we observe also sizable contributions from terms $\cos(n\varphi)$ with $n > 2$. In the plot, these contributions are responsible for the flat area around the antiperiodic boundary angle $\varphi = \pi$. In the right diagram of fig. 3.3 we compare the angular dependence of the condensate at $T = 1.81\,T_c$ for the two finite quark masses

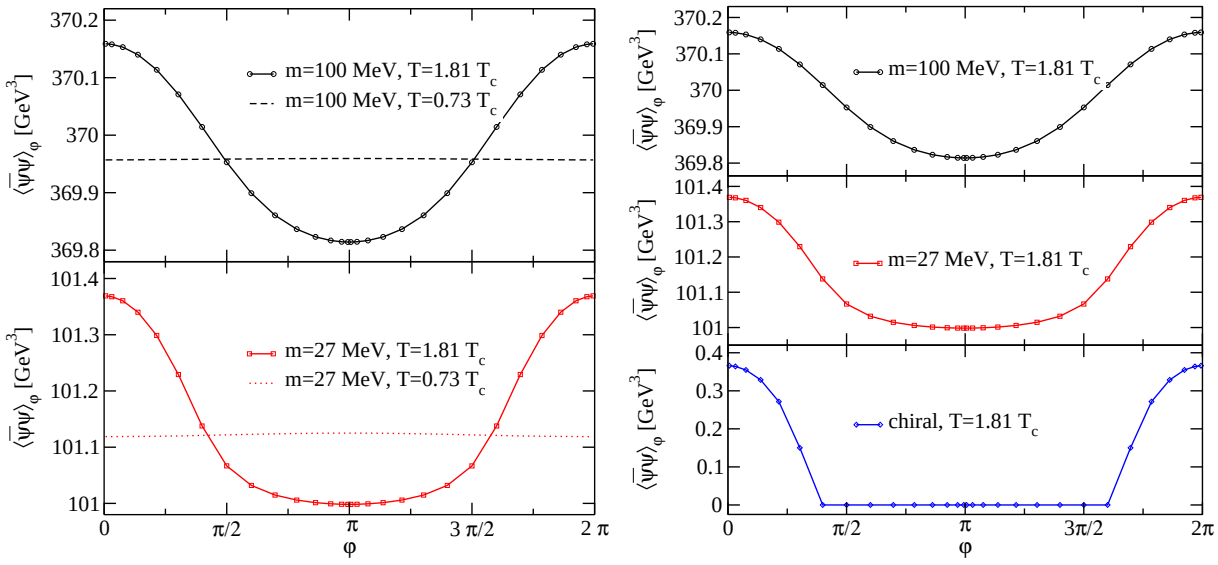

Figure 3.3: Angular dependence of the quark condensate. Shown are results for gauge group SU(3). Left diagram: The condensate for temperatures below and above the deconfinement temperature and for two different quark masses. Right diagram: Results above the deconfinement temperature. In addition to the quark masses already considered in the left diagram also the condensate in the chiral limit is shown.

already considered in the left diagram and also in the chiral limit. Approaching the chiral limit the area around the antiperiodic boundary angle $\varphi = \pi$ becomes flatter and finally develops a derivative discontinuity at two finite values of $\varphi = \pi \pm L$. These indicate the breakdown of the loop expansion (3.6) in the chiral limit. Note that this is also the limit where the condensate is free of quadratic ultraviolet divergences and the continuum limit can be taken; another reason why the loop expansion (3.6) is no longer applicable.

A combined plot of the angular and temperature dependence of the chiral limit condensates for SU(2) and SU(3) is shown in figs. 3.4 and 3.5. The behavior of the condensates of both gauge groups differs only in details. In both gauge groups we observe a similar φ-dependent evolution of the quark condensate. Whereas at periodic boundary conditions $\varphi = 0, 2\pi$ the condensate is monotonically rising, cf. the black curve in the diagram in fig. 3.6, it clearly shows signals for a phase transition for boundary angles close to antiperiodic boundary conditions $\varphi = \pi$. Indeed for angles around $\varphi = \pi$, one could (formally) define a φ-dependent transition temperature that is related to the width L of the plateau. A slight difference in SU(2) and SU(3) is discernible at the critical temperature where the plateau emerges. For SU(3) the results suggest that the plateau emerges discontinuously

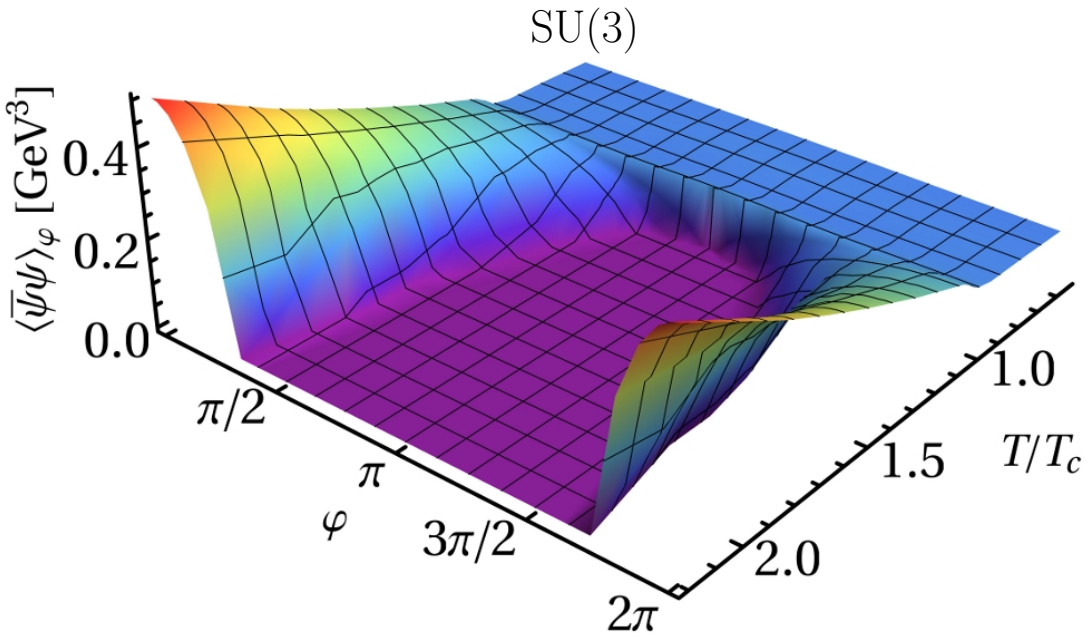

Figure 3.4: A 3d-plot of the angular and temperature dependence of the chiral quark condensate for SU(3).

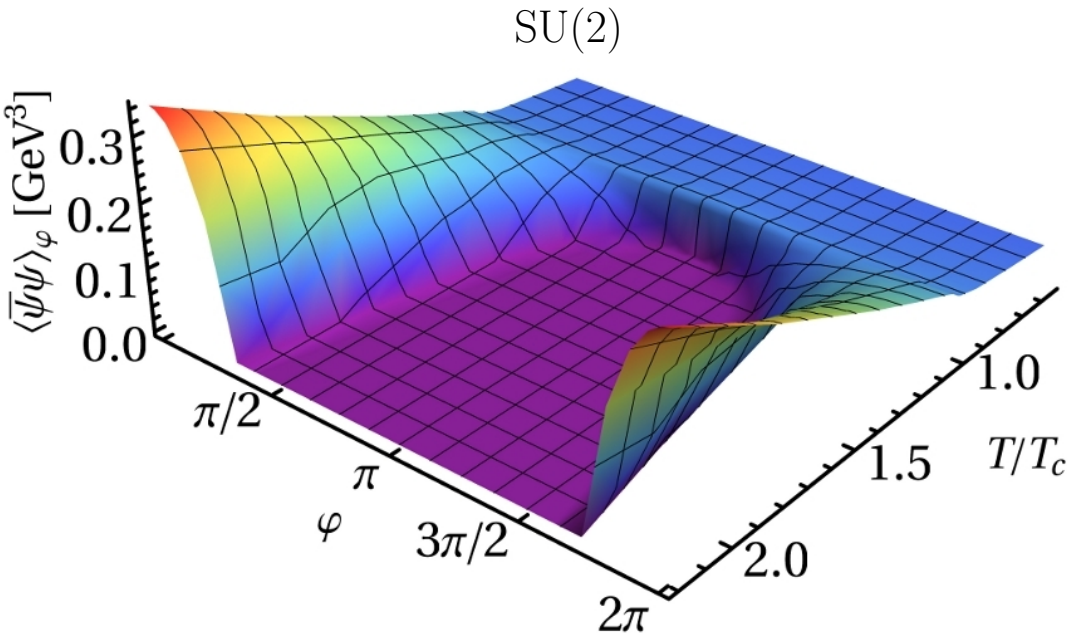

Figure 3.5: The same 3d-plot as in fig. 3.4 now for SU(2).

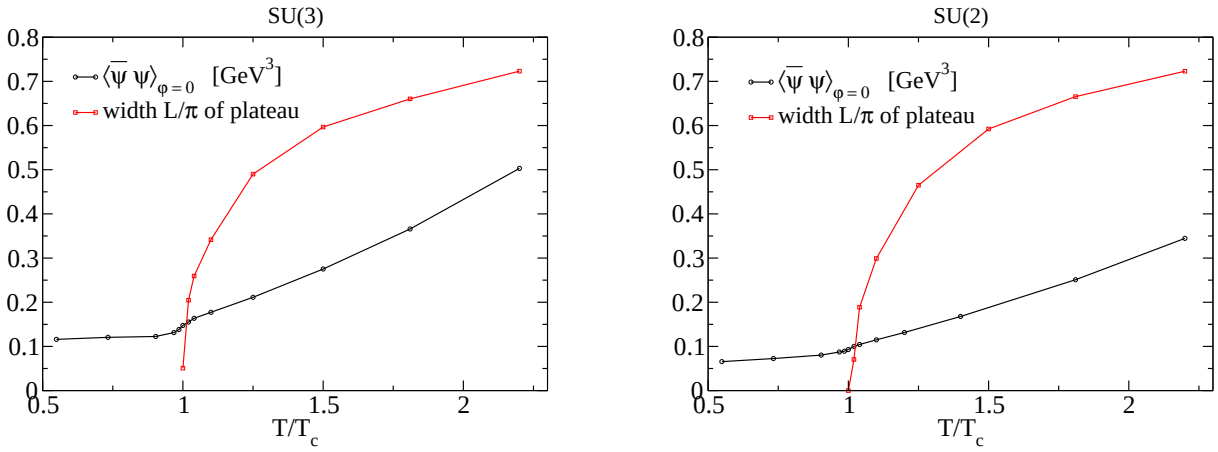

Figure 3.6: Temperature dependence of the half-width L of the plateau in the chiral quark condensate in units of π (i.e. $L/\pi = 1$ means that the plateau extends over all angles $\varphi = 0 \ldots 2\pi$) and temperature dependence of the chiral quark condensate $\langle\bar{\psi}\psi\rangle_\varphi$ at periodic boundary conditions $\varphi = 0$. Left diagram SU(3) and right diagram SU(2) data.

with a finite width whereas the plateau width seems to increase continuously in the case of SU(2). The dependence of the massive quark condensate as function of (T, φ) is similar to its chiral counterpart. The most pronounced difference is that there is no plateau around $\varphi = \pi$, but instead a cosine-shaped dip as can be inferred from fig. 3.3.

In fig. 3.6 we show the temperature dependence of the half-width L of the plateau in the chiral quark condensate in units of π. The width of the plateau is zero below the critical temperature T_c and rises quickly above, spreading up to $L/\pi \approx 0.75$ at $T = 2.2T_c$. The presumably continuous and discontinuous emergence of the plateau for SU(2) and SU(3) indicated in the 3d plots is more clearly recognizable in this figure.

The monotonic rise slows down for temperatures $T > 1.25\,T_c$. However, from the presently available results up to $T = 2.2T_c$ one cannot exclude that the plateau finally extends over the whole range of boundary angles $\varphi = 0 \ldots 2\pi$ for $T \to \infty$.

The chiral condensate at periodic boundary conditions $\langle\bar{\psi}\psi\rangle_{\varphi=0}$ is also a monotonic function of temperature, as shown in the same plot. From a naive dimensional analysis one might expect that it rises proportional to the third power of temperature for high temperatures. However, an analytic analysis shows that

$$\langle\bar{\psi}\psi\rangle_{\varphi=0}(T) \sim T^2 \quad \text{for } T \gg T_c\,. \tag{3.11}$$

We implicitly assumed that at large enough temperatures the temperature effects in the gluon dressing functions and the vector dressing functions A and C of the quark propa-

gator and the quark-gluon vertex are arbitrary weak and therefore can be neglected. In order to derive this result we first analyze the large temperature limit of the qDSE (2.60) for the scalar quark dressing function. With periodic boundary conditions $\varphi = 0$ only the zeroth Matsubara frequency, $\omega_{n_p} = 0$, contributes in the Matsubara sum; all others are suppressed by powers of the temperature T. We can therefore neglect the Matsubara frequencies in the arguments of dressing functions and the vertex only depends on the gluon three momentum. Working in the chiral limit, we then have

$$\begin{aligned} B(\boldsymbol{p},T) &\sim T\int \frac{d^3q}{(2\pi)^3}\,\frac{B(\boldsymbol{q},T)}{\boldsymbol{q}^2+B^2(\boldsymbol{q},T)}\frac{3\Gamma(\boldsymbol{q}-\boldsymbol{p})}{(\boldsymbol{q}-\boldsymbol{p})^2} \\ &\sim T\int dq\frac{B(\boldsymbol{q},T)}{\boldsymbol{q}^2+B^2(\boldsymbol{q},T)}\,. \end{aligned} \tag{3.12}$$

The second line follows from the first line because of the temperature independence of the terms in the angular integral. The resulting integral in eq. (3.12) is dominated from low momenta, $\boldsymbol{q}^2 < B^2(\boldsymbol{q},T)$, and consequently the integrand scales like $1/B(\boldsymbol{q},T)$ leading to

$$B(\boldsymbol{p},T) \sim \sqrt{T} \qquad \text{for } T \gg T_c\,, \tag{3.13}$$

in agreement with numerical results discussed in refs. [41, 86]. We also confirmed that indeed the scaling of $B(\boldsymbol{p},T)$ with T is independent of the three-momentum $\boldsymbol{p}$.

Having identified the large temperature scaling of $B(\boldsymbol{p},T)$, we now analyze the integral for the quark condensate, eq. (3.4), given by

$$\begin{aligned} \langle\bar\psi\psi\rangle_{\varphi=0} &= 4\,Z_2\,N_c\,T\sum_{\omega_p}\int\frac{d^3p}{(2\pi)^3}\,\frac{B}{\omega_{n_p}^2C^2+\boldsymbol{p}^2A^2+B^2}\,, \\ &\sim T\int dp\,\boldsymbol{p}^2\frac{B(\boldsymbol{p},T)}{\boldsymbol{p}^2+B^2(\boldsymbol{p},T)}\,. \end{aligned} \tag{3.14}$$

Here, the second line is obtained by again neglecting the temperature scaling of the vector dressing functions A, C and the contributions of all but the lowest Matsubara frequency. The resulting integral has an extra factor of $\boldsymbol{p}^2$ as compared to the one in eq. (3.12). It is therefore not dominated by momenta smaller than B^2. Recalling that $B(0,T) \sim B(\boldsymbol{p},T) \sim \sqrt{T}$ we proceed by the integral transformation $p \to p'B(0,T)$ which leads to

$$\begin{aligned} \langle\bar\psi\psi\rangle_{\varphi=0} &\sim T\int dp'\,\boldsymbol{p}'^2B^3(0,T)\,\frac{B(\boldsymbol{p},T)}{B^2(\boldsymbol{p},T)\,(\boldsymbol{p}'^2B^2(0,T)/B^2(\boldsymbol{p},T)+1)}\,, \\ &\sim T^2\,, \qquad \text{for } T \gg T_c\,. \end{aligned} \tag{3.15}$$

Due to the limited temperature range up to $2.2\,T_c$ for the gluon input, a numerical verification in the framework of the here presented truncation is impossible. However, we find agreement with the numerical results assuming temperature independence of the parameters of the gluon dressing function at high temperatures [41]. We conclude that our analytical result is not definite and may be modified by corresponding temperature dependencies.

Chiral and deconfinement transition

Our numerical results for the ordinary quark condensate, eq. (3.4) with $\varphi = \pi$, and the dressed Polyakov loop, eq. (3.5), are shown in fig. 3.7. Let us first concentrate on the results for the ordinary quark condensate. Both, for SU(2) and SU(3), we find chiral transitions taking place on a very small temperature interval. This is particularly clear in the chiral limit (lower panel) but also for quark masses as heavy as the strange quark mass (upper panel). This temperature interval clearly coincides with the one identified in the previous section for the change of behavior in the electric and magnetic screening masses. Technically what happens in the quark-DSE is that below T_c the electric, longitudinal part of the gluon propagator increases dramatically and therefore provides for extra interaction strength in the quark DSE. As a consequence, we find increasing values for the quark condensate. At or below T_c the electric part of the gluon propagator reaches its maximum and then drops sharply around and above T_c. In the quark-DSE this sudden loss of interaction strength is responsible for the dramatic decrease in the chiral condensate. It is satisfying to note that a similar behavior has been observed from calculations of the quenched condensate via Casher-Banks relations on the lattice [98]. This agreement gives us confidence that the temperature dependence of our truncation for the quark-gluon vertex, eq. (3.10), is at least qualitatively reliable and leads to meaningful results.

In the chiral limit we clearly obtain a chiral phase transition from the conventional quark condensate. Unfortunately, the temperature resolution of the lattice input is still not fine enough to unambiguously identify the order of the phase transition. One may speculate whether the SU(2) transition is second or first order, whereas the SU(3) one seems to be first order. The behavior at finite quark masses may be compatible with a rapid crossover for SU(2) and in the case of SU(3) even with a jump in the condensate signaling a remnant of a first order transition. Further investigations are necessary to clarify, whether the differences seen in fig. 3.7 between SU(2) and SU(3) are indeed significant.

As concerns the dressed Polyakov-loop we clearly find a transition between the center-symmetric low temperature phase and the center-broken phase at transition temperatures very close to the ones encountered for the conventional quark condensate. Below T_c the

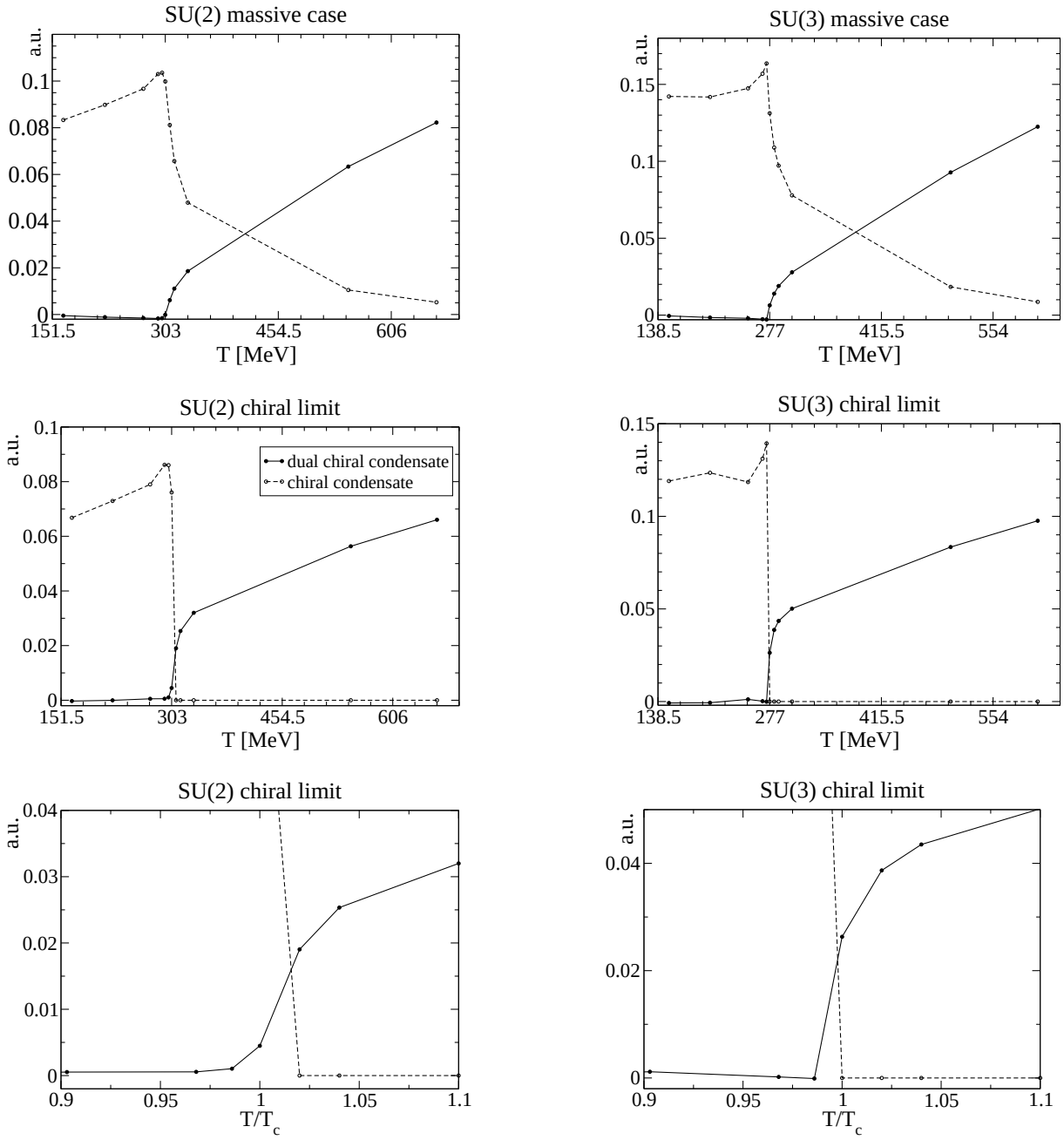

Figure 3.7: The quark condensate $\langle\bar{\psi}\psi\rangle_\pi$ and the dressed Polyakov loop Σ_1 as a function of temperature for SU(2) (left panel) and SU(3) (right panel) Yang-Mills theory. Shown are results in arbitrary units (a.u.) for a massive (strange-)quark (upper panel) with $m \approx 80$ MeV and in the chiral limit (lower panel). Lower diagrams show a close up of the dual condensate close to the transition temperature.

dressed Polyakov-loop is almost constant and very small. For large quark masses close to the transition temperature we even find small negative values of the Polyakov-loop. We interpret these as artifacts introduced due to mass dependencies in the quark-gluon vertex that are not represented by our vertex ansatz. At temperatures $T_c \leq T \leq 1.1T_c$ the Polyakov-loop rises sharply and then less steeply for larger temperatures. Within the temperature range investigated we do not yet see a saturation of the dressed Polyakov-loop at large temperatures, although the results in the chiral limit may bear some signals of such a behavior. In general, the deconfinement transition extracted from the dressed Polyakov-loop is as pronounced as the corresponding signal in the electric and magnetic screening masses of the gluon propagator, discussed in section 3.2. Although the transition is more rapid for SU(3), as can be seen from the lower line of fig. 3.7, also here the temperature resolution and the systematic quality of the input gluon propagator is not yet good enough to cleanly identify an order of the deconfinement transition.

We comment on the temperature resolution of the lattice gluon data for gauge group SU(2). In refs. [41, 85] the lattice data used as input have been available only for four different temperatures and had to be interpolated in between. This procedure generated a smooth behaviour of the gluon propagator around the critical temperature resulting also in a broad transition range as concerns the chiral condensate. Here, with our much better temperature resolution as concerns the lattice gluon, we are able to identify this behavior as an artifact of the interpolation procedure.

3.4 Summary

We studied the chiral and the deconfinement transition in SU(2) and SU(3) Yang-Mills theory using the Landau gauge quark propagator. We introduced a truncation scheme combining Dyson-Schwinger equations with lattice results for the gluon propagator as input. Due to this, a realistic temperature dependent gluon propagator is implemented and temperature effects in the quark-gluon vertex are also taken into account. The considerable changes in the gluon propagator, especially in the electric gluon dressing function around T_c, have been identified as the source of equally dramatic changes in the ordinary quark condensate as determined from the Dyson-Schwinger equation for the quark propagator: the condensate keeps rising below T_c only to decrease sharply at T_c. This behavior is in agreement with previous observations from lattice calculations of the Casher-Banks relation [98]. It also locates the mechanism for chiral symmetry restoration in Landau gauge rather unambiguously in the (ultra-)soft electric sector of the theory, emphasizing its genuine nonperturbative nature.

As for the deconfinement transition we observe a clean transition from the dressed Polyakov-loop as determined from the Dyson-Schwinger equation for the quark propagator. The corresponding transition temperatures, $T_c \approx 303$ MeV for SU(2) and $T_c \approx 277$ MeV for SU(3), agree with the ones extracted within the lattice calculation.

From these results we conclude that the dressed Polyakov loop is a well suited deconfinement order parameter for functional methods. Together with the presented truncation scheme this provide a good starting point to generalize the approach towards the inclusion of unquenching effects and the introduction of finite chemical potential.

Chapter 4

Quark Spectral Properties above T_c

Particularly with regard to the insight about the nature of the quark-gluon plasma (QGP) that is gained from the wealth of data produced by the Relativistic Heavy-Ion Collider (RHIC), a detailed understanding of the quark quasi-particle spectrum, is highly desirable. In the strongly coupled regime just above the chiral phase transition (see refs. [99–102] for recent reviews), despite the strong coupling, phenomena like the constituent quark number scaling of elliptic flow [103] still suggest quarks as quasi-particle excitations. This should also be connected with the success of quasi-particle models in describing thermodynamic properties in this regime of the QCD phase diagram [104–106] and also serves as a foundation for transport approaches like the one discussed in ref. [107]. In another context, dilepton production in a heavy ion collision has been related to the spectral properties of the thermalized quasi-particles and specifically to the dispersion relation of quarks [108–111].

There is however no straightforward approach for the determination of the spectral function beyond systematic weak-coupling expansions. Ab initio calculations of correlators within lattice QCD are performed in Euclidean space and an analytic continuation that is necessary to determine the spectral function is strictly speaking not possible. The same is still true for computations within functional approaches, such as Dyson-Schwinger and functional RG methods, at least when considering truncations beyond simple rainbow approximations.

In this chapter, we present first steps towards the determination of spectral functions in the framework of Dyson-Schwinger equations beyond simple rainbow approximations. Particularly due to our input for the gluon propagator, the DSE calculations are also limited to Euclidean space and we use a method established in refs. [38, 39] in the framework of lattice QCD. There, the authors assumed a certain shape for the quark spectral

function including a few parameters which were determined from fitting to the Euclidean numerical data. In such an approach one relies on physical guidance, as e.g. given by the HTL approximation, for the construction of a suitable ansatz for the spectral function. The truncation scheme used is largely identical with the one of the previous chapter. However, here we only consider gauge group SU(3) since our investigation is motivated by quenched SU(3) lattice calculations with which we want to compare.

This chapter is organized as follows: In section 4.1 we comment on slight modifications of the truncation scheme introduced in the previous section and briefly present our results for the quark dressing functions in Euclidean space below and above the critical temperature T_c. We then introduce the spectral representation for the quark propagator in section 4.2. The Schwinger function and a criterion for positivity violations of the spectral function are considered in section 4.3. In this section, using fit ansätze for the spectral function, we also focus on zero momentum and finite quark masses before moving to finite momentum in the chiral restored phase in section 4.4. The obtained results are confronted with recent quenched lattice QCD results from ref. [39].

4.1 Matsubara Propagator below and above T_c

Before turning to results for the propagator we need to specify the truncation setup. The input for the SU(3) gluon propagator is fixed by the lattice results as described in section 3.2. However, as already noted, the $q\bar{q}g$-vertex is only barely constrained and states an uncertainty source in our calculation. Staying for simplicity with the vertex ansatz given in eq. (3.10) it turns out that its temperature dependence is in one-to one correlation to the thermal masses m_T of the quarks as extracted in section 4.3. Since the same quantity has been determined from quenched QCD results for the Landau gauge quark propagator, see Tab. II of Ref [39], we adjust the vertex parameter d_1 such that it roughly coincides with these results. The vertex parameter, $d_2 = 0.5$ GeV^2, as well as all other quantities of the vertex ansatz are kept as before. This procedure works only above the critical temperature where thermal masses can be extracted. Below the critical temperature no such information is available and we therefore stay to the constant value $d_1 = 4.6$ GeV^2.

We certainly checked the d_1 dependence of our results for the quark spectral function below the critical temperatures; this is discussed in section 4.3. Our values of d_1 and the obtained thermal masses are summarized in tab. 4.1. Obviously, the strength of the vertex ansatz at low momenta is significantly reduced above the critical temperature. This is what one may expect: In the Dyson-Schwinger equation for the quark-gluon vertex, discussed in detail in ref. [69], skeleton diagrams containing dressed gluon propagators

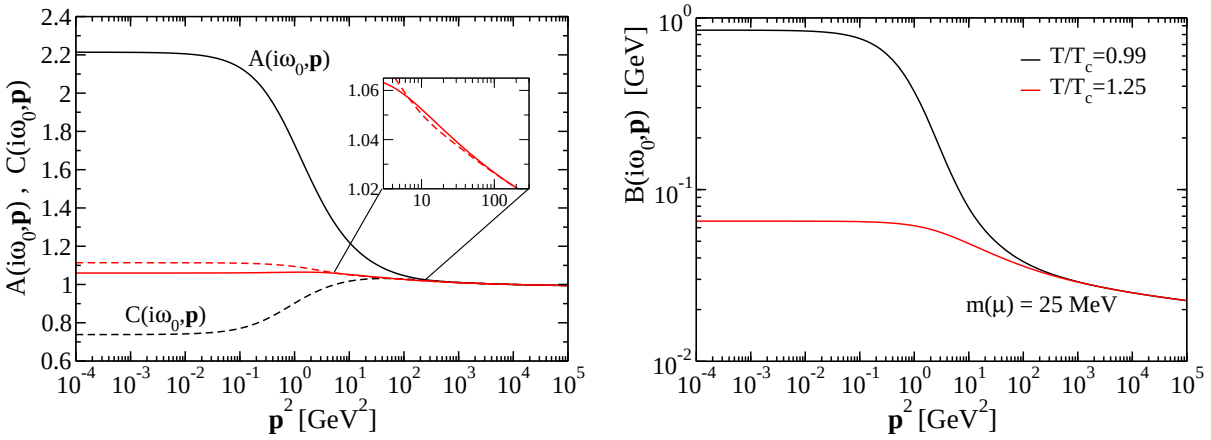

Figure 4.1: Momentum dependence of the dressing functions A, C, B below and above the critical temperature. Results are shown for the lowest Matsubara frequency and finite bare quark mass $m(\mu) = 25\,\mathrm{MeV}$.

can be extracted. The rapid decrease in the strength of the longitudinal gluon at or around the critical temperature T_c, fig. 3.1, will thus back-feed into the vertex DSE which probably explains the reduction of the strength of the quark-gluon vertex. This behavior fits nicely to our findings for the parameter d_1 in our ansatz for the vertex. We therefore believe that our vertex ansatz accurately reflects qualitative and maybe even quantitative features of the fully dressed quark-gluon vertex.

Having fixed our input in the qDSE we briefly discuss our results for the Matsubara propagator in momentum space shown in fig. 4.1. We show results for $m(\mu) = 25$ MeV with $\mu^2 = 10545$ GeV^2. This corresponds roughly to a strange quark mass. Above T_c the interaction strength as parameterized by the quark-gluon vertex is strongly reduced and the dressing functions $A(i\omega_0, \boldsymbol{p})$ and $C(i\omega_0, \boldsymbol{p})$, which are finite in Landau gauge, do not deviate much from unity. In the infrared all dressing functions are constant and we observe that $A(i\omega_0, \boldsymbol{p}) < C(i\omega_0, \boldsymbol{p})$. This is also found for the dressing functions in HTL

Table 4.1: Temperature dependent parameter for the quark-gluon vertex and extracted thermal masses m_T.

T/T_c	< 1	1.25	1.5	2.2
d_1 [GeV^2]	4.6	0.5	0.4	0.25
m_T/T		0.865	0.862	0.822

approximation [75], where this inequality holds for all momenta. In the simplified case of constant dressing functions this is perfectly consistent with our expectations: As can be seen from the Dirac decomposition of the propagator, eq. (2.62), we would interpret $\sqrt{A/C} = v \leq 1$ as the velocity of the quasi-particles, $\sqrt{v^2\boldsymbol{p}^2 + B^2/C^2}$ as their dispersion relation and $1/C \leq 1$ as the wave-function renormalization of the γ_4-component[1]. In contrast to the HTL approximation there is, however, a momentum range (8 GeV^2 to 200 GeV^2 in fig. 4.1) where $A(i\omega_0, \boldsymbol{p}) > C(i\omega_0, \boldsymbol{p})$ for all here considered temperatures above T_c and all masses. To what extent this behavior is generic or truncation-affected needs to be investigated in future studies.

Below T_c, on the contrary, the results become less intuitive. Due to the stronger interaction and lower temperature, the chiral symmetry breaking dressing function B is significantly larger in the infrared with its size related to the scale of dynamical symmetry breaking. For the dressing functions $A(i\omega_0, \boldsymbol{p})$ and $C(i\omega_0, \boldsymbol{p})$ we find, however, $A(i\omega_0, \boldsymbol{p}) > C(i\omega_0, \boldsymbol{p})$. This does not allow for a simple quasi-particle interpretation as outlined above. Also the contribution from the self-energy is of the same order as the free propagator, in particular the dressing function $A(i\omega_0, \boldsymbol{p})$ is strongly enhanced in the infrared. This also hints towards more complicated dynamics than a gas of quasi-particles, which is of course expected in the confined phase of QCD.

From these results we therefore conclude that a simple interpretation in terms of the excitation spectrum seems not appropriate below T_c. Even for the analysis above T_c, as we discuss in the following, the quasi-particles can receive a thermal mass in the chiral restored phase. This is already known from the HTL expansion, where the quasi-particles in the high temperature and small coupling regime have a mass of order gT.

4.2 Quark Spectral Function and Representation

Causality and resulting analyticity imply that a correlator can be represented through a spectral function. For the quark propagator this representation is given by

$$S(i\omega_n, \boldsymbol{p}) = -\int_{-\infty}^{\infty} \frac{d\omega'}{2\pi} \frac{\rho(\omega', \boldsymbol{p})}{i\omega_n - \omega'}\,, \tag{4.1}$$

where the Dirac structure of the spectral function is parameterized as

$$\rho(\omega, \boldsymbol{p}) = -i\gamma_4\, \rho_4(\omega, |\boldsymbol{p}|) - \rho_{\mathrm{v}}(\omega, |\boldsymbol{p}|)\, (\boldsymbol{\gamma}\cdot\boldsymbol{p})/|\boldsymbol{p}| + \rho_{\mathrm{s}}(\omega, |\boldsymbol{p}|)\,. \tag{4.2}$$

[1] Note that only the γ_4-component of the quark propagator obeys a sum rule [112].

Our conventions are chosen such that they agree up to the momentum normalization with those in ref. [75] using Minkowski space conventions[2]. Assuming a positive definite Fock space[3], the dressing functions furthermore obey

$$\rho_4(\omega, |\boldsymbol{p}|) \geq \sqrt{\rho_{\mathrm{v}}(\omega, |\boldsymbol{p}|)^2 + \rho_{\mathrm{s}}(\omega, |\boldsymbol{p}|)^2} \geq 0 \tag{4.3}$$

and the sum rules

$$1 = Z_2 \int_{-\infty}^{\infty} \frac{d\omega}{2\pi}\, \rho_4(\omega, |\boldsymbol{p}|)\,, \tag{4.4}$$

$$0 = \int_{-\infty}^{\infty} \frac{d\omega}{2\pi}\, \rho_{\mathrm{v}}(\omega, |\boldsymbol{p}|)\,, \tag{4.5}$$

$$0 = \int_{-\infty}^{\infty} \frac{d\omega}{2\pi}\, \rho_{\mathrm{s}}(\omega, |\boldsymbol{p}|)\,, \tag{4.6}$$

where here Z_2 is the wave function renormalization constant and not the plasmino residue which will be introduced later.

In the following we limit ourself to vanishing momenta $|\boldsymbol{p}|$ and the chiral restored phase, respectively. For this purpose it is instructive to introduce the projectors

$$\begin{aligned} P_{\pm}(\boldsymbol{p}) &= \frac{1}{2}\left(1 \mp i\gamma_4\, (\boldsymbol{\gamma}\cdot\boldsymbol{p})/|\boldsymbol{p}|\right)\,, \\ L_{\pm} &= \frac{1}{2}\left(1 \mp i\,\gamma_4\right)\,, \end{aligned} \tag{4.7}$$

where the signs are again chosen in order to agree with common Minkowski space conventions. $P_{\pm}(\boldsymbol{p})$ can be interpreted as energy projectors for massless modes.

For vanishing momentum it is then convenient to write

$$\rho(\omega, \mathbf{0}) = -i\left(\rho_+^M(\omega) L_+\gamma_4 + \rho_-^M(\omega) L_-\gamma_4\right)\,, \tag{4.8}$$

$$S(i\omega_n, \mathbf{0}) = -i\left(S_+^M(i\omega_n) L_+\gamma_4 + S_-^M(i\omega_n) L_-\gamma_4\right)\,, \tag{4.9}$$

i.e. $\rho_{\pm}^M(\omega) = \rho_4(\omega, \mathbf{0}) \pm \rho_{\mathrm{s}}(\omega, \mathbf{0})$ and $\rho_{\mathrm{v}}(\omega, \mathbf{0}) = 0$. From eqs. (4.3) and (4.6) we infer that the functions $\rho_{\pm}^M(\omega)$ are positive semi-definite and normalized to Z_2. Furthermore the spectral representation yields the scalar relation

$$S_{\pm}^M(i\omega_n) = -\int_{-\infty}^{\infty} \frac{d\omega'}{2\pi}\, \frac{\rho_{\pm}^M(\omega')}{i\omega_n - \omega'}\,. \tag{4.10}$$

[2] $\gamma_{\mathrm{M}}^{\mu}$ in common Minkowski space conventions are related to those used in this work via $\gamma_{\mathrm{M}}^0 = -i\,\gamma_4$ and $\gamma_j = \gamma_{\mathrm{M}}^j$.

[3] For completeness we note that this is not guaranteed for a gauge-fixed Yang-Mills theory.

On the other hand for a chirally symmetric phase with $B(i\omega, |\boldsymbol{p}|) = 0$ and $\rho_{\mathrm{s}}(\omega, |\boldsymbol{p}|) = 0$, we introduce

$$\rho(\omega, \boldsymbol{p}) = -i \sum_{e=\pm} \rho_e^P(\omega, |\boldsymbol{p}|)\, P_e(\boldsymbol{p})\, \gamma_4\,, \tag{4.11}$$

$$S(i\omega_n, \boldsymbol{p}) = -i \sum_{e=\pm} S_e^P(\omega, |\boldsymbol{p}|)\, P_e(\boldsymbol{p})\, \gamma_4\,, \tag{4.12}$$

i.e. $\rho_\pm^P(\omega, |\boldsymbol{p}|) = \rho_4(\omega, |\boldsymbol{p}|) \pm \rho_{\mathrm{v}}(\omega, |\boldsymbol{p}|)$. As before we see that $\rho_\pm^P(\omega, |\boldsymbol{p}|)$ is positive semi-definite and normalized to Z_2. The spectral representation for the dressing functions again take the form

$$S_\pm^P(i\omega_n, |\boldsymbol{p}|) = -\int_{-\infty}^{\infty} \frac{d\omega'}{2\pi}\, \frac{\rho_\pm^P(\omega', |\boldsymbol{p}|)}{i\omega_n - \omega'}\,. \tag{4.13}$$

In the following, we aim to invert the linear relation between Matsubara propagators $S_\pm^M(i\omega_n)$, $S_\pm^P(i\omega_n, \boldsymbol{p})$ determined by solving the truncated DSE and the respective spectral functions $\rho_\pm^M(\omega)$ and $\rho_\pm^P(\omega, |\boldsymbol{p}|)$. Strictly speaking, for a finite set of Matsubara frequencies, this problem is however ill-posed.

4.3 Quark Spectral Function at Zero Momentum

In this section, we focus our attention to the quark propagator at zero momentum. We analyze the correlator at temperatures below and above the critical temperature and for various bare quark masses. Since the general problem of extracting the spectral function from the spectral representation is ill-posed, we will limit ourselves to parameterized ansätze and determine the best fitting function in the given subspace. Above the critical temperature we study the quark mass dependence of the so obtained insight on quasi-particle excitations. This strategy was explored in refs.[38, 39] in the framework of lattice QCD.

We will mainly consider the following two-pole ansatz for the spectral function

$$\rho_\pm^M(\omega) = 2\pi\big[Z_1\delta(\omega \mp E_1) + Z_2\delta(\omega \pm E_2)\big]\,, \tag{4.14}$$

with fitting parameters $Z_1,\ Z_2$ and $E_1,\ E_2$. This will be related to our quark propagator via eq. (4.10), for which we identify

$$S_\pm^{\mathrm{DSE},\,M}(i\omega_n) = \frac{i\omega_n\, C(i\omega_n, 0) \pm B(i\omega_n, 0)}{\omega_n^2\, C^2(i\omega_n, 0) + B^2(i\omega_n, 0)}\,. \tag{4.15}$$

Our choice is suggested by HTL results at high temperatures and small coupling. In contrast to a non-interacting fermion, whose spectral function consists of a single δ-function, it is known from HTL that an additional collective excitation develops: the plasmino. The fitting parameters $E_{1,2}$ denote the quasi-particle energies and $Z_{1,2}$ the corresponding residues. Certainly the full spectral function will be more complicated. The working assumption here is, that if quasi-particle excitations with small decay widths exist, then their peaks will be the dominant contribution of the spectral function and therefore such a simple ansatz may reveal characteristics of the quasi-particles and their dispersion relations. However, we emphasize again that in HTL calculations the thermal masses $E_{1/2}$ are of order gT, whereas the width of the corresponding peaks in the spectral functions are of order g^2T. In a strong coupling regime this becomes of the same order, if not larger.

Likewise, as done in ref. [39], we also investigated other ansätze for the spectral function. We considered a single pole ansatz

$$\rho_{\pm}^{M}(\omega) = 2\pi Z_1 \delta(\omega \mp E_1)\,, \tag{4.16}$$

and ansätze allowing for one- and two-particle excitations with Gaussian widths

$$\rho_{\pm}^{M}(\omega) = 2\sqrt{\pi}\,\frac{Z_1}{\Gamma_1}\exp\frac{-(\omega \mp E_1)^2}{\Gamma_1^2}\,, \tag{4.17}$$

$$\rho_{\pm}^{M}(\omega) = 2\sqrt{\pi}\left[\frac{Z_1}{\Gamma_1}\exp\frac{-(\omega \mp E_1)^2}{\Gamma_1^2} + \frac{Z_2}{\Gamma_2}\exp\frac{-(\omega \pm E_2)^2}{\Gamma_2^2}\right]. \tag{4.18}$$

Here, Γ_1 and Γ_2 are additional fitting parameters.

In order to evaluate the quality of the fit we minimize

$$\ell_{\pm}^2 = \sum_{n}^{N_\omega}\left|S_{\pm}^{\mathrm{DSE},\,M}(i\omega_n) - S_{\pm}^{M}(i\omega_n)\right|^2\,, \tag{4.19}$$

i.e. we implicitly assume uncorrelated data with equal total errors. For comparing the different fit forms we evaluate ℓ_{+}^2 with $N_\omega = 39$. In principle, one may also define $\ell_{\pm}^2/\mathrm{dof}$ where dof denotes N_ω minus the number of fit parameters however this does not affect our results.

A remark on the numerical results seems appropriate here. Within a given truncation scheme the error in Dyson-Schwinger calculations is essentially determined by the error of the numerical integration. It can be estimated by varying the numerical parameters of the integration and can be made significantly smaller than in lattice calculations. At least for large temperatures where the Matsubara frequencies are largely separated, the assumption of uncorrelated errors seems reasonable. In principle, the self-energy is calculated in DSE

calculations and the total error appears for the inverse propagator, which grows linearly in frequencies ω_n. By using eq. (4.19) we therefore enhance the importance of small ω_n. We expect the relevant information for spectral functions to be encoded here as the propagator approaches the perturbative result at large frequencies very fast.

For the data analyzed, we find ℓ_+^2 more than one order of magnitude smaller for fits based on eq. (4.14) than for the single pole Ansatz eq. (4.16). This is in accordance with the findings in ref. [39]. Comparing ℓ_+^2 obtained from the single peak ansatz eq. (4.17) with its value obtained for ansatz (4.14) we find similar results for light quarks ($m/T \lesssim 0.2$) but roughly one order of magnitude difference in favor of (4.14) for heavy quarks ($m/T \gtrsim 0.2$).

Examining ansatz (4.18) we find parameters with improved ℓ_+^2 compared to the two pole ansatz. However, depending on the initial parameter values different local minima may be found. Typical solutions correspond to a normal mode with a width which tends to zero and a plasmino mode with broad width. Furthermore, we find that the possible excitations do not acquire a thermal mass in the chiral limit. In ref. [39] it was found that ansatz (4.18) may improve χ^2/dof for uncorrelated fits but reduces to two delta functions for correlated fits. By way of comparison and taking into account the results of [39] for correlated data we focus the discussion to the two-pole ansatz in the following.

Results above and below the critical temperature

Before analyzing the quark mass dependence of the fit parameters we investigate the propagator below and above the critical temperature. Here, T_c is given by the deconfinement transition as extracted in the previous section from the dressed Polyakov loop from the propagator and from the lattice simulations of our input gluon propagator. We note that the chiral transition temperature coincides with T_c within a few MeV, depending slightly on the bare quark mass.

In fig. 4.2 we show the Schwinger function defined by the Fourier transform of $S_+^M(i\omega_n)$:

$$S_+^M(\tau) = T \sum_n e^{-i\omega_n \tau} S_+^M(i\omega_n)\,. \tag{4.20}$$

From charge conjugation invariance it follows that $S_\pm^M(\tau) = S_\mp^M(1/T - \tau)$. The numerical data are denoted by data points. Above T_c the solid lines are obtained by using the spectral function obtained from fitting with ansatz (4.14). Note that the points close to $\tau T = 0$ and $\tau T = 1$ are subject to boundary effects due to the finite number of Matsubara modes used when Fourier transforming.

At zero temperature the Schwinger function has been used to search for positivity violations in the quark propagator. From the Osterwalder-Schrader axioms of Euclidean quantum field theory one knows that the Schwinger function needs to be strictly positive

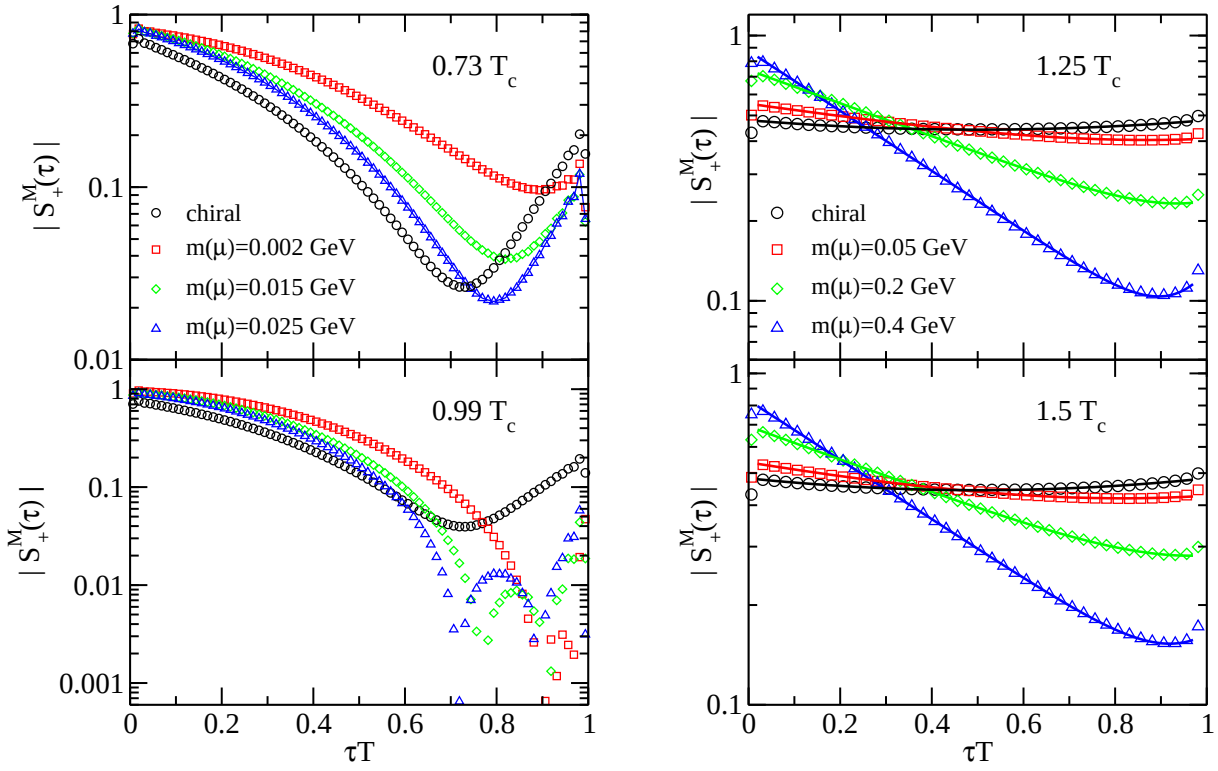

Figure 4.2: Schwinger function $S_+^M(\tau)$ for different temperatures and current quark masses. For $T = 0.99T_c$ and $m(\mu) = 0.2,\, 0.4\,\mathrm{GeV}$ the Schwinger function changes sign in an interval around $\tau T \approx 0.8$.

for physical particles. At finite temperature we can express the Schwinger function using the spectral representation (4.10) in (4.20) as

$$\begin{aligned} S_+^M(\tau) &= -T \int \frac{d\omega'}{2\pi} \rho_+^M(\omega') \sum_n \frac{e^{-i\omega_n \tau}}{i\omega_n - \omega'} \\ &= \int \frac{d\omega'}{2\pi}\, \rho_+^M(\omega')\, \underbrace{\frac{e^{(1/2-\tau T)\omega'/T}}{e^{\omega'/2T} + e^{-\omega'/2T}}}_{>0} . \end{aligned} \tag{4.21}$$

Hence, we conclude that a positive spectral function always yields a positive Schwinger function. Conversely, positivity violations in the Schwinger function imply a non-positivity of the spectral function and are therefore sufficient for the absence of the corresponding particle from the physical spectrum of a theory. This is an alternative confinement criterion.

In fact we are able to prove a more weak criterion for non-positivity of the spectral

function. This criterion relies on the curvature of the Schwinger function. Even for positive $S_+^M(\tau)$, non-positivity of the spectral function is implied if $\ln(S_+^M(\tau))$ possesses concave curvature for some τ. Conversely

$$\rho_+^M(\omega) \geq 0 \quad \Rightarrow \quad \frac{\partial^2}{\partial\tau^2} \ln S_+^M(\tau) \geq 0\,. \tag{4.22}$$

To derive this note that from eq. (4.21) we find

$$\frac{\partial^2}{\partial\tau^2} \ln S_+^M(\tau) = -\left(\frac{\int \tilde{\rho}(\omega)\omega\, d\omega}{\int \tilde{\rho}(\omega)\, d\omega}\right)^2 + \frac{\int \tilde{\rho}(\omega)\omega^2\, d\omega}{\int \tilde{\rho}(\omega)\, d\omega} \tag{4.23}$$

where we defined $\tilde{\rho}(\omega) := e^{-\tau\omega}\rho_+^M(\omega)/(1+\exp(-\frac{\omega}{T}))$. Obviously if $\rho_+^M(\omega) \geq 0$ than also $\tilde{\rho}(\omega) \geq 0$. In this case, positivity of (4.23) follows from the Cauchy-Schwarz inequality. For $\lambda \in \mathbb{R}$:

$$\int d\omega\, \tilde{\rho}(\omega)(\omega-\lambda)(\omega-\lambda) = \int d\omega\, \tilde{\rho}(\omega)\,\omega^2 - 2\lambda \int d\omega\, \tilde{\rho}(\omega)\,\omega + \lambda^2 \int d\omega\, \tilde{\rho}(\omega) \geq 0\,. \tag{4.24}$$

Choose the value $\lambda = (\int d\omega\, \tilde{\rho}(\omega)\,\omega)/(\int\, d\omega\, \tilde{\rho}(\omega))$. This yields

$$\int d\omega\, \tilde{\rho}(\omega)\,\omega^2 - \frac{\left(\int d\omega\, \tilde{\rho}(\omega)\,\omega\right)^2}{\int d\omega\, \tilde{\rho}(\omega)} \geq 0 \tag{4.25}$$

and therewith $(\partial^2 \ln S_+^M(\tau))/(\partial\tau^2) \geq 0$. Hence, concave curvature of $\ln(S_+^M(\tau))$ is a sufficient criterion for positivity violations of the spectral function and in this sense for confinement. We stress that this does not mean that a spectral representation exists for a positive Schwinger function with $(\partial^2 \ln S_+^M(\tau))/(\partial\tau^2) \geq 0$.

Having discussed the relation between the Schwinger function and confinement we now analyze our results shown in fig. 4.2. For the quark propagator at zero temperature positivity violations of the Schwinger function have been investigated in a number of works, see [113, 114] and refs. therein. At finite temperature it has been suggested from calculations in a simple model, that explicit positivity violations in the Schwinger function occur below the critical temperature, whereas positivity is restored above T_c [79]. Although we do not find explicit positivity violations in the Schwinger function for all considered mass and temperature values below T_c, we indeed find concave curvature of the logarithm of the Schwinger function below T_c. The concave curvature is recognizable in the left diagrams of fig. 4.2 around $\tau T \approx 0.5$. From eq. (4.22) we therefore reason positivity violations of the spectral function. This is in line with quenched lattice QCD results that directly determine $S_+^M(\tau)$ [39]. For completeness, we note that we find explicit positivity violations of the Schwinger function at $T = 0.99\,T_c$ for a range in current quark

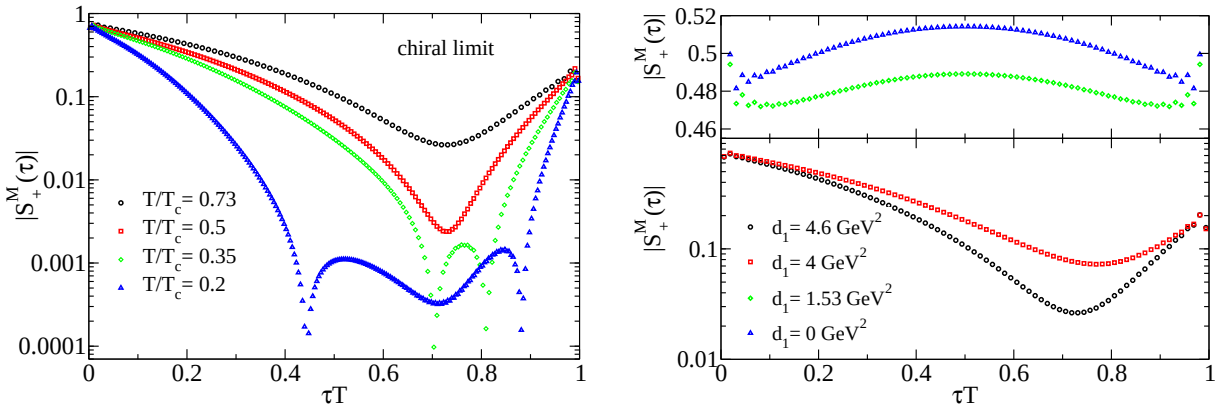

Figure 4.3: Left diagram: Schwinger functions $S_+^M(\tau)$ approaching the zero temperature limit. Shown are result for four different temperatures below the deconfinement temperature in the chiral limit. Right diagram: Dependence of the Schwinger function on the vertex parameter d_1. The upper part shows extreme values of d_1 not allowing for spontaneous chiral symmetry breaking.

masses, albeit this effect is not seen in the chiral limit. However, in this case the effect emerges when approaching the zero temperature limit, as shown in the left diagram of fig. 4.3.

Above the critical temperature $S_+^M(\tau)$ is positive and found to be convex on a log-scale. Furthermore, chiral symmetry restoration through $B(i\omega_n, 0) = 0$ translates into $S_+^M(i\omega_n) = -S_+^M(-i\omega_n)$ and $S_+^M(\tau) = S_+^M(1/T - \tau)$. We see this symmetry emerge when decreasing the current quark mass $m(\mu)$. Related to dynamical symmetry breaking this symmetry is absent below T_c, even in the chiral limit. This finding again agrees with quenched lattice calculations in ref. [39].

In order to show that confinement via positivity violations of the spectral function is not a truncation artifact of our numerical calculations we investigate the dependence of the Schwinger function on the vertex parameter d_1. This is shown in the right diagram of fig. 4.3. We find concave curvature below the deconfinement transition temperature T_c also for values of d_1 that do not allow for spontaneous dynamical mass generation. This shows that the positivity violations found in the numerical calculation cannot be attributed to the dynamical generation of quark masses. Hence, they have nothing to do with chiral symmetry breaking but rather with the non-perturbative, confining nature of the gluon propagator. It is therefore apparent, that the curvature of the Schwinger function may serve as another source for extracting the deconfinement transition temperature T_c from

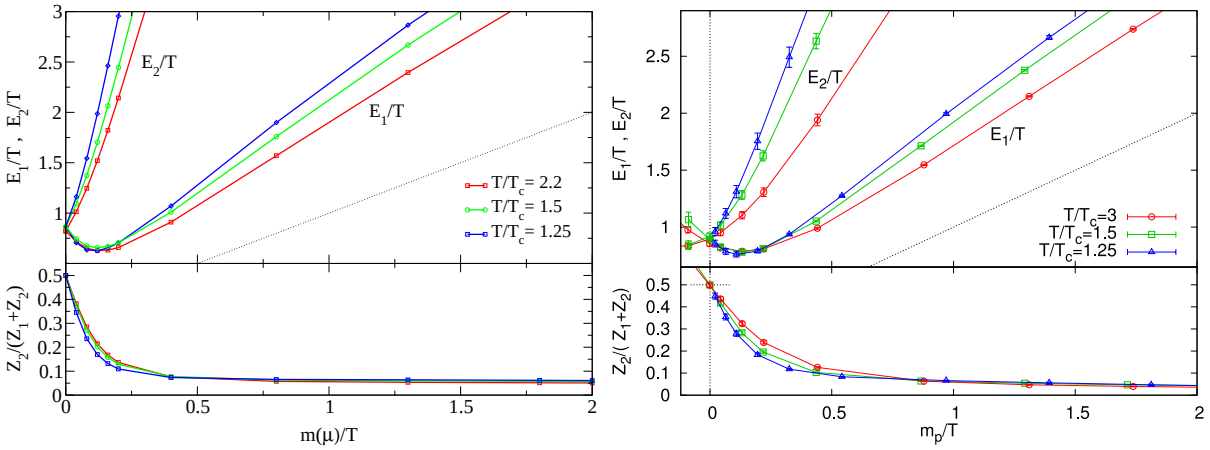

Figure 4.4: Dependence of fit parameters on bare quark mass in two-pole ansatz at vanishing momentum. For the two branches in the upper plot we define $E_2 \geq E_1$. Left diagram: Result extracted from Dyson-Schwinger calculations. Right diagram: Lattice result from ref. [39].

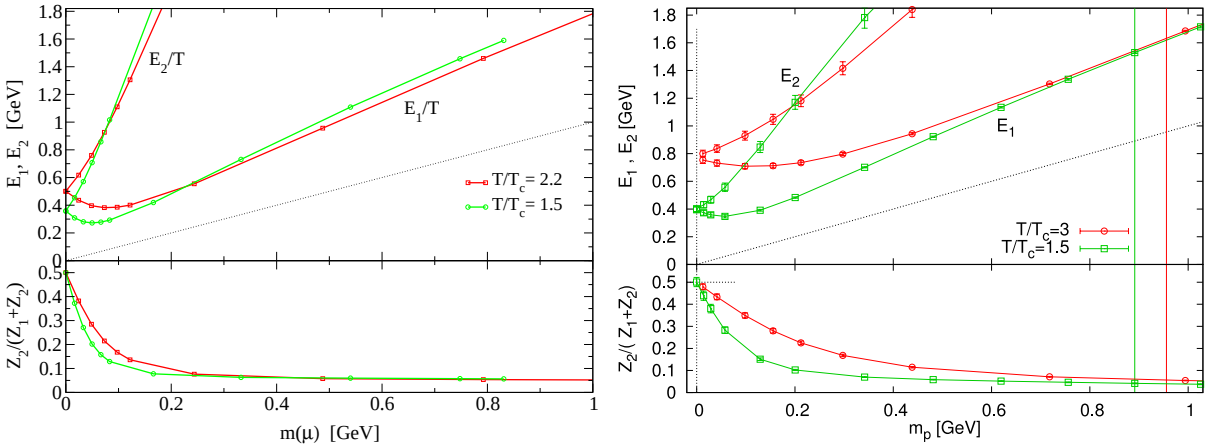

Figure 4.5: Fit parameters in physical units for two temperatures. Left diagram: Dyson-Schwinger results. Right diagram: Lattice result ref. [39].

the quark propagator besides the dressed Polyakov loop [80, 85, 86].

Quark mass dependence of fit parameters

In figures. 4.4 and 4.5 the dependence of the poles E_1, E_2 on the bare quark mass $m(\mu)$ for different temperatures is shown. In figure 4.4 we consider three different temperatures and use dimensionless variables by normalization with T. The results in physical units for the temperatures $T = 1.5\ T_c$ and $2.2\ T_c$ are shown in fig. 4.5. The left diagrams

depict the results extracted from our Dyson-Schwinger calculation and the right ones the lattice results of ref. [39] for comparison. Also shown is the relative strength of the plasmino pole, defined as the E_2 branch in the upper part, which is given by the ratio $Z_2/(Z_1+Z_2)$. The disappearance of the scalar part of the propagator in the chiral limit, i.e. $B(i\omega_n, 0) = 0$, manifests itself in the spectral function being an even function, $\rho(-\omega, \mathbf{0}) = \rho(\omega, \mathbf{0})$, and therefore $E_1 = E_2$, $Z_1 = Z_2$. We use this as the definition of the thermal mass $m_T \equiv E_1$ and, as outlined in the context of Tab. 4.1, use this value to determine the vertex parameter d_1. It is worth noting that the qualitative behavior in fig. 4.4 does not change when increasing d_1 by one order of magnitude.

From the mass dependence of $Z_2/(Z_1+Z_2)$ in figs. 4.4 and 4.5 it is discernible that the plasmino contribution decreases with increasing quark mass. This is in accordance with the expectation that for heavy quarks the spectral function reduces to one of free quarks. Only small deviations from sum rule (4.4) are found with a mismatch of less than 4%. Furthermore we find the minimum of E_1 at non-vanishing quark mass whereas the plasmino pole increases monotonically with quark mass. The slope of E_1/T and E_2/T for fixed $m(\mu)/T$ is temperature dependent and decreases with increasing temperature. Compared to the lattice data in ref. [39], we find qualitative and quantitative similar results. Note that the highest temperature considered in our analysis is $2.2\,T_c$ whereas also $3\,T_c$ is considered in the lattice analysis. The reason is that we only have data up to $2.2\,T_c$ for the gluon propagator in our disposal. The minima in E_1/T approximately coincide with the lattice results whereas the slopes in $Z_2/(Z_1+Z_2)$ and $E_{1,2}/T$ are slightly different. However, this may be traced back to different definitions of the bare quark mass.

4.4 Momentum Dependence of the Spectral Function in the Chiral Limit

In this section, we investigate the quark propagator in the chiral limit for varying momenta. For a chiral symmetric quark propagator it is convenient to use the decomposition on energy projectors as shown in eqs. (4.11) and (4.12). In terms of the quark dressing functions we then have

$$S_\pm^P(i\omega_n, |\boldsymbol{p}|) = \frac{i\omega_n C(i\omega_n, |\boldsymbol{p}|) \pm |\boldsymbol{p}| A(i\omega_n, |\boldsymbol{p}|)}{\omega_n^2 C^2(i\omega_n, |\boldsymbol{p}|) + |\boldsymbol{p}|^2 A^2(i\omega_n, |\boldsymbol{p}|)}\,. \tag{4.26}$$

Along the same line as in the previous section we use the two-pole ansatz

$$\rho_\pm^P(\omega, |\boldsymbol{p}|) = 2\pi\big[Z_1\delta(\omega \mp E_1) + Z_2\delta(\omega \pm E_2)\big] \tag{4.27}$$

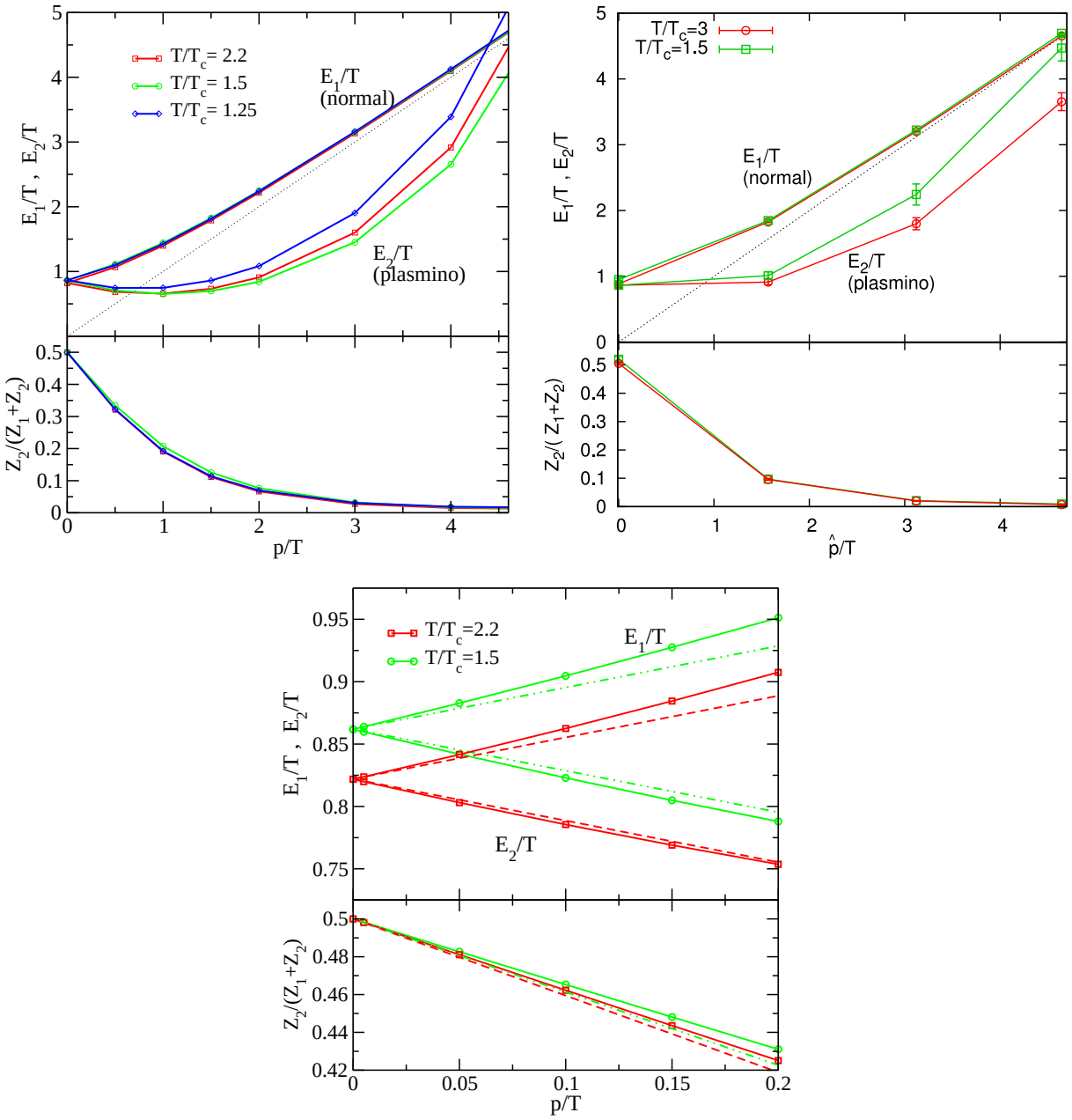

Figure 4.6: Momentum dependence of fit parameters for the two pole ansatz (4.27) at different temperatures. Upper left diagram: Dyson-Schwinger results for three different temperatures $T/T_c = 2.2$, 1.5 and 1.25. Upper right diagram: Lattice results ref. [39] for $T/T_c = 3$ and 1.5. Lower diagram: Close up of left diagram in momentum range $p/T \in [0, 0.2]$. For comparison we give the small momentum behavior of the HTL approximation in eqs.(4.28) and (4.29) as dashed lines.

and fit the parameters Z_1, Z_2 and E_1, E_2 to the data. These are then momentum dependent and we obtain the dispersion relation of quasi-particle and plasmino together with there spectral strength. For all momenta shown here ℓ_+^2 is of the same order of magnitude than the results for zero momentum.

In the upper left diagram of fig. 4.6 we show the results for the momentum dependence of the parameters E_1, E_2 and $Z_2/(Z_1+Z_2)$ for temperatures $T/T_c = 1.25$, 1.5 and 2.2. For comparison, the upper right diagram of fig. 4.6 depicts the lattice results of ref. [39]. For increasing momenta the ratio $Z_2/(Z_1+Z_2)$ decreases and tends to go to zero for high momenta. Likewise E_1 is approaching the light cone. Therefore the spectral function at high momenta reduces to the one of a single free particle. In the plasmino branch a minimum at non-vanishing momentum is clearly recognizable. This feature is known from perturbation theory and may be anticipated from the lattice results in the right diagram, albeit not observable. It is conspicuous and not obtained in one loop perturbation theory that the plasmino branch goes over into the space-like region, as seen in our analysis as well as from the lattice. However, it is known that due to Landau damping the spectral function at high temperatures contains a contribution in the space-like region which is not included in our fit ansatz, eq. (4.27). It might be that the plasmino pole by shifting into the space-like region mimics this missing contribution. This possibility is also considered in the following. An analytic continuation of the DSE to include smaller Euclidean energies might help to distinguish these different scenarios. Also note that with increasing momenta, the value of E_2 becomes less constrained by the fitting procedure, since the spectral strength Z_2 and therefore the contribution of the plasmino branch to the data decreases. We stress that we obtain very satisfactory agreement with the results of ref. [39].

In the lower diagram of fig. 4.6 we focus on the region near zero momentum. In addition to the fitted values shown as straight lines, we also present the behavior for the HTL result [75] given by

$$E_1 \simeq m_T + \frac{|\boldsymbol{p}|}{3}\,, \quad E_2 \simeq m_T - \frac{|\boldsymbol{p}|}{3}\,, \tag{4.28}$$

$$\frac{Z_2}{Z_1+Z_2} \simeq \frac{1}{2} - \frac{|\boldsymbol{p}|}{3m_T} \tag{4.29}$$

for $|\boldsymbol{p}| \ll m_T$. We observe that our results agree well with the HTL result for sufficiently small momentum, with the better agreement for the plasmino branch E_2, and then depart from it. Since the expansion is supposed to apply for small $|\boldsymbol{p}|/T$, this is expected. Comparing the two temperatures it is recognizable that the results at higher temperature agree better with the HTL result, although we are certainly not in a regime where we

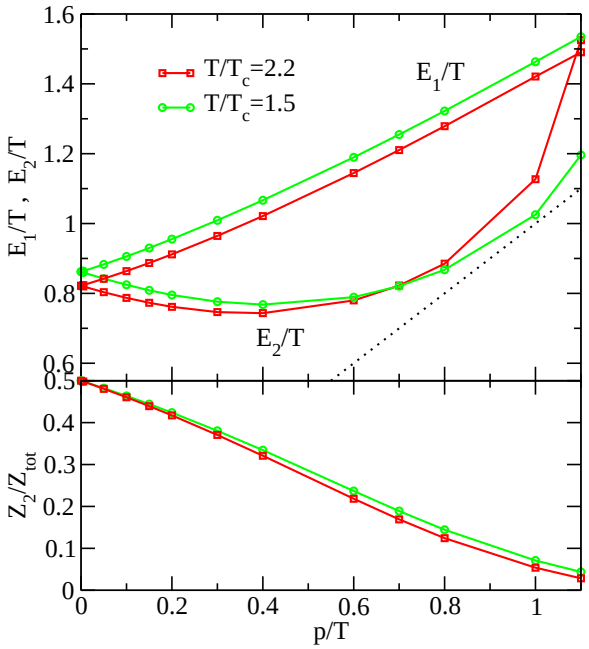

Figure 4.7: Momentum dependence of the fit parameters for the extended ansatz (4.30) for two different temperatures.

expect the HTL approximation to work.

Since the result for the plasmino branch of the two-pole ansatz indicate a possible space-like continuum contribution we extend the two-pole ansatz (4.27) by the HTL continuum contribution. The fitting function then matches exactly the spectral function in HTL approximation

$$\rho_{\pm}^{P}(\omega,\boldsymbol{p}) = 2\pi\left[Z_1\delta(\omega\mp E_1)+Z_2\delta(\omega\pm E_2)\right] + \frac{\pi}{\boldsymbol{p}}\,m_T^2\,(1\mp x)\Theta(1-x^2) \times\left[\left(\boldsymbol{p}\,(1\mp x)\pm\frac{m_T^2}{2\,\boldsymbol{p}}\left[(1\mp x)\ln\left|\frac{x+1}{x-1}\right|\pm 2\right]\right)^2+\frac{\pi^2 m_T^4}{4\boldsymbol{p}^2}(1\mp x)^2\right]^{-1} \tag{4.30}$$

where $x=\omega/\boldsymbol{p}$. The thermal masses are taken from Tab. 4.1 and $E_{1,2}$ and $Z_{1,2}$ are the fit parameters. The results are shown in fig. 4.7. We find ℓ_+^2 to be marginally smaller compared to the two-pole ansatz and we conclude from the results presented in fig. 4.6, that the plasmino branch going over into the space-like region might well be an artifact of a missing space-like spectral weight in ansatz (4.14). The upper plot of fig. 4.7 shows that the plasmino tends to the light cone for momenta $p/T\simeq 0.8$ instead of crossing it. Also the minimum of the plasmino branch has shifted to lower momenta. At high momenta the plasmino seems to deviate from the light cone again. However we note again that

due to the small spectral strength Z_2 at these momenta the value of E_2 is only poorly constrained. On the other hand the momentum dependence of E_1 is practically unaltered.

The lower plot of fig. 4.7 shows the relative strength of the plasmino $Z_2/Z_{\rm tot}$ where

$$Z_{\rm tot} = Z_1 + Z_2 + \int_{-p}^{+p} d\omega\, \rho_{\pm}^{P}(\omega, \boldsymbol{p})\,. \tag{4.31}$$

Compared to the two-pole ansatz the plasmino spectral weight decreases considerably more rapid with increasing momentum. We also find that $Z_{\rm tot}$ agrees within 3% with the expected value obtained from sum rule (4.4). Since the space-like part is sub-leading for small momenta the small momentum behavior of $E_{1,2}$ and $Z_2/(Z_1+Z_2)$ is practically unaltered by the continuum contribution.

4.5 Summary

We have analyzed the quark propagator at finite temperatures obtained within the same truncation of the quark Dyson-Schwinger equation used in the previous chapter. Our motivation was to extract characteristics of the spectral function of the propagator from the obtained data using the same method as proposed in lattice QCD calculations.

For the Matsubara propagator, i.e. in Euclidean space, our results agree qualitatively with the lattice QCD results below and above the deconfinement phase transition. General analytic properties of the quark propagator are different in the deconfining and confining phase. Our results indicate that these are determined by the non-perturbative behavior of the gluon propagator. The numerical data below the deconfinement phase transition do not allow for an interpretation in terms of a quasi-particle picture. Above the deconfinement phase transition, on the other hand, the data can be fitted by a physically motivated spectral function consisting of a quasi-particle branch and a plasmino branch with vanishing width, respectively. The obtained results for the current quark mass dependence of the thermal masses and for the dispersion relations of quasi-particle and plasmino are consistent with those from quenched lattice QCD. Including a possible space-like continuum contribution in the model spectral function shift the dispersion relation of the plasmino into the time-like region. This indicates the importance of additional continuum contributions in the spectral function.

In ref. [42] also a complementary analysis of the numerical data by means of the so-called maximum entropy method was performed. There it was found that although the method was shown to work for 'mock' data once the input was assumed to be accurate enough, the application to the numerical DSE results turned out to be more subtle. This

hints that the spectral function, at least in the employed truncation, might not be positive semi-definite. Therefore the extracted spectral functions using fit forms should be taken with a grain of salt. Nevertheless the nice agreement with lattice QCD data in Euclidean space supports our approach via Dyson-Schwinger equations in principle.

We note that shortly before completion of this work a similar study in the framework of Dyson-Schwinger equations using the Maximum Entropy Method was presented [115]. In this investigation, the authors find a mode not seen in our study. However, the difference might be explaind by the different truncation schemes. In contrast to our approach the authors utilize a rainbow ladder truncation.

Chapter 5

A Hard Thermal Loop Truncation

In chapter 3 we introduced a truncation of the quark Dyson-Schwinger equation neglecting quark loop effects in the gluon propagator meaning that only valence quarks are present. In this way we gained knowledge about the interplay between the quark propagator and the temperature dependent gluon propagator. Furthermore, this truncation allowed for an investigation of the chiral and deconfinement transition in a clean 'laboratory' avoiding the problems involved with dynamical quarks. However, in particular the contribution of the light quarks will have an important impact, as e.g. on the transition temperatures. In this chapter, we will enlarge our investigations taking into account also quark loop effects in the gluon propagator. This is an important next step towards an analysis of the QCD phase diagram. We mention at this point that we also give first insights into the influence of meson contributions, in particular of critical modes in chapter 6.

We will first consider vanishing quark chemical potential. Before we discuss the results for this case in section 5.2, we outline our truncation scheme in section 5.1. We then extend the framework and discuss results at finite chemical potential in section 5.3. As will become apparent the consideration of a finite chemical potential does not involve any further difficulties. Here, the advantages of our approach become manifest.

5.1 The Truncation Scheme

The truncation presented in section 3.2 with the corresponding $\bar{q}qg$-vertex ansatz and fit functions for the temperature dependent gluon propagator serves as our starting point. As a first approach and in oder to get an intuition for the influence of quark contributions on the gluon propagator we utilize a Hard-Thermal-Loop (HTL) like approximation. Such a proceeding was already proposed and explored in the context of a Dyson-Schwinger study

of color-superconductivity at vanishing temperature [116–118]. Our strategy will not be completely self-consistent. In particular we use 'bare' quark propagators for the thermal polarization contribution. In this way, we obtain a tractable truncation scheme. Furthermore, the assumption of 'bare' propagators may carry essential features at least above the critical temperature. The reason is that the dynamical quark degrees of freedom in which we are interested, are most important and have the largest effect in the case of light quarks with small current quark mass. Above the transition temperature there is almost no dynamical mass generation and also vector self-energies are suppressed, as the results shown in fig. 4.1 indicate. In contrast to these results we will not adjust the vertex parameters temperature dependent however, the effects of the neglected temperature dependence of the vertex and the 'bare' quark approximation are contrary and thus subtract partially. Anyway, our results a posteriori support the truncation scheme. Certainly also the self-consistent calculation incorporating the quark self-energies needs to be studied.

Figure 5.1 depicts the enhancement of the gluon propagator and the quark Dyson-Schwinger equation. The gluon propagator incorporating the HTL quark contribution $D^{\mathrm{HTL}}_{\mu\nu}(K)$ is given by

$$\left(D^{\mathrm{HTL}}_{\mu\nu}\right)^{-1}(K) = \left(D^{\mathrm{YM}}_{\mu\nu}\right)^{-1}(K) + \Pi_{\mu\nu}(K)\,, \tag{5.1}$$

where $\Pi_{\mu\nu}(K)$ denotes the polarization tensor and we have indicated that the gluon propagator on the right hand side is calculated in pure Yang-Mills theory. The general expression for the polarization tensor reads

$$\Pi_{\mu\nu}(K) = Z_{1F}\,\frac{N_f\,g^2}{2}\,T\sum_{n_q}\int\frac{d^3\,q}{(2\pi)^3}\,\mathrm{Tr}_D\Big(\gamma_\mu S(Q)\Gamma_\nu(K,L)S(Q-K)\Big)\,. \tag{5.2}$$

We may decompose the tensor in a transverse and longitudinal component

$$\Pi_{\mu\nu}(K) = P^T_{\mu\nu}(K)\,\Pi_T(K) + P^L_{\mu\nu}(K)\,\Pi_L(K)\,, \tag{5.3}$$

where $P^{T,L}_{\mu\nu}(K)$ denote the projectors given by (2.64) and (2.65). From (5.1) and (5.3) we then obtain

$$D^{\mathrm{HTL}}_{\mu\nu}(K) = P^T_{\mu\nu}(K)\,\frac{Z_T(K)}{K^2 + Z_T(K)\Pi_T(K)} + P^L_{\mu\nu}(K)\,\frac{Z_L(K)}{K^2 + Z_L(K)\Pi_L(K)} \tag{5.4}$$

where $Z_{T,L}(K)$ are the fit functions, eq. (3.7), describing the temperature dependent gluon propagator in pure Yang-Mills theory. As aforementioned, we employ the approximation of vanishing quark self-energies in the calculation of the quark loop. In this case the

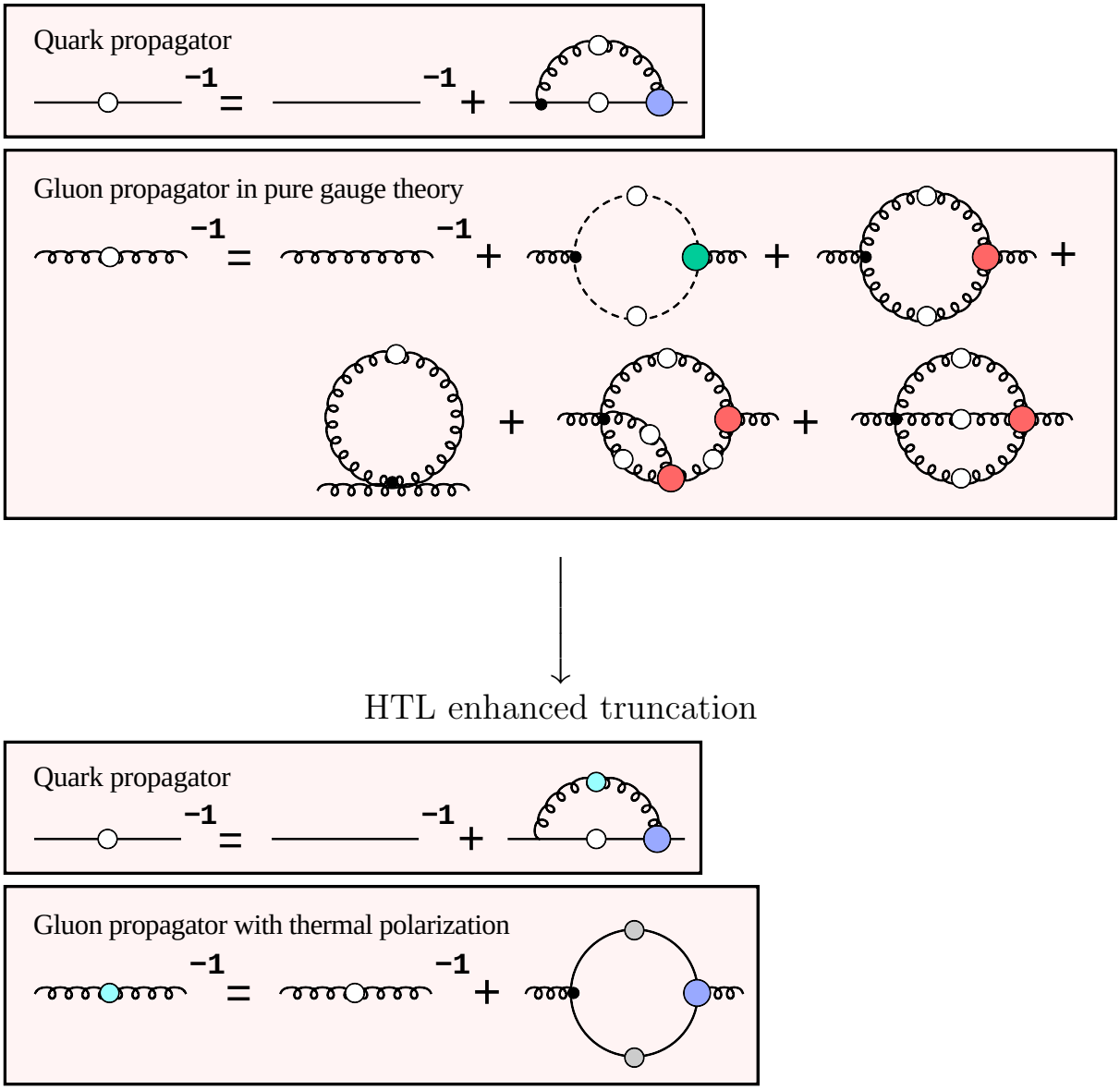

Figure 5.1: Suitable truncation scheme including quark loop effects in the gluon propagator. The gray dots for the quark loop shall indicate the HTL-approximation.

vertex ansatz in the polarization tensor, eq. (2.70), reduces to

$$\begin{aligned} \Gamma_\nu(K,L) &= \tilde{\Gamma}(K)\gamma_\nu\,, \qquad \text{with} \\ \tilde{\Gamma}(K) &= \tilde{Z}_3\left(\frac{d_1}{d_2+K^2}+\frac{K^2}{\Lambda^2+K^2}\left(\frac{\beta_0\alpha(\mu)\ln[K^2/\Lambda^2+1]}{4\pi}\right)^{2\delta}\right)\,. \end{aligned}$$

Furthermore the polarization tensor may then be expressed as

$$\Pi_{\mu\nu}(K) = \frac{Z_{1F}}{Z_2^2}\,\frac{N_f\,g^2\,\tilde{\Gamma}(K)}{2}\,T\sum_{n_q}\int\frac{d^3\,q}{(2\pi)^3}\,\mathrm{Tr}_D\Big(\gamma_\mu S_0(Q)\,\gamma_\nu\,S_0(Q-K)\Big)\,. \tag{5.5}$$

The evaluation in leading order of the sum plus integral, being proportional to T^2, is well known, see e.g. ref. [75]. Utilizing this result and defining running couplings according to eq. (2.69) by

$$\alpha_{T,L}(K) = \frac{Z_{1F}}{Z_2^2}\,\frac{g^2}{4\,\pi}\,Z_{T,L}(K)\,\tilde{\Gamma}(K) \tag{5.6}$$

we find for $(Z\,\Pi)_{T,L}(K)$ [1]:

$$Z_L(K)\Pi_L(K) \;=\; 2\,m_L^2(K)\,\frac{K^2}{\boldsymbol{k}^2}\left(1-\frac{i\,\omega_k}{2\,|\boldsymbol{k}|}\,\ln\left(\frac{i\omega_k+|\boldsymbol{k}|}{i\omega_k-|\boldsymbol{k}|}\right)\right), \tag{5.7}$$

$$Z_T(K)\Pi_T(K) \;=\; m_T^2(K)\,\frac{i\omega_k}{|\boldsymbol{k}|}\left[\frac{i\omega_k}{|\boldsymbol{k}|}+\left(1-\left(\frac{i\omega_k}{\boldsymbol{k}}\right)^2\right)\frac{1}{2}\ln\left(\frac{i\omega_k+|\boldsymbol{k}|}{i\omega_k-|\boldsymbol{k}|}\right)\right] \tag{5.8}$$

with the thermal momentum dependent masses

$$m_{T,L}^2(K) = \frac{N_f\,\pi\,T^2\,\alpha_{T,L}(K)}{3}\,. \tag{5.9}$$

With eq. (5.4) we obtain the HTL enhanced gluon propagator which now also includes the non-perturbative phenomena of Landau damping and Debye screening resulting from the quarks. The approximation of the quark loop implicitly assumes the quark masses to be negligible. Therefore, we only consider the contribution of the light up and down quarks, i.e. $N_f = 2$, on the gluon propagator. Nevertheless the mass of the valence ('test') quark may be varied.

5.2 Numerical Results at Vanishing μ_q

We investigate the chiral and the deconfinement transition in the chiral limit and for two different quark masses. The resulting temperature dependent ordinary and dual condensates are shown in fig. 5.2. The quark loop effects can be assessed by comparing with the results in fig. 3.7. We first focus on the results in the chiral limit and for the lighter quark whose mass roughly corresponds to an up quark mass. These are shown in the upper part of fig. 5.2. Except for the chiral transition in the chiral limit we find chiral and deconfinement crossovers instead of strict phase transitions. Also the transition temperatures

[1] Note that for the practical implementation the relation $\frac{i\,x}{2}\ln\left(\frac{x+i}{x-i}\right) = -x\,\arctan(1/x)$ is helpful.

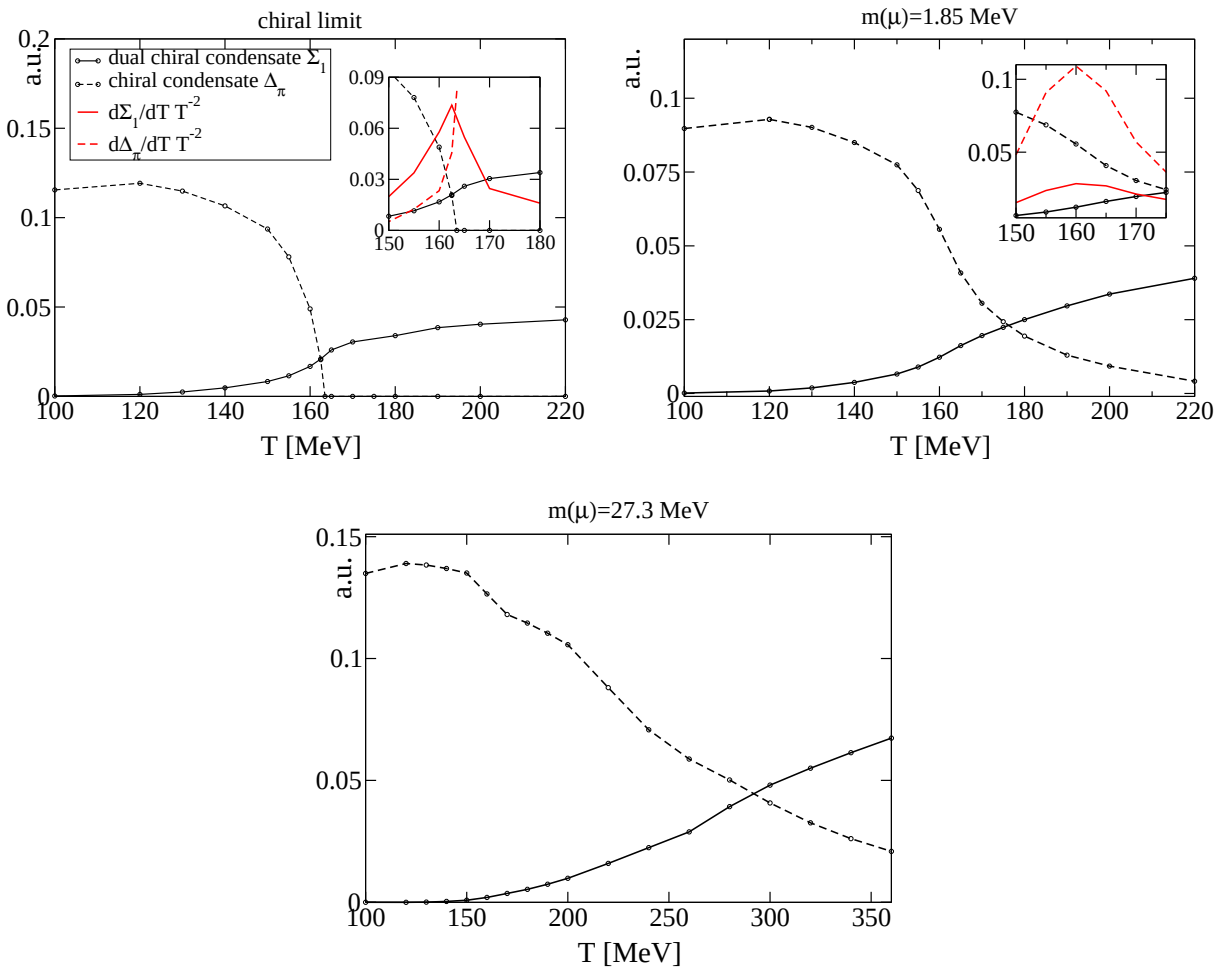

Figure 5.2: The quark condensate $\langle\bar{\psi}\psi\rangle_\pi$ and the dressed Polyakov loop Σ_1 as a function of temperature. Shown are results in arbitrary units (a.u.) for quark masses $m(\mu) = 1.85$ MeV ($\mu^2 = 10545$ GeV^2) and in the chiral limit.

shift to much lower values. This is in accordance with general expectations and also with results from lattice calculations, see [119] and references therein. A further unquenching effect can be seen from the fact that the dressed Polyakov-loop is not strictly zero below the deconfinement transition. This signals the explicit center symmetry breaking. In the chiral limit we observe a second order chiral phase transition with a vanishing chiral condensate at the critical temperature of $T_{\rm ch} \approx 163(2)$ MeV. An estimate of the transition temperatures using normalized temperature derivatives, $(d\Sigma_1/dT)\ T^{-2}$ and $(d\langle\bar{\psi}\psi\rangle_\pi/dT)\ T^{-2}$, yields $T_{\rm dec} \approx 163(1.5)$ MeV in the chiral limit and $T_{\rm ch} \simeq T_{\rm dec} \approx 160(3)$ MeV in the massive case. The errors indicated in the parenthesis give the uncertainty due to the temperature grid. Note that the temperature grid for the massive quark is more

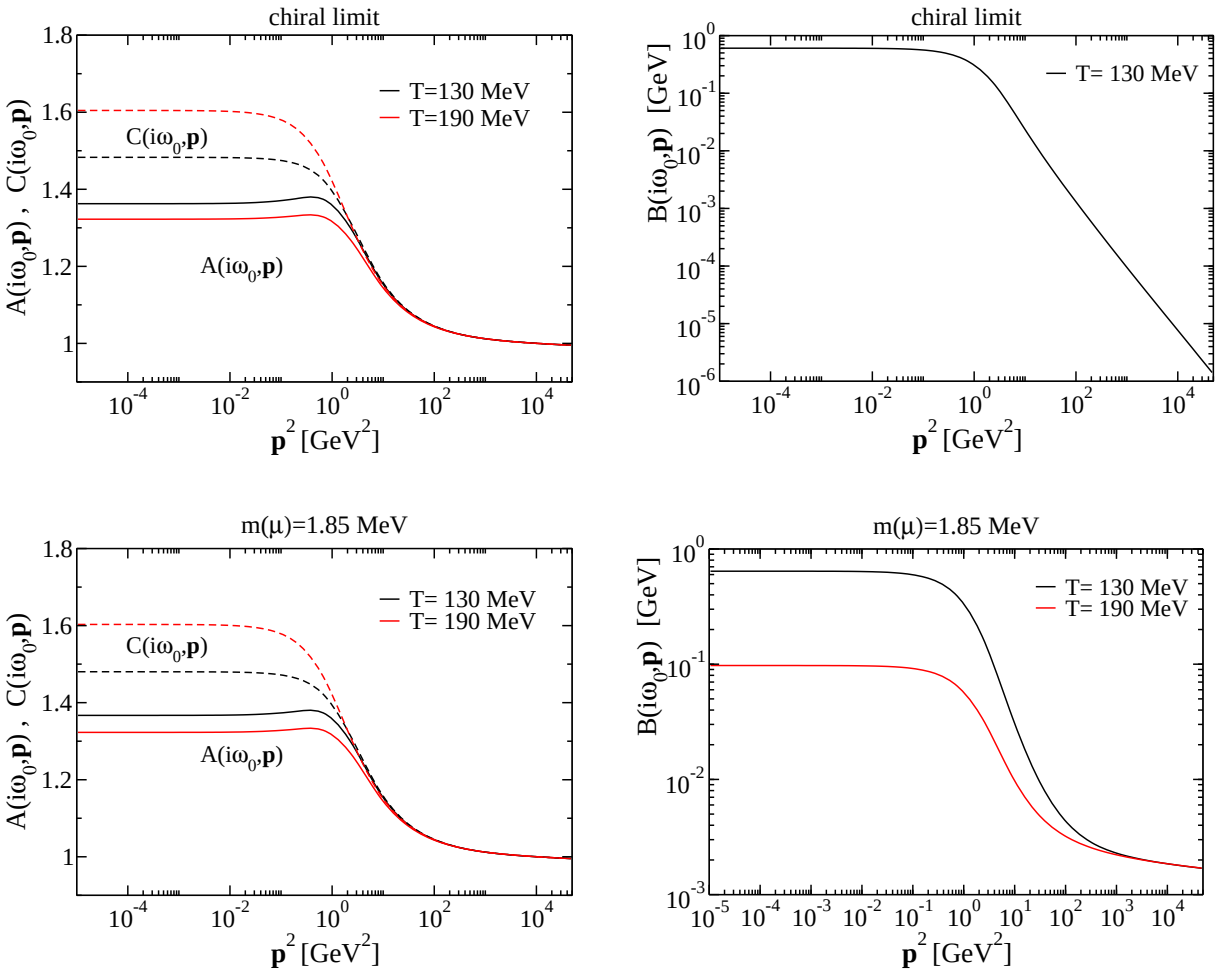

Figure 5.3: Momentum dependence of the dressing functions A, C, B below and above the critical temperature for the lowest Matsubara frequency. Shown are results in the chiral limit and in the massive case. The scalar function $B(P)$ vanishes in the chiral limit above the critical temperature.

coarse and it might be that the transition temperatures in the light massive case and the chiral limit coincide. In both cases the chiral and the deconfinement transition temperatures coincide. Both, the accordance of chiral and deconfinement crossover temperatures and the corresponding transition temperature are in agreement with lattice QCD. The transition temperature extracted from lattice QCD is given by $T_{\text{ch}} \sim 175$ MeV for $N_f = 2$ chiral flavors [120, 121]. The good agreement for this simple truncation remains to be checked in more refined calculations. Nevertheless this indicates the capabilities of the approach and is a promising starting point for further investigations.

Concerning the condensates of the heavier quark shown in the lower part of 5.2 we find

a considerable different behavior. Both transitions are heavily washed out and a narrow temperature range can hardly be determined. However, it is discernible that the reduction in the conventional condensate and the rise in the dual condensate begin at around 150 MeV thus close to the transition temperatures of the lighter quarks. Whether this general behavior is physical or due to a failure of our truncation can not yet be answered.

In fig. 5.3 we show the momentum dependence of the propagator dressing functions at lowest Matsubara frequency. The upper part shows the result in the chiral limit and the lower one for the light massive quark. The scalar function in the chiral limit above the chiral phase transition vanishes. Therefore only the result below the transition temperature can be observed on the log-log plot. The regular (chiral limit) and irregular (massive) asymptotics of the mass function are clearly discernible. We may compare these results with the ones in the quenched case, fig. 4.1. In contrast to the quenched case we observe $A(i\omega_0;\boldsymbol{p}) < C(i\omega_0;\boldsymbol{p})$ for temperatures below and above the transition and also for all momenta. This agrees with the simple interpretation of $\sqrt{A/C} = v$ as 'velocity' and is also conform with HTL results even though we are certainly not in a perturbative regime. It also suggests investigations towards spectral representations of these data. In this respect it would be interesting to compare a MEM analysis of these data with the quenched case.

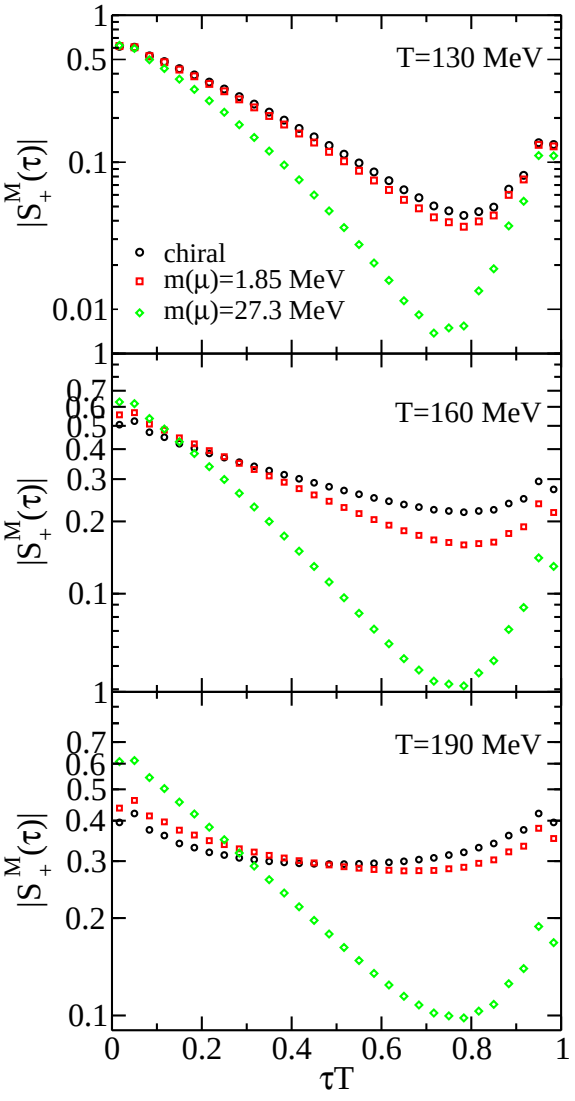

Figure 5.4: Schwinger functions at different temperatures and different masses.

In fig. 5.4 the Schwinger function, as defined in eq. (4.20), is shown. We recall that a concave curvature on a log-scale can not be reproduced by any positive definite spectral function and thus indicates the absence of the particle from the physical spectrum. At temperature $T = 130$ MeV we find concave curvature in the log-scale plot for all masses.

Comparing with fig. 5.2 we find the value of the dressed Polyakov loop to be small at this temperature, albeit not exactly vanishing. With rising temperature the concave curvature gradually disappears dependent on the quark mass. At $T = 160$ MeV the concave curvature is disappeared in the chiral limit but still present for the massive cases. It even persists for the highest mass at temperature $T = 190$ MeV and disappears in this case at $T = 220$ MeV (not shown in the figure). Note that this behavior is in one to one correspondence with the results for the dual condensate.

5.3 Numerical Results at Non-Vanishing μ_q

The framework outlined in the previous section can be extended to also include a moderate quark chemical potential. We do not consider color superconducting phases or spontaneous symmetry breaking by diquark condensation why our main theoretical framework is sufficient. A quark chemical potential μ_q is introduced in the partition function eq. (2.6) with action (2.7) by

$$\int_0^\beta d\tau d^3x\, \mathcal{L}_E \longrightarrow \int_0^\beta d\tau d^3x \left(\mathcal{L}_E + \psi^\dagger \mu_q\, \psi\right). \tag{5.10}$$

The Euclidean Lagrangian including the chemical potential can be expressed as

$$\mathcal{L}_E + \psi^\dagger \mu_q\, \psi = \bar{\psi}\big(- i(\not{D} + \gamma_4 \mu_q) + m\big)\psi + \frac{1}{2\, g_s^2} \mathrm{Tr}_c\, (F_{\mu\nu} F_{\mu\nu})\,. \tag{5.11}$$

The free quark propagator in momentum space is now given by

$$S_0^{-1}(P) = -\gamma_4(\omega_n + i\mu_q) + \gamma \cdot \boldsymbol{p} + m \tag{5.12}$$

and the full quark propagator may be parametrized as

$$S^{-1}(P) = -\gamma_4(\omega_n + i\mu_q)\, C(P) + \gamma \cdot \boldsymbol{p}\, A(P) + B(P)\,. \tag{5.13}$$

Due to the chemical potential the propagator receives an imaginary part and therefore also the self-energy contributions and the dressing functions A, C and B acquire an imaginary part.

Besides these changes only the thermal masses (5.9) become modified within the HTL truncation

$$m_{T,L}^2(K) = \frac{N_f\, \pi\, \alpha_{T,L}(K)}{3} \left(T^2 + \frac{3\, \mu_q^2}{\pi^2}\right). \tag{5.14}$$

The formal expression for the gluon propagator (5.1) with (5.7) and (5.8) thereby remain unaltered.

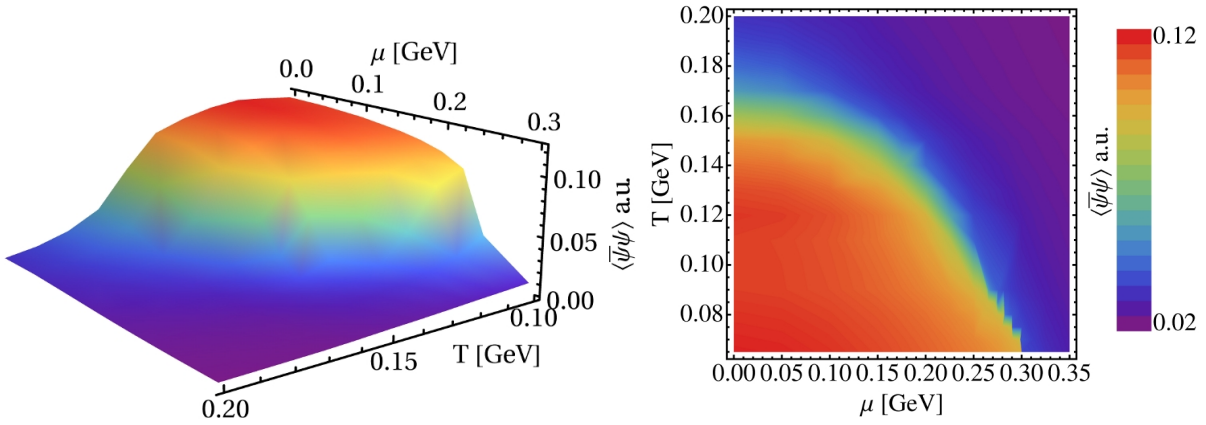

Figure 5.5: Temperature and chemical dependent chiral quark condensate $\langle\bar{\psi}\psi\rangle_\pi$ for quark mass $m(\mu) = 1.85$ MeV ($\mu^2 = 10545$ GeV^2. The case of vanishing chemical potential may be compared with fig. 5.2.

Quark condensate at non-vanishing chemical potential

We first consider the quark condensate at non-vanishing chemical potential

$$\langle\bar{\psi}\psi\rangle_\pi = Z_2 T \sum_n \int^\Lambda \frac{d^3p}{(2\pi)^3}\, \mathrm{tr}_D S(P) \tag{5.15}$$

where the quark propagator (5.13) is determined from the qDSE. An analysis of the qDSE yields

$$\mathrm{Re}A(i\omega_n, \boldsymbol{p}) = \mathrm{Re}A(-i\omega_n, \boldsymbol{p})\,, \tag{5.16}$$

$$\mathrm{Im}A(i\omega_n, \boldsymbol{p}) = -\mathrm{Im}A(-i\omega_n, \boldsymbol{p}) \tag{5.17}$$

and correspondingly for $C(i\omega_n, \boldsymbol{p})$ and $B(i\omega_n, \boldsymbol{p})$ dressing functions. The quark condensate is therefore a real function of chemical potential and temperature. Results for an up quark mass are shown in fig. 5.5. In the left diagram we show a combined plot of the temperature and chemical potential dependence. The right diagram shows the same results in a contour plot. In the contour plot we extended the temperature range down to $T = 0.065$ GeV. We obtain a narrow transition regime with a cross-over transition for temperatures $T \gtrsim 0.09$ GeV. Below this temperature the emergence of the first order transition is suggested by the contour plot, albeit the resolution needs to be improved. In fig. 5.6 we show this regime in more detail which also allows the rough location of the critical point. The critical point lies at around $T \approx 90$ MeV and $\mu_q \approx 0.26$ GeV. We only give rough values since it is expensive to locate this point exactly due to critical slowing down.

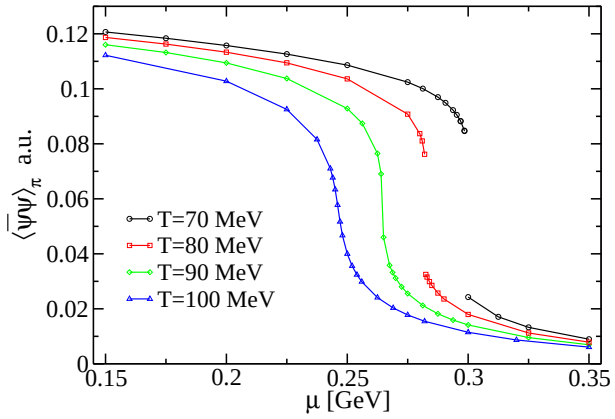

Figure 5.6: The quark condensate at the first order phase transition.

Dual condensates at non-vanishing chemical potential

In this paragraph we compare results for the dual condensates Σ_1 and Σ_{-1}. Whereas these quantities are the same in the case of vanishing chemical potential they differ at non-vanishing chemical potential. This is due to the violation of charge conjugation invariance and expresses the distinction of quarks and antiquarks. Just as the Polyakov loop can be related to the quark and antiquark free energies, Σ_1 is related to the quark free energy and Σ_{-1} to the antiquark free energy. On a technical level the difference expresses itself in the emergence of an imaginary part of the φ-dependent condensate

$$\langle\bar{\psi}\psi\rangle_\varphi = \mathrm{Re}\Big(\langle\bar{\psi}\psi\rangle_\varphi\Big) + i\mathrm{Im}\Big(\langle\bar{\psi}\psi\rangle_\varphi\Big) \tag{5.18}$$

with $\mathrm{Im}(\langle\bar{\psi}\psi\rangle_\varphi) \neq 0$ for $\varphi \neq \pi$ and $\mu_q \neq 0$. Using (5.16) and (5.17) we find $\mathrm{Re}(\langle\bar{\psi}\psi\rangle_\varphi) = \mathrm{Re}(\langle\bar{\psi}\psi\rangle_{2\pi-\varphi})$ and $\mathrm{Im}(\langle\bar{\psi}\psi\rangle_\varphi) = -\mathrm{Im}(\langle\bar{\psi}\psi\rangle_{2\pi-\varphi})$. In fig. 5.7 results are shown for the real and imaginary part of the condensate at temperature $T = 0.14$ GeV and various values of μ_q. The emergence of the imaginary part and its symmetry properties are clearly discernible. More important we find a first order transition in φ for large chemical potentials, as can be seen in the case $\mu_q = 0.3$ GeV. The location of this transition depends on temperature and chemical potential. Due to this discontinuity the calculation of the dual condensates is aggravated. In order to extract the dual condensates nevertheless we analyze each parameter set separately. We split the integration into two parts if the discontinuity occurs and in addition interpolate in φ for the numerical integration. Due to the finite number of points in φ the location of the discontinuity is tainted with uncertainty. This may cause some error on the results for the dual condensates and should be kept in mind when considering the results. The qualitative behavior is however

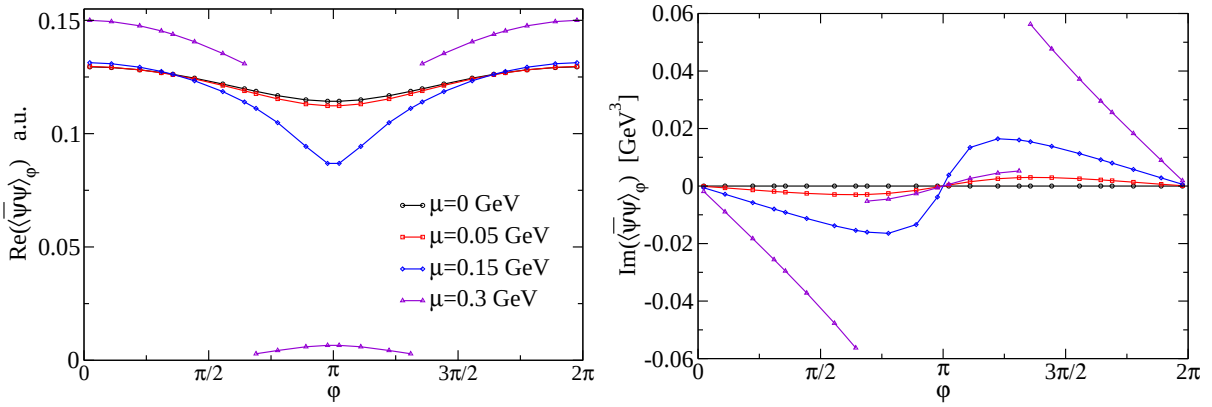

Figure 5.7: Angular dependence of the real and imaginary parts of the quark condensate at temperature $T = 0.14$ GeV.

correctly returned by our analysis.

Using that the imaginary part vanishes by symmetry when integrating over φ the dual condensates can be written as

$$\Sigma_{\pm 1} = \int_0^{2\pi} \frac{d\varphi}{2\pi} \Big\{ \mathrm{Re}(\langle \bar{\psi}\psi \rangle_\varphi) \cos(\varphi) \pm \mathrm{Im}(\langle \bar{\psi}\psi \rangle_\varphi) \sin(\varphi) \Big\} . \tag{5.19}$$

Hence, $\mathrm{Im}(\langle \bar{\psi}\psi \rangle_\varphi)$ determines the asymmetry of quarks and antiquarks. The effect is clearly discernible when comparing the contour plots in figs. 5.8 and 5.9. We find that the positive quark chemical potential stabilizes the confined phase of quarks, see fig. 5.9, and destabilizes the confined phase of antiquarks, fig. 5.8. This can be understood, considering how the chemical potential enters in our truncation. On the one hand, the chemical potential modifies the gluon propagator similar to a temperature, as can be seen from eq. (5.14). Hence, the system is driven into the deconfining phase when increasing the potential. On the other hand, the chemical potential explicitly occurs in the quark propagator (5.13). This contribution drives the system into the deconfining phase for antiquarks however has the contrary effect for quarks meaning that it stabilizes the confined phase of quarks. As shown by our results the effect in the gluon propagator will dominate at some chemical potential and we enter the deconfining regime also for quarks. This is in line with the naive picture that one has to raise more energy when putting a static quark into a thermodynamic system with background quarks already present. Our findings suggest that quarks and antiquarks possess different deconfinement crossover temperatures at finite chemical potential.

At this point two remarks seem appropriate. The first remark concerns our trunca-

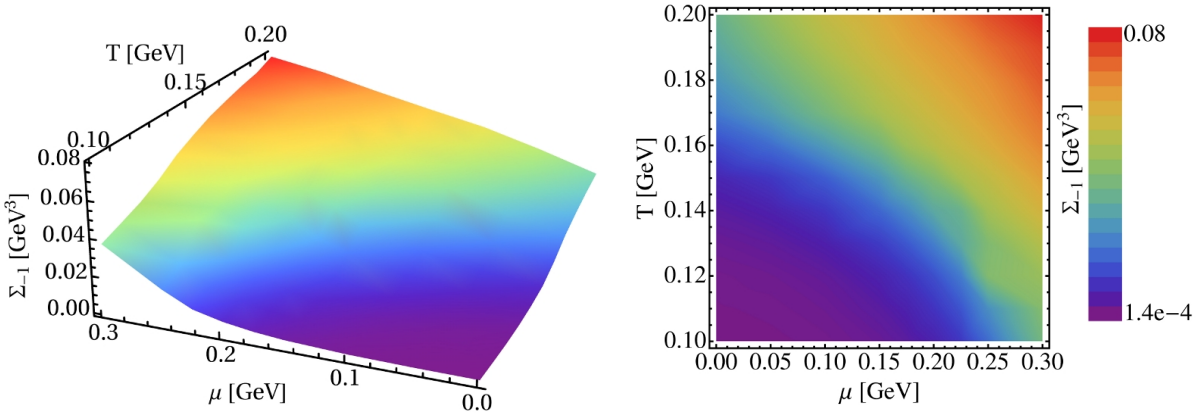

Figure 5.8: Temperature and chemical dependent dual quark condensate Σ_{-1}.

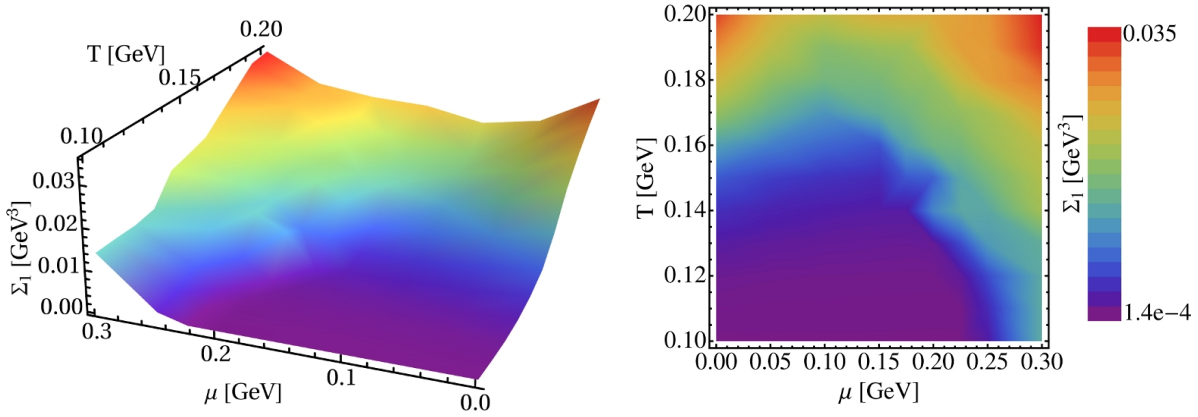

Figure 5.9: Temperature and chemical dependent dual quark condensate Σ_1.

tion scheme. We note that we only considered the leading term squared in μ_q in the gluon polarization. It certainly remains to study the effects and the interplay of subleading terms in the gluon propagator, especially regarding different impacts on quarks and antiquarks. As a second remark, we recall that center symmetry is explicitly broken. Therefore there is no strict deconfinement phase transition and due to this, also no order parameter. Though, one may generalize observables that would qualify as order parameters also to this case. These observables may than show a rapid change signaling the cross-over temperature. However, depending on the observable used somewhat different transition temperatures may be obtained. In our case this may especially concern the deconfinement transition temperatures of quarks and antiquarks.

5.4 Summary

In this chapter we introduced a truncation including unquenching effects in the gluon equation with $N_f = 2$ light quarks. We found several remarkable features. Instead of the deconfinement phase transitions in the quenched case we now find smooth crossovers. The chiral transition is a crossover transition in the massive case and a second order phase transition in the chiral limit. The crossover temperatures are significantly reduced and lie in the range of lattice findings. For heavy valence quarks there is no narrow temperature range for the crossovers discernible. Instead we obtain a steady rise in the dressed Polyakov loop and a decrease in the conventional condensate over a large temperature range. Interestingly, we found that an analysis of the Schwinger function matches with these results. At temperatures below the deconfinement crossover temperature we obtain reflection positivity violation of the spectral function by the concave curvature of the logarithmic Schwinger function. Rising the temperature, this concave curvature disappears gradually. We find a similar current quark mass dependence as for the dual condensate which means a more distinct transition for the lighter valence quarks.

Furthermore, we explored the possibility to extend the truncation scheme to finite quark chemical potential. We are able to extract the dual condensates of quarks and antiquarks. We obtain different deconfinement transitions for quarks and antiquarks and furthermore we can attribute the differences to the two input sources of the chemical potential in our truncation.

Besides the verification of our findings in more refined truncations it also remains to study the dual condensates in the range of the second order transition in detail. In this sense, the study yields a starting point for investigations including self-consistent coupling of quarks to gluons.

Chapter 6

Critical Modes and the Chiral Phase Transition

In the previous chapter we exploited the influence of quark medium effects on the gluon propagator. The framework of the HTL-like truncation indicates that this is the dominant effect with respect to the considerable different transition temperatures in pure gauge theory and QCD. In this chapter, we consider degrees of freedom particularly important for a description close to the chiral phase transition. These degrees of freedom are associated with strong long-range correlations and can be identified as Goldstone modes and the associated radial excitation. We are interested in investigating the critical chiral phase transition for two chiral flavors. In particular we study scaling laws close to the critical temperature. Before we discuss our approach in more detail a general remark concerning the applicability of Dyson-Schwinger equations may be appropriate. Although Dyson-Schwinger equations are well established they are usually not considered to study critical phenomena and it is even unclear to what extend they are suitable. An example for a calculation of the anomalous dimension in a ϕ^4-theory can be found in ref. [122]. There, the authors employ the 2PI formalism which may be interpreted as a particular truncation scheme of Dyson-Schwinger equations. A different approach employing a functional Dyson-Schwinger equation for the effective potential is described in ref. [123]. However, the results in [123] show that this framework needs to be enhanced in order to go beyond mean field. In this work we follow a different strategy by investigating the qDSE and separating quantities which obey scaling laws. We limit ourself to analytic investigations and basic ideas and leave details as well as the numerical implementation for future investigations.

6.1 Quark Propagator and Pion Effects

In ref. [124] a possibility is revealed for studying the leading meson back-reaction on the quark propagator at zero temperature. We proceed along the same lines however proposing a somewhat different truncation particularly convenient at finite temperature. In order to separate meson contributions consider the Dyson-Schwinger equation for the $q\bar{q}g$-vertex, diagrammatically shown in the upper line of fig. 6.1. Note that in contrast to the $q\bar{q}g$-vertex DSE shown in fig. 2.4, the vertices on the right hand side are connected vertices. We focus on the second diagram on the right-hand side. This contains the fully amputated connected quark-anti-quark scattering kernel $\mathcal{K}$. The scattering kernel certainly incorporates resonant meson contributions as follows from the corresponding Bethe-Salpeter equation (BSE). Among these, the important degrees of freedom close to the critical chiral phase transition, the Goldstone bosons and the so-called σ-meson, are situated. In the following we will separate these contributions and study their effect in the qDSE. The remaining diagrams in the $q\bar{q}g$-vertex DSE being also present in pure gauge theory and presumably sub-leading at the phase transition, are summarized in a simple vertex model Γ_{YM}. This procedure is depicted in fig. 6.2.

The BSE for the quark-anti-quark scattering kernel is diagrammatically shown in the second line of fig. 6.1. Formally it can be written as

$$\mathcal{K}^{rs}_{tu}(Q,K;P) = M^{rs}_{tu}(Q,K;P) + \int M^{vw}_{tu}(Q,I;P)\, S_{wa}(I_+)\, \mathcal{K}^{rs}_{ab}(I,K;P)\, S_{vb}(I_-) \qquad (6.1)$$

where $\mathcal{K}(Q,K;P)$ denotes the scattering kernel, $M(Q,I;P)$ the 2PI quark-anti-quark vertex and $S(I)$ the quark propagator. The upper and lower letters refer to appropriate Dirac-, flavor- and color indices. The momentum routing is indicated and we have $I_+ - I_- = P$ with $I_\pm = I \pm P/2$ and respectively for the other momenta. At zero temperature the pion exchange is the dominant contribution in the mid-momentum range since heavier hadrons are suppressed by factors of $\Lambda^2_{\mathrm{QCD}}/m_H$ with $H \in \{K, \rho, N, ...\}$. At finite temperature close to the critical chiral transition the infrared theory is in addition also described by the σ-meson. We assume anomalous non-conservation of $U_A(1)$ symmetry and thus a massive pseudo-scalar flavor singlet meson. The role of the $U_A(1)$ anomaly for the chiral phase transition is discussed in section 2.3. We separate the critical degrees of freedom from the kernel by writing [76]

$$\mathcal{K}^{rs}_{tu}(Q,K;P) = \bar{\Gamma}^i_M(Q,P)|_{rs}\, \frac{1}{P^2+m^2}\, \Gamma^i_M(K,P)|_{tu} + R^{rs}_{tu}(Q,K;P) \qquad (6.2)$$

where $\Gamma^i_M(K,P)$ is the Bethe-Salpeter amplitude (BSA) respectively its charge conjugate $\bar{\Gamma}^i_M(K,P)$ and R is a part regular for $P^2 \to m^2$. Concentrating on the scaling behavior

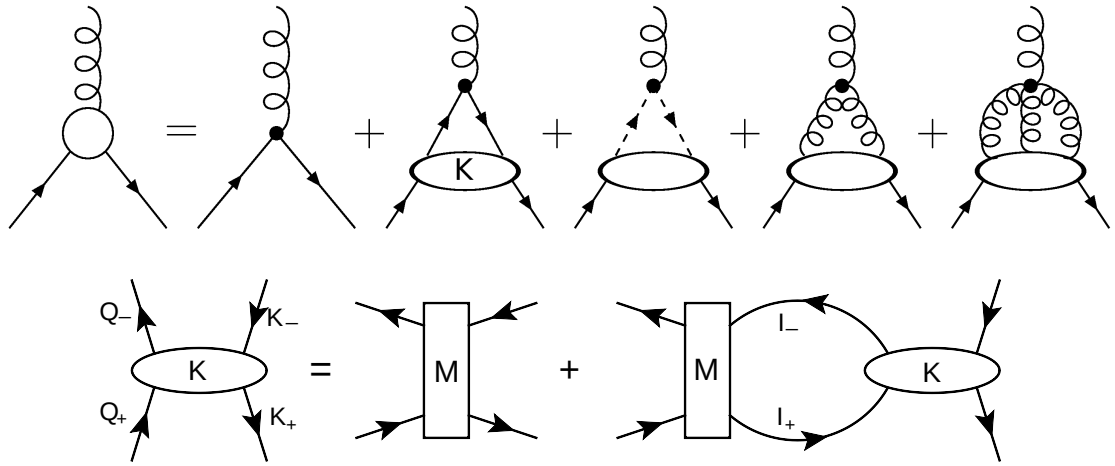

Figure 6.1: Upper line: The full untruncated Dyson-Schwinger equation for the $q\bar{q}g$-vertex, see [125]. All internal propagator are fully dressed. All signs and prefactors have been absorbed in the diagrams. The vertex on the left hand side is the 1 PI $q\bar{q}g$-vertex and the ones on the right hand side are fully amputated, connected vertices. Lower line: The inhomogeneous Bethe-Salpeter equation for the quark-antiquark scattering kernel $\mathcal{K}$. The kernel M denotes the 2PI vertex with respect the quark lines.

induced by the long-range modes we may ignore the regular part in the following. The quark-gluon vertex can then be written as a sum of the vertex model $\Gamma_{\rm YM}$ not affected by critical modes and the meson exchange contribution. This is shown in fig. 6.2 together with the resulting quark Dyson-Schwinger equation

$$S^{-1}(i\omega_{n_p}, \boldsymbol{p}) \;=\; Z_2\, S_0^{-1}(i\omega_{n_p}, \boldsymbol{p}) + \Sigma_{\rm YM}(P) + \Sigma_\pi(P) + \Sigma_\sigma(P)\,. \tag{6.3}$$

The self-energies are given by

$$\Sigma_{\rm YM}(P) \;=\; -Z_{1F}\, g_s^2\, C_f\, T \sum_{n_q} \int \frac{d^3q}{(2\pi)^3}\, \gamma_\mu\, S(Q)\, \Gamma_\nu^{YM}(K,L)\, D_{\mu\nu}(K)\,, \tag{6.4}$$

$$\Sigma_\pi(P) \;=\; -3Z_{1F}\, g_s^2\, C_f\, T \sum_{n_q} \int \frac{d^3q}{(2\pi)^3}\, \gamma_\mu\, S(Q)\, \Gamma_\nu^{\pi}(K,L)\, D_{\mu\nu}(K)\,, \tag{6.5}$$

$$\Sigma_\sigma(P) \;=\; -Z_{1F}\, g_s^2\, C_f\, T \sum_{n_q} \int \frac{d^3q}{(2\pi)^3}\, \gamma_\mu\, S(Q)\, \Gamma_\nu^{\sigma}(K,L)\, D_{\mu\nu}(K)\,. \tag{6.6}$$

We used as before $L = (Q+P)/2$ and the abbreviation $\Gamma_\nu^{(\pi,\sigma)}(K,L)$ for the triangle meson exchange. This should not be confused with the Bethe-Salpeter amplitudes $\Gamma_{\pi,\sigma}$.

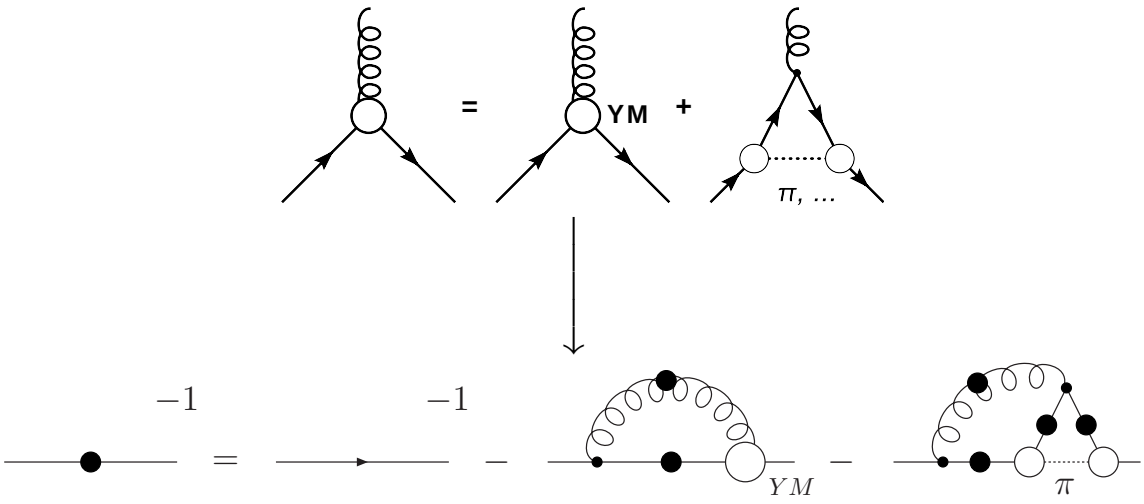

Figure 6.2: The approximation of the $q\bar{q}g$-vertex including the long-range fluctuations near the chiral phase transition (upper line). Lower line: Resulting quark Schwinger-Dyson equation.

The calculation of the quark self-energy with meson exchange is in general quiet complex. It states a two-loop diagram containing the full BSA amplitudes, $\Gamma_{\pi,\sigma}$, which can in principle be determined from the corresponding Bethe-Salpeter equation. In order to obtain a tractable truncation that in addition preserves the important features for an investigation of the chiral phase transition we employ low-energy properties of pions in the symmetry broken phase.

6.2 Goldstone Modes in QCD

Low energy properties of pions

In ref. [76] the relations between the quark propagator, the pion BSA and the pion decay constant f_π in the vacuum were clarified. The axial vector Ward-Takahashi identity (axWTI) is crucial in this respect. In the chiral limit it reads (see appendix A for details)

$$P_\mu \, \Gamma^a_{5\mu}(K,P) = S^{-1}(K_+)\, \gamma_5 \frac{\tau^a}{2} + \gamma_5 \frac{\tau^a}{2}\, S^{-1}(K_-) \tag{6.7}$$

with the isovector axial-vector vertex $\Gamma^a_{5\mu}(K,P)$ and $K_\pm = K \pm \frac{P}{2}$. In the following we consider the limit of zero bare quark mass in the spontaneous chiral symmetry broken phase and derive low-energy chiral properties at finite temperature.

As in the case of the quark-anti-quark scattering kernel one may write the isovector axial-vector vertex with a regular and an irregular part

$$\Gamma^a_{5\mu}(K,P) = \frac{\tilde{P}_\mu}{P_4^2 + v_G^2\,\vec{p}^2}\Phi^a_5(K,P) + R^a_{5\mu}(K,P)\,, \tag{6.8}$$

where the momentum $\tilde{P}_\mu = (P_4, v_G^2\vec{p})$ includes the 'velocity' v_G. Remember that $R^a_{5\mu}(K,P)$ is regular for $P_\mu \to 0$. In the vacuum Lorenz invariance implies $v_G^2 = 1$. In medium this is in general not the case. From the inhomogeneous BSE of $\Gamma^a_{5\mu}(K,P)$ evaluated at the putative poles we find that $\Phi^a_5(K,P)$ is given by the pion BSA amplitude, Γ_π, up to a residuum factor r_A:

$$\Phi^a_5(K,P^2=0) = r_A\,\Gamma^a_\pi(K,P^2=0)\,. \tag{6.9}$$

If chiral symmetry is spontaneously broken the right hand side of (6.7) is non-vanishing also in the limit $P_\mu \to 0$:

$$P_\mu\,\Gamma^a_{5\mu}(K,P)\big|_{P_\mu\to 0} = \gamma_5\tau^a B(K) \tag{6.10}$$

Hence, the isovector axial-vector vertex, respectively Φ^a_5 couples to massless modes with appropriate quantum numbers, the Goldstone bosons. In eq. (6.10) we assumed degenerate quark masses. Summarizing, we find from eqs. (6.8),(6.9) and (6.10)

$$\Phi^a_5(K,0) \;=\; \gamma_5\tau^a\,B(K)\,, \tag{6.11}$$

$$\Gamma^a_\pi(K,0) \;=\; \gamma_5\tau^a\,\frac{B(K)}{r_A}. \tag{6.12}$$

It remains to determine r_A in order to obtain the zero momentum limit of the BSA. This can be done by means of the homogeneous BSE for the isovector axial-vector vertex written in terms of the quark-antiquark scattering amplitude $\mathcal{K}$ as

$$\Gamma^a_{5\mu}(K,P)\Big|_{tu} = Z_2\,T\sum_{n_q}\int\frac{d^3q}{(2\,\pi)^3}\Big[S(Q_+)\gamma_5\,\gamma_\mu\,\frac{\tau^a}{2}\,S(Q_-)\Big]\Big|_{sr}\,\mathcal{K}^{rs}_{tu}(Q,K;P)\,. \tag{6.13}$$

Now we use again the separation in regular and irregular components, eq. (6.2), and match left- and right-hand side of (6.13) at the pole $P^2 \to 0$. This yields

$$\delta^{ab} r_A\,\tilde{P}_\mu = Z_2\,T\sum_{n_q}\int\frac{d^3q}{(2\,\pi)^3}\,\mathrm{Tr}_{D,c,f}\Big[S(Q_+)\gamma_5\gamma_\mu\frac{\tau^a}{2}S(Q_-)\bar{\Gamma}^b_\pi(Q,-P)\Big]\Big|_{P^2\to 0}\,. \tag{6.14}$$

Note that $\mathrm{Tr}_f\Big[S\gamma_5\gamma_\mu\frac{\tau^a}{2}S\,\bar{\Gamma}^b_\pi\Big] \propto \delta^{ab}$. With (6.12) we obtain

$$r_A^2\tilde{P}_\mu \;=\; 3\,Z_2\,T\sum_{n_q}\int\frac{d^3q}{(2\,\pi)^3}\,B(Q)\,\mathrm{Tr}_D\Big[S(Q_+)\gamma_5\gamma_\mu S(Q_-)\gamma_5\Big]. \tag{6.15}$$

This expression is valid in the limit $P_\mu \to 0$ only and it determines r_A^2 for $P_\mu = (P_4, 0)$ and $r_A^2\, v_G^2$ for $P_\mu = (0, \vec{p})$. It is the finite temperature generalization of the famous Pagel-Stokar formula for the pion decay constant. We denote $r_A = f_\pi^t$ as temporal decay constant and $r_A\, v_G = f_\pi^s$ as spatial decay constant.

Having discussed the pion BSA we will make a short comment on the pion propagation in the symmetry broken phase. This issue has been considered in refs. [126, 127]. The real part of the pion dispersion relation can be determined as

$$\omega_p^2 = u^2(\boldsymbol{p}^2 + m_\pi^2) \tag{6.16}$$

where u is the pion velocity and m_π is the pion screening mass. At $\boldsymbol{p}^2 = 0$ the energy of a pion $E_\pi = u m_\pi$ is called the pion pole mass. In Euclidean space, the resulting pion propagator D_π is given by

$$D_\pi = \frac{1}{\tilde{\omega}_p^2 + u^2(\boldsymbol{p}^2 + m_\pi^2)} \tag{6.17}$$

with $m_\pi = 0$ in the chiral limit. From the previous discussion it is clear that the pion velocity $u = v_G$ is determined from the pion decay constants. It is given by the ratio of f_π^s transverse to the heat bath and the longitudinal part f_π^t:

$$u = \frac{f_\pi^s}{f_\pi^t}\,. \tag{6.18}$$

Thus the pion velocity can be calculated using the relation eq. (6.15) for the pion decay constants. We note that this is in agreement with findings using other approaches [126, 127]. At temperature $T = 0$, we have $f_\pi = f_\pi^s = f_\pi^t$ and consequently $u = 1$.

Scaling analysis

Having outlined general properties of pions in the symmetry broken phase we will now perform a scaling analysis of the qDSE (6.3) for $T < T_c$ close to the critical temperature. We concentrate on a scaling of the scalar function $B(P)$ with reduced temperature. The reduced temperature is given by $t = (T_c - T)/T_c$.

Scaling laws of π-quantities close to the critical temperature can be obtained from a matching of an effective theory with QCD, as shown by Son and Stephanov in [127]. This matching reveals the following scaling laws for the decay constants f_π^t and f_π^s:

$$u \sim f_\pi^s \sim t^{\nu/2}\,, \qquad f_\pi^t \sim \text{const}\,. \tag{6.19}$$

The result is obtained using the known scaling relations for the inverse correlation length m_σ and the order parameter $\langle\bar{\psi}\psi\rangle$:

$$m_\sigma \sim t^\nu\,, \qquad \langle\bar{\psi}\psi\rangle \sim t^{\nu/2(1-\eta)}\,. \tag{6.20}$$

In $d = 3$ dimensions the values for the exponents of the $O(4)$-universality class are $\nu \approx 0.73$ and $\eta \approx 0.03$, see e.g. [128–130].

For our scaling analysis we assume a scaling law for the scalar function, $B \sim t^x$, with some unknown exponent x. The main idea is to utilize self-consistency of the Dyson-Schwinger equation. This requires left- and right-hand side of (6.3) to obey the same scaling law. For momenta large compared to the σ-mass, $m_\sigma \ll |\boldsymbol{q}|$, σ- and π-correlators will be degenerate. Since m_σ tends to zero it is appropriate to assume degeneracy of (6.5) and (6.6) for low momenta. Furthermore, for simplicity we ignore the anomalous dimension η which would be only a small correction any way. It remains to project the self-energy contributions onto the Dirac scalar

$$B(P) = \Sigma^B_{\mathrm{YM}}(P) + \Sigma^B_{\pi,\sigma}(P)\,, \tag{6.21}$$

with $\Sigma^B_{\mathrm{YM}}(P) = \mathrm{Tr}(\Sigma_{\mathrm{YM}}(P))/4$ respectively $\Sigma^B_{\pi,\sigma}(P) = \mathrm{Tr}(\Sigma_{\pi,\sigma}(P))/4$. We assume in the following that the vector dressing functions A and C do not obey a scaling law. Then the important quantities in the qDSE, obeying a scaling law, are the dressing function B and the transverse decay constant. For the first contribution, $\Sigma^B_{\mathrm{YM}} \sim B$, self-consistency is trivially fulfilled since only $B(Q)$ in the integral kernel of Σ^B_{YM} scales with reduced temperature. Therefore, both sides are proportional to t^x. Hence, as one may expect no constraint for x can be derived from this. The projection of the self-energy including the meson exchange, $\Sigma^B_{\pi,\sigma}$, yields

$$B \sim \Sigma^B_{\pi,\sigma} \sim \frac{B^3}{f_\pi^{s\,2}} + \frac{B^5}{f_\pi^{s\,2}}\,. \tag{6.22}$$

This is easily obtained from the fact that the trace over Dirac matrices is only non-vanishing for an even number of matrices. Note that the BSA is essential here. For small B, i.e. close to T_c, the cubic term is leading and the quintic term is sub-leading. With the scaling of the transverse pion decay constant given in (6.19) we find

$$B \sim t^x \sim \frac{B^3}{f_\pi^{s\,2}} \sim \frac{t^{3x}}{t^\nu} \Rightarrow x = \nu/2\,. \tag{6.23}$$

Indeed, a simple analysis shows that the solution is not only consistent with the Dyson-Schwinger equation but also with the known scaling law for the quark condensate

$$B \sim t^{\nu/2} \Rightarrow \langle\bar{\psi}\psi\rangle \sim t^{\nu/2}\,. \tag{6.24}$$

Remember that we neglected contributions stemming from the anomalous dimension. Likewise, one may study eq. (6.15) with regard to the pion decay constant. Equation

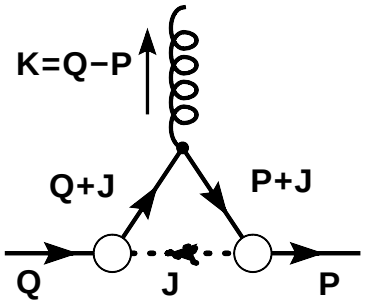

Figure 6.3: Loop diagram for the meson exchange with momenta.

(6.15) for f_π^s can approximately be expressed as (see [131] for details)

$$f_\pi^{s2} = Z_2 \frac{12}{\pi^2} T \sum_n \int \frac{d^3p}{(2\boldsymbol{p})} \frac{\boldsymbol{p}^2 A^2(P) B(P)}{(\omega_n^2 C(P)^2 + \boldsymbol{p}^2 A(P)^2 + B(P)^2)^2} \left(\frac{B(P)}{A(P)} - \frac{2}{3} \frac{\partial}{\partial \boldsymbol{p}^2} \frac{B(P)}{A(P)} \right) . \tag{6.25}$$

Inserting (6.23) for the scalar function we conclude the scaling law of f_π^{s2} as

$$B \sim t^{\nu/2} \Rightarrow f_\pi^{s2} \sim t^\nu \, . \tag{6.26}$$

Hence, we obtain a closed system in terms of scaling with t.

Although, numerical results are not yet available we outline a tractable truncation for a numerical computation. The two loop diagram is very demanding already at zero temperature and we will therefore not consider its complete self-consistent treatment. For the critical behavior close to the transition temperature it is sufficient to consider only the zeroth Matsubara mode of the meson exchange. The triangle diagram is therefore effectively given by a three dimensional loop integral. A possible momentum routing is displayed in fig. 6.3. We further use the approximation of 'bare' quark propagators in this triangle diagram. This seems justifiable since we consider the meson exchange to be a correction term and the vector dressing functions are only a slight modification assuming that they are well behaved, i.e. constant in the deep infrared. The leading contribution in the quark Dyson-Schwinger equation discussed before is also included in this 'bare' approximation. In addition, we consider the BSA in the limit of $J^2 \to 0$, see fig. 6.3, which incorporates the important long-range effects. Therefore the BSA only depends on the momenta Q respectively P and the diagram shown in fig. 6.3 is given by

$$\begin{aligned} \Gamma_\nu^{\pi,\sigma}(Q,K) &= -T \frac{B(Q)B(P)}{f_\pi^{t2}} \int \frac{d^3j}{(2\pi)^3} \, \gamma_5 \, S_0(Q+J) \, \gamma_\nu \, S_0(P+J) \gamma_5 \, D_\pi(0,\boldsymbol{j}) \\ &= T \frac{B(Q)B(P)}{f_\pi^{s2}} \int \frac{d^3j}{(2\pi)^3} \frac{\mathcal{T}^a + \mathcal{T}_i^b \, j_i + \mathcal{T}_{ij}^c \, j_i \, j_j}{\boldsymbol{j}^2 \left((\boldsymbol{j}+\boldsymbol{q})^2 + \omega_Q^2\right) \left((\boldsymbol{j}+\boldsymbol{p})^2 + \omega_P^2\right)} \end{aligned} \tag{6.27}$$

with

$$\mathcal{T}^a = \omega_Q\,\omega_P\,\gamma_4\,\gamma_\nu\,\gamma_4 - \omega_Q\gamma_4\,\gamma_\nu\,\not{p} - \not{q}\,\gamma_\nu\,\gamma_4\,\omega_P + \not{q}\,\gamma_\nu\,\not{p}\;, \tag{6.28}$$

$$\mathcal{T}^b_i = -\omega_Q\,\gamma_4\,\gamma_\nu\,\gamma_i - \gamma_i\,\gamma_\nu\,\gamma_4\,\omega_P + \gamma_i\,\gamma_\nu\,\not{p} + \not{q}\,\gamma_\nu\,\gamma_i\;, \tag{6.29}$$

$$\mathcal{T}^c_{ij} = \gamma_i\,\gamma_\nu\,\gamma_j\;. \tag{6.30}$$

This expression can be evaluated analytically. The result is somewhat lengthy. It is stated together with a sketch of the calculation in appendix D.

6.3 Summary

We outlined a possibility to study the effects of the meson back-reaction in the symmetry broken phase. This allows to account for the important degrees of freedom close to a chiral phase transition. Furthermore, an analysis showed that the essential elements to describe a second order phase transition are included and that the equations are consistent close to the critical temperature. We also suggested a truncation scheme to verify these results in a numerical calculation. Besides the numerical calculation in this framework, it also remains to investigate the contribution of the anomalous dimension.

Especially in regard to the minor insights about the applicability of Dyson-Schwinger equations to critical phenomena we believe that our investigations are interesting and promising.

Chapter 7

Conclusions and Outlook

This thesis aims to be a first step in providing Dyson-Schwinger equations as a tool for the phenomenology of strongly interacting matter at finite temperature and moderate chemical potential. The approach might provide an alternative to lattice QCD beyond model calculations. Though lattice QCD gets along without truncations and states the only ab initio approach so far, its application in the phenomenology of heavy ion physics is still affected. The implementation of quarks in lattice computations is a subtle issue and light quarks especially chiral symmetry cannot be realized, at least not in a naive form. More serious is the notorious sign problem preventing the use of Monte-Carlo methods for a direct computation at finite chemical potential. On these grounds, other reliable non-perturbative methods are highly desirable and might prove beneficial. As demonstrated in this thesis, neither the chiral limit nor the implementation of finite chemical potential cause serious problems in the continuum Dyson-Schwinger formalism.

In order to obtain sensible results, our approach should certainly be in accordance with lattice QCD in cases where lattice theory can be applied. To this end, we pursued a systematic strategy starting with a truncation scheme for the Dyson-Schwinger equation of the quark propagator neglecting dynamical quark degrees of freedom. More importantly, non-perturbative temperature dependencies of the gluon propagator come into play by using insight from lattice calculations. Also temperature effects in the quark-gluon vertex are considered within our truncation. This constitutes a considerable extension of previous studies at finite temperature in the framework of Dyson-Schwinger equations.

After having outlined the basic framework used throughout this thesis in chapter 2 we have investigated the chiral and the deconfinement transition in chapter 3. We introduced our truncation scheme corresponding to quenched SU(2) and SU(3) theory. Progress could be achieved in investigating the deconfinement transition by considering a recently pro-

posed order parameter for deconfinement, the dressed Polyakov loop. This is already of interest so far, because in general quark deconfinement is not easily accessible in functional methods. In order to extract the dressed Polyakov loop we generalized the boundary conditions for the quark propagator to $U(1)$-valued boundary conditions parametrized by an angle φ. The angular dependent quark condensate exemplified the non-trivial temperature dependence. Below T_c we found the condensate to be independent of φ to very good approximation. Consequently, the dressed Polyakov loop vanished. Accurately at the critical temperature the expected cosine-type shape developed and we observed a clean transition from the dressed Polyakov-loop. We note, that not only the behavior of the dressed Polyakov loop but also of the ordinary condensate is in agreement with previous lattice simulations. This shows a posteriori the goodness of our truncation. Furthermore, we studied the characteristic mass dependence of the condensate when approaching the chiral limit. This is the limit where the loop expansion of the dressed Polyakov loop breaks down which we found to be signaled by the derivative discontinuity in the condensate. A main insight derived from our results is the localization of the mechanism for chiral symmetry restoration and thus also for breaking in the electric gluon propagator. Its modification driven by the deconfinement transition modifies the quark-gluon interaction such that chiral symmetry gets restored. This is of certain interest even though it may be a gauge dependent statement.

An interesting future project would be to investigate the dressed Polyakov loop for fermions in the adjoint representation. In this case the chiral and the deconfinement transition differ considerable. Furthermore it remains to investigate the Landau gauge Yang-Mills system of ghost and gluon propagators at finite temperature within a functional framework. This might locate and shed light on the reasons for the dramatic change in the electric gluon propagator.

First steps beyond rainbow truncations in the determination of quark spectral functions at finite temperature from Dyson-Schwinger equations were made in chapter 4. Motivated by similar lattice QCD studies we fitted model spectral functions to our numerical data. Above T_c we found a two-pole approximation, corresponding to a normal mode and a plasmino mode, to reproduce the numerical data well. For the fitting parameters which correspond to energy and strength of the quasi-particle excitations, we extracted the mass dependence at zero momentum as well as the momentum dependence in the chiral limit. Adjusting the vertex ansatz temperature dependent in order to agree with the lattice results in the chiral limit at zero momentum, we found the extracted mass dependence to be in quantitative agreement with the lattice data. Investigating the momentum dependence in the chiral limit we found a minimum in the plasmino branch. An extension of

the model spectral function shows the possible importance of continuum contributions. Although nice agreement with lattice QCD results is obtained for the spectral functions our insights hint for its direct determination in the framework of functional methods. A central finding could however be achieved investigating analytic properties of the quark propagator using the Schwinger function. We derived a criterion for positivity violation of the spectral function and in this sense confinement. Our numerical results indeed showed positivity violation in the course of this criterion below the deconfinement phase transition temperature. Above the transition no positivity violation was found. Furthermore, we could show that the different properties below and above the transition temperature are determined by the non-perturbative behavior of the gluon propagator. From the analytic and numerical results we conclude that the Schwinger function provides an alternative deconfinement order parameter.

A canonical next step would be to determine the spectral function directly using spectral representations of the gluon and the quark-gluon vertex. By virtue of this also possible implications due to details concerning the gluon propagator and the quark-gluon vertex could be considered. It might also be illustrative to analyze the lattice results of the gluon propagator along similar lines as has been done for the results of the quark propagator in quenched approximation.

In chapter 5 we outlined an extension of the truncation scheme including effects of dynamical quark degrees of freedom. In the first part of this chapter we investigated the truncation with respect to chiral and deconfinement transition temperatures. In agreement with expectations we find dramatic changes in the transition temperatures and the nature of the transitions. This indicates the capabilities of this approach. Interestingly, an analysis of the deconfinement transition by the Schwinger function is in direct accordance with the dressed Polyakov loop. This strongly supports the approach to the deconfinement transition via the Schwinger function. Due to the promising results at vanishing chemical potential and as it is the intended aim, we also investigated the phase diagram at non-vanishing chemical potential. Concerning the quark condensate we found the expected behavior with a crossover at low chemical potential, a first order transition at high chemical potential and a second order phase transition point (critical point) connecting them. Moreover, we also determined the φ-dependent condensate. This shows a distinct behavior at non-vanishing chemical potential with a first-order transition in φ at some temperature dependent chemical potential. As a main result, we found a difference in the quark and antiquark dressed Polyakov loop. This difference is determined by the imaginary part of the condensate. For a positive quark chemical potential our results suggest that antiquarks liberate faster than quarks with increasing temperature. A detailed

investigation of the interplay of the chiral and the deconfinement transition at the second order chiral phase transition is at work.

The canonical next step is to consider a self-consistent truncation for the medium polarization of the gluon propagator. Particularly important in this respect is the possibility to study the case of $N_f = 2+1$. Concerning the analytic properties, we conclude that the good agreement of the confinement criteria extracted from the Schwinger function and from the dual condensate may hint toward a relation of both. It would certainly be interesting if such a relation could be established by analytic investigations. In this respect, it also remains to investigate the spectral and analytic properties of the quark propagator at non-vanishing chemical potential. Of interest is an analysis of the Schwinger function with respect to positivity violations and particularly with respect to differences in quarks and antiquarks. Furthermore, it would also be interesting to access the thermodynamic potential and associated quantities, as e.g. pressure and energy density.

Finally, in chapter 6 we discussed a possibility to take into account meson backreactions, which will be important for a description of the chiral phase transition. Separating quantities which obey scaling laws, we analytically derived the scaling law of the scalar dressing function B with reduced temperature. It remains to consider the closed system of equations numerically.

Acknowledgements

Without the support of many people this work would not have been possible. With pleasure I take the opportunity to thank all of them.

First of all I would like to thank my thesis advisor Christian Fischer for giving me the opportunity to work on this subject. I am very grateful to him for numerous stimulating discussions and various support and encouragement throughout this work. In particular I appreciated the possibility to participate in miscellaneous workshops and conferences making it possible to get in contact with experienced scientists.

I would like to thank Professor Jochen Wambach for being the second examiner of this work and his interest in its content.

Thanks deserves to be given to Dominik Nickel for the successful collaboration and his continuous interest in this work and helpful discussions. I thank Axel Maas for the successful collaboration and for the implementation and availability of the lattice calculations.

I appreciated the pleasant and stimulating atmosphere at the IKP Darmstadt and give thanks to the local groups, TNP, NPQCD, NPQFT, TPP and NHQ. I thank Tobias Göcke for many interesting discussions and Richard Williams for sharing his insight into Dyson-Schwinger equations. Furthermore I'd like to express my appreciation for the computer administration to Michael Wagner, Christian Kellermann, Daniel Müller, Robert Roth and Richard Williams and for all other administration matters to Mrs. Genette Kluckner.

I gratefully acknowledge elucidating explanations from Bernd-Jochen Schäfer, Jan Martin Pawlowski and Lorenz von Smekal. I thank the participants of the Theorie Palaver and my office colleagues for the good cooperation.

It is with particular pleasure that I thank my friends and family. Especially I would like to mention the support of my parents and my girlfriend Hanna.

This work has been supported by the Helmholtz Young Investigator Grant VH-NG-332.

Appendix A

Conventions

We use the conventions outlined in [75]. For completeness we review these conventions here.

Minkowski Space Conventions

We use the Metric tensor:

$$g^{\mu\nu} = \mathrm{diag}(1, -1, -1, -1)\,, \tag{A.1}$$

and Dirac matrices satisfying

$$\{\gamma^\mu, \gamma^\nu\} = 2g^{\mu\nu}\,, \qquad \gamma_5 = i\gamma^0\gamma^1\gamma^2\gamma^3\,. \tag{A.2}$$

The scalar product is given by

$$x \cdot y = x^\mu y_\mu = x^0 y^0 - \boldsymbol{x} \cdot \boldsymbol{y}\,, \tag{A.3}$$

and the divergence is

$$\partial_\mu V^\mu = \partial_0 V^0 + \nabla \boldsymbol{V}\,. \tag{A.4}$$

Fourier transform:

$$f(p) = \int d^4x\; e^{i\,p\cdot x} f(x) \quad \text{and} \quad p_\mu = i\partial_\mu\,. \tag{A.5}$$

The perturbative quark propagator reads

$$S(p) = \frac{i}{\not{p} - m} = \frac{i(\not{p} + m)}{p^2 - m^2} \tag{A.6}$$

and the gluon propagator

$$D_{\mu\nu}(p) = \frac{-i}{p^2}\left(g_{\mu\nu} - \frac{p_\mu p_\nu}{p^2}\right). \tag{A.7}$$

Furthermore we have $\not{D} = D_\mu \gamma^\mu$ with $D_\mu = \partial_\mu + A_\mu$. We included the coupling constant g_s in the gluon field.

Euclidean Space Conventions

The Euclidean space conventions are obtained from the Minkowski conventions by the following transformations:

$$t \rightarrow -i\tau \tag{A.8}$$

$$p_0 \rightarrow -ip_4 = i\omega_n \tag{A.9}$$

$$\gamma_0 \rightarrow -i\gamma_4 \tag{A.10}$$

with ω_n Matsubara frequency. The additional minus sign for the Matsubara frequeny is chosen such that $i\omega_n \rightarrow p_0$. In Euclidean space we use capital letters $P = (p_4, \boldsymbol{p}) = (-\omega_n, \boldsymbol{p})$. With this we obtain

$$\{\gamma^\mu, \gamma^\nu\} = -2\delta_{\mu\nu}\,, \tag{A.11}$$

$$f(P) = \int d^4X\; f(X)e^{-i\,P\cdot X} \quad \text{and} \quad P_\mu = -i\partial_\mu\,. \tag{A.12}$$

The propagators are given by

$$S(P) = \frac{1}{\not{P}+m} = \frac{-\not{P}+m}{P^2+m^2} = \frac{\omega_n\gamma_4 - \not{p}+m}{P^2+m^2}\,, \tag{A.13}$$

$$D_{\mu\nu}(P) = \frac{1}{P^2}\Big(\delta_{\mu\nu} - \frac{P_\mu P_\nu}{P^2}\Big)\,. \tag{A.14}$$

Note that $A_4 = iA_0$ and $A = (A_4, \boldsymbol{A})$. Hence we obtain $\not{D} = \gamma_\mu D_\mu$ with $D_\mu = \gamma_\mu - A_\mu$.

Definition of Propagators

The non-perturbative imaginary time-ordered ghost, gluon and quark propagators are defined by

$$\langle T_\tau\; c^a(X)\bar{c}^b(Y)\rangle_c = \frac{\delta^2 W}{\delta\sigma^b(Y)\,\delta\bar{\sigma}^a(X)} = D_G^{ab}(X,Y)\,, \tag{A.15}$$

$$\langle T_\tau\; A_\mu^a(X)A_\nu^b(Y)\rangle_c = \frac{\delta^2 W}{\delta J_\mu^a(X)\,\delta J_\nu^b(Y)} = D_{\mu\nu}^{ab}(X,Y)\,, \tag{A.16}$$

$$\langle T_\tau\; \psi(X)\bar{\psi}(Y)\rangle_c = \frac{\delta^2 W}{\delta\eta(Y)\,\delta\bar{\eta}(X)} = S(X,Y) \tag{A.17}$$

and we used the generating functional for connected correlators $W[\bar{\sigma},\sigma,J,\bar{\eta},\eta] = \ln Z[\bar{\sigma},\sigma,J,\bar{\eta},\eta]$, see also (2.16). We may also define 'field expectation values' $\bar{\Psi}, \Psi, \mathcal{C}, \bar{\mathcal{C}}$ and $\mathcal{A}$ according

to

$$\frac{\delta W}{\delta J^a_\mu}[\bar\sigma,\sigma,J,\bar\eta,\eta] = \mathcal{A}^a_\mu\,, \tag{A.18}$$

$$\frac{\delta W}{\delta \bar\eta}[\bar\sigma,\sigma,J,\bar\eta,\eta] = \Psi\,, \tag{A.19}$$

$$\frac{\delta W}{\delta \eta}[\bar\sigma,\sigma,J,\bar\eta,\eta] = -\bar\Psi\,, \tag{A.20}$$

$$\frac{\delta W}{\delta \bar\sigma^a}[\bar\sigma,\sigma,J,\bar\eta,\eta] = \mathcal{C}^a\,, \tag{A.21}$$

$$\frac{\delta W}{\delta \sigma^a}[\bar\sigma,\sigma,J,\bar\eta,\eta] = -\bar{\mathcal{C}}^a \tag{A.22}$$

where we kept the source terms not set to zero.

The inverse bare propagators follow from the classical action obtained from the Lagrangian (2.11). We find

$$D^{ab}_{(0)G}{}^{-1}(X,Y) = \frac{\delta^2 S_E}{\delta c^b(Y)\delta\bar c^a(X)}\bigg|_{\varphi=0} = -\delta^{ab}\partial^2\delta(X-Y) \tag{A.23}$$

$$D^{ab}_{(0)\mu\nu}{}^{-1}(X,Y) = \frac{\delta^2 S_E}{\delta A^a_\mu(X)\delta A^b_\nu(Y)}\bigg|_{\varphi=0} = \frac{\delta^{ab}}{g_s^2}\bigg(-\partial^2\delta_{\mu\nu}+\Big(1-\frac{1}{2\alpha}\Big)\partial_\mu\partial_\nu\bigg)\delta(X-Y) \tag{A.24}$$

$$S^{-1}_{(0)}(X,Y) = \frac{\delta^2 S_E}{\delta\psi(Y)\delta\bar\psi(X)}\bigg|_{\varphi=0} = (-i\partial\!\!\!/_X+m)\delta(X-Y) \tag{A.25}$$

wiht $\varphi = \{\bar\psi,\psi,A_\mu,\bar c,c\}$. The corresponding propagators in momentum space are obtained using the definition of the Fourier transformation given in eq. (A.12). We assume homogeneous phases in equilibrium meaning that the propagators only depent on $U = X - Y$.

Definition of the Quark-Gluon Vertex

The 1PI guark-gluon vertex in coordinate space is given by

$$g_s\Gamma^a_\mu(X;Y,Z) = \frac{\delta^3\Gamma[\Phi]}{\delta\mathcal{A}^a_\mu(X)\delta\Psi(Z)\delta\bar\Psi(Y)} \tag{A.26}$$

where $\Phi = \{\bar\Psi,\Psi,\mathcal{C},\bar{\mathcal{C}}\}$ and Γ is the effective action which is the generating functional of 1PI correlators, see (2.17). A connection to the connected vertex is established by

$$\frac{\delta^3 W}{\delta J^a_\mu(X)\,\delta\eta(Z)\,\delta\bar\eta(Y)} = \frac{\delta}{\delta J^a_\mu(X)}\left(\frac{\delta^2\Gamma[\Phi]}{\delta\Psi(Z)\delta\bar\Psi(Y)}\right)^{-1}. \tag{A.27}$$

From this expression we can derive

$$\begin{aligned}\frac{\delta^3 W[J]}{\delta J^a_\mu(X)\,\delta\eta(Z)\,\delta\bar\eta(Y)} &= \frac{\delta}{\delta J^a_\mu(X)}\left(\frac{\delta^2\Gamma[\Phi]}{\delta\Psi(Z)\delta\bar\Psi(Y)}\right)^{-1}\\ &= -\int_{U,T,W}\left(\frac{\delta^2\Gamma}{\delta A^b_\nu(U)\delta A^a_\mu(X)}\right)^{-1}\left(\frac{\delta^2\Gamma}{\delta\Psi(T)\delta\bar\Psi(Y)}\right)^{-1}\\ &\quad\times\left(\frac{\delta^3\Gamma}{\delta A^b_\nu(U)\delta\Psi(W)\delta\bar\Psi(T)}\right)\left(\frac{\delta^2\Gamma}{\delta\Psi(Z)\delta\bar\Psi(W)}\right)^{-1}\\ &= -\int_{U,T,W} D^{ab}_{\mu\nu}(X,U)S(Y,T)g_s\,\Gamma^b_\nu(U;T,W)\,S(W,Z)\,. \end{aligned}\tag{A.28}$$

The Fourier transformed vertex reads

$$\Gamma^a_\mu(K;Q,P) = \int d[XYZ]\,e^{-i(KZ-QY+PZ)}\Gamma^a_\mu(X;Y,Z)\tag{A.29}$$

which amounts to an incoming gluon momentuma K, one incoming quark mometum P and one outcoming quark momentum Q. Due to momentum conservation we may define a reduced vertex by

$$\Gamma^a_\mu(K;Q,P) = -i(2\pi)^4\delta(K-Q+P)\Gamma^a_\mu(Q,P)\,.\tag{A.30}$$

The bare vertex as derived from the classical action is given by

$$\Gamma^{(0)a}_\mu(Q,P) = \gamma_\mu t^a\tag{A.31}$$

with the generators of the gauge group t^a.

Axial-Vector Ward-Takahashi Identity

The Ward-Takahashi identity for general currents can be derived using an infinitesimal local transformation $\psi(x)\to(1+i\alpha(x))\psi(x)$ with $\alpha^\dagger(x)=\alpha(x)$ and applying

$$\begin{aligned} 0 &= \int[d\bar\psi\psi A]\delta(\mathcal{O}e^{-S})\,,\\ \Rightarrow\langle(\delta S)\mathcal{O}\rangle &= \langle\delta\mathcal{O}\rangle \end{aligned}\tag{A.32}$$

where $\mathcal{O}$ is some fermionic bilinear operator. In the following we employ $\mathcal{O}=\psi(y)\bar\psi(z)$ and $\alpha(x)=\varepsilon(x)\gamma_5\frac{\tau^a}{2}$. From the matter part of the Lagrangian eq. (2.11) , $\mathcal{L}^q_E=\bar\psi(-i\not{D}+m)\psi$, we obtain

$$\delta\mathcal{L}_E = \bar\psi(x)\Big(\big(\not{\partial}\alpha(x)\big)+i\,\{\alpha(x),m\}\Big)\psi(x)\,.\tag{A.33}$$

With this we get

$$
\begin{aligned}
-\partial_\mu^x \big\langle \bar\psi(x)\gamma_\mu\gamma_5\frac{\tau^a}{2}\psi(x)\,\psi(y)\bar\psi(z)\big\rangle_c &= i\delta(x-y)\gamma_5\frac{\tau^a}{2}\,\big\langle\psi(y)\bar\psi(z)\big\rangle_c \\
&+\; i\delta(x-z)\big\langle\psi(y)\bar\psi(z)\big\rangle_c\,\gamma_5\frac{\tau^a}{2} \\
&-\; i\big\langle\bar\psi(x)\big\{\gamma_5\frac{\tau^a}{2},m\big\}\psi(x)\,\psi(y)\bar\psi(z)\big\rangle_c\,.
\end{aligned}
\tag{A.34}
$$

The Fourier transformation of this expression with $m = 0$ yields the axial vector Ward-Takahashi identity as stated in eq. (6.7).

Appendix B

Derivation of the Quark DSE

As oulined in section 2.4 the Dyson-Schwinger equations for correlation functions can be derived from the assumption that the functional integral of a derivative vanishes

$$0 = \int [d\varphi] \frac{\delta}{\delta\varphi_i} \exp\left[-S[\varphi] + \int J_j \varphi_j \right] \tag{B.1}$$

$$= \left(J_i - \left. \frac{\delta S[\varphi]}{\delta \varphi_i} \right|_{\varphi \to \delta/(\delta J)} \right) \mathcal{Z}[J] \tag{B.2}$$

where the subscript collects different fields and space-time, color and/or Dirac degrees of freedom. For QCD one may define the superfield $\varphi_i = \{A^a_\mu, \bar{c}^a, c^a, \bar{\psi}, \psi\}$. In order to obtain the expression (2.39) we use the following identities

$$J_i = \frac{\delta \Gamma[\Phi]}{\delta \Phi_i} \qquad \text{and} \tag{B.3}$$

$$F\left[\frac{\delta}{\delta J_i}\right] \mathcal{Z}[J] = F\left[\frac{\delta}{\delta J_i}\right] e^{W[J]} = e^{W[J]}\, F\left[\Phi_i + \frac{\delta^2 W}{\delta J_i \delta J_j} \frac{\delta}{\delta \Phi_j}\right] , \tag{B.4}$$

where we expressed the derivative with respect to the source terms as

$$\frac{\delta}{\delta J_i} = \frac{\delta \Phi_j}{\delta J_i} \frac{\delta}{\delta \Phi_j} = \left(\frac{\delta^2 W}{\delta J_i \delta J_j} \right) \frac{\delta}{\delta \Phi_j} . \tag{B.5}$$

With this, the equation (B.2) can be brought into the useful form

$$\frac{\delta \Gamma[\Phi]}{\delta \Phi_i} = \frac{\delta S}{\delta \varphi_i} \left[\left(\frac{\delta^2 W}{\delta J_j \delta J_k} \right) \frac{\delta}{\delta \Phi_k} + \Phi_j \right] . \tag{B.6}$$

To derive the quark Dyson-Schwinger equation we differentiate with respect to $\bar{\psi}(x)$ and utilize

$$\frac{\delta}{\delta\bar{\psi}} S[\bar{\psi}, \psi, A_\mu, \bar{c}, c] = Z_2(-i\partial\!\!\!/ + Z_m m)\psi + iZ_{1F} g_s \gamma_\mu t^a A^a_\mu \psi \,, \tag{B.7}$$

$$A^a_\mu \rightarrow \mathcal{A}^a_\mu + \frac{\delta^2 W}{\delta J^a_\mu \, \delta\bar{\eta}} \frac{\delta}{\delta\Psi} + \ldots \tag{B.8}$$

$$\psi \rightarrow \Psi + \ldots \tag{B.9}$$

The dots denote terms not relevant in the derivation of the quark Dyson-Schwinger equation. These vanish due to the derivatives. Applying a further derivative with respect to $\Psi(Y)$ to (B.2) we obtain

$$\begin{aligned} \frac{\delta^2\Gamma[\Phi]}{\delta\Psi(Y)\,\delta\bar{\Psi}(X)} &= Z_2(-i\partial\!\!\!/ + Z_m m)\delta(X-Y) \\ &\quad + Z_{1F} g_s \int_Z \gamma_\mu t^a \frac{\delta^2\Gamma[\Phi]}{\delta\Psi(Y)\bar{\Psi}(Z)} \frac{\delta^3 W[J]}{\delta J^a_\mu(X)\,\delta\eta(Z)\,\delta\bar{\eta}(X)} \end{aligned} \tag{B.10}$$

where the abbreviation $\int_z = \int d\tau_z \int d^3z$ is used. Utilizing eq. (A.28) we may rewrite the connected $q\bar{q}g$-vertex appearing in the integral kernel as

$$\frac{\delta^3 W[J]}{\delta J^a_\mu(X)\,\delta\eta(Z)\,\delta\bar{\eta}(X)} = -\int_{U,T,W} D^{ab}_{\mu\nu}(X,U) S(X,T) g_s \, \Gamma^b_\nu(U;T,W)\, S(W,Z) \tag{B.11}$$

where we used the definition of the 1PI vertex (A.26). Inserting (B.11) into (B.10) yields the convential form of the quark Dyson-Schwinger equation in coordinate space

$$S^{-1}(X,Y) = Z_2\, S_0^{-1}(X,Y) - iZ_{1F}\, g_s^2 \int_{U,T} \gamma_\mu t^a S(X,T) \Gamma^b_\nu(U;T,Y) D^{ab}_{\mu\nu}(X,U) \,. \tag{B.12}$$

The Fourier transformation of this expression according to (A.12) and (A.29) yields the quark Dyson-Schwinger equation in momentum space.

Appendix C

Gluon Propagator and Quark-Gluon Vertex

We shortly summarize our input for the gluon propagator and the $q\bar{q}g$-vertex and state the fit parameters for the gluon propagator. A detailed discussion can be found in section 3.2 at eq. (3.10) and in section 4.1. For the vertex we use a temperature dependent ansatz

$$\begin{aligned}\Gamma_\nu(K,L;\mu) &= \widetilde{Z}_3\left(\delta_{4\nu}\gamma_4\frac{C(Q)+C(P)}{2}+(1-\delta_{4\nu})\gamma_\nu\frac{A(Q)+A(P)}{2}\right)\\ &\times\left(\frac{d_1}{d_2+K^2}+\frac{K^2}{\Lambda^2+K^2}\left(\frac{\beta_0\alpha(\mu)\ln[K^2/\Lambda^2+1]}{4\pi}\right)^{2\delta}\right).\end{aligned}\tag{C.1}$$

with the quark vector dressing functions A and C and the corresponding momenta $Q = L + K/2$ and $P = L - K/2$. The gluon momentum is given by K and $L = (Q+P)/2$ denotes the average momentum. The anomalous dimension δ for N_c colors and N_f flavors is given by $\delta = -9\,N_c/(44\,N_c - 8\,N_f)$. The ghost wave function renormalization constant $\tilde{Z}_3$ cancels a corresponding factor in the Dyson-Schwinger equation. We use $d_2 = 0.5$ GeV^2 for both gauge groups, $d_1 = 7.6$ GeV^2 for SU(2) and $d_1 = 4.6$ GeV^2 for SU(3) except for chapter 4. There we adjust the parameter temperature dependent as given in table 4.1.

For the dressing functions $Z_{T,L}(K)$ of the Landau gauge gluon propagator we use the following expressions fitted to lattice results

$$Z_{T,L}(K) = \frac{P^2\Lambda^2}{(K^2+\Lambda^2)^2}\left\{\left(\frac{c}{K^2+\Lambda^2 a_{T,L}(T)}\right)^{b_{T,L}(T)}+\frac{K^2}{\Lambda^2}\left(\frac{\beta_0\alpha(\mu)\ln[K^2/\Lambda^2+1]}{4\pi}\right)^{\gamma}\right\},\tag{C.2}$$

where we introduced a temperature independent scale parameter $\Lambda = 1.4$ GeV and a coefficient $c = 11.5\,\text{GeV}^2$. The anomalous dimension of the gluon is $\gamma = (-13\,N_c +$

$4\,N_f)/(22\,N_c - 4\,N_f)$. Also from perturbation theory $\beta_0 = 4/\gamma_m = (11\,N_c - 2\,N_f)/3$ and we renormalize at $\alpha(\mu) = 0.3$. The temperature dependent fit parameters $a_{T,L}$ and $b_{T,L}$ are stated in table C.1 and C.2. A comparison of our fits with the lattice data for a selection of temperatures is shown in fig. 3.1 for SU(3) and fig. C.1 for SU(2).

Table C.1: Temperature dependent fit parameters for the SU(2) gluon propagator.

	SU(2)				
T/T_c	T [MeV]	$a_L(T)$	$b_L(T)$	$a_T(T)$	$b_T(T)$
0	0	1.22	1.94	1.22	1.24
0.361	109	0.62	1.48	1.31	1.98
0.440	133	0.48	1.41	1.31	2.02
0.451	136	0.63	1.52	1.39	2.03
0.549	166	0.30	1.31	1.31	1.98
0.603	182	0.29	1.29	1.32	1.92
0.733	222	0.21	1.29	1.32	1.89
0.903	273	0.15	1.28	1.33	1.76
0.968	293	0.15	1.30	1.32	1.75
0.986	298	0.15	1.29	1.29	1.72
1.00	303	0.18	1.28	1.24	1.71
1.02	308	0.34	1.31	1.26	1.76
1.04	314	0.56	1.41	1.30	1.79
1.10	333	0.93	1.56	1.37	1.83
1.81	548	2.69	1.15	1.33	1.480
2.20	665	5.00	1.16	1.35	1.32

Table C.2: Temperature dependent fit parameters for the SU(3) gluon propagator.

	SU(3)				
T/T_c	T [MeV]	$a_L(T)$	$b_L(T)$	$a_T(T)$	$b_T(T)$
0	0	0.60	1.36	0.60	1.36
0.361	100	0.42	1.23	0.71	1.37
0.440	122	0.23	1.14	0.78	1.46
0.451	125	0.33	1.20	0.83	1.47
0.549	152	0.19	1.13	0.86	1.52
0.603	167	0.17	1.08	1.04	1.60
0.733	203	0.11	1.10	1.05	1.60
0.903	250	0.098	1.13	1.67	1.91
0.968	268	0.082	1.14	1.57	1.81
0.986	273	0.079	1.14	1.06	1.45
1.00	277	0.16	1.05	0.54	1.13
1.02	282	0.27	1.05	0.55	1.14
1.04	288	0.32	1.03	0.57	1.17
1.10	305	0.50	1.07	0.63	1.19
1.81	500	2.71	1.14	1.47	1.49
2.20	609	4.72	1.47	1.42	1.30

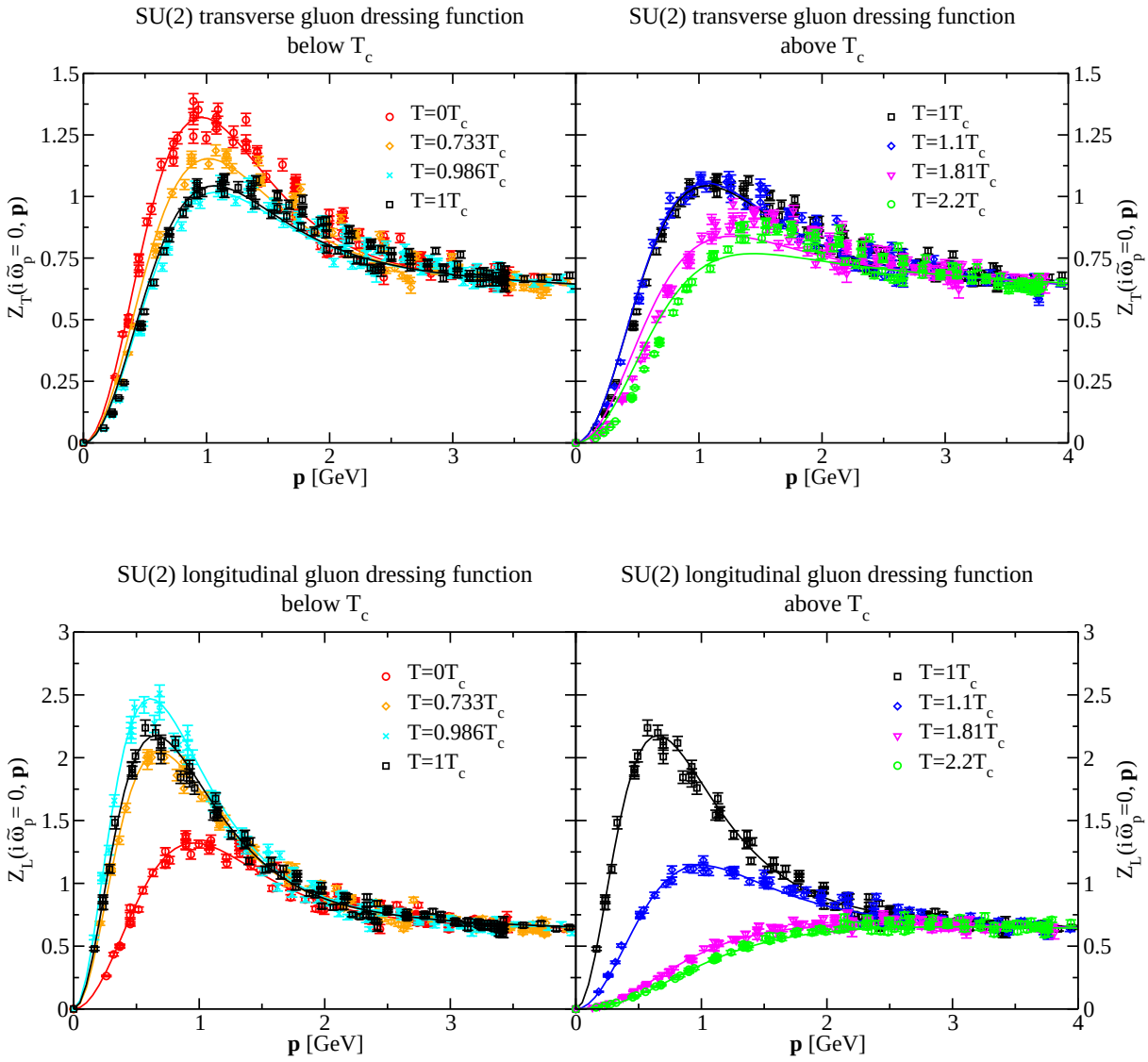

Figure C.1: Transverse (upper plot) and longitudinal (lower plot) temperature dependent gluon dressing functions for the lowest Matusbara frequency from SU(2) lattice calculations compared with our fits. The left part shows results below the critical temperature (0 T_c, 0.733 T_c, 0.986 T_c, 1 T_c) and the right part above the critical temperature (1 T_c, 1.1 T_c , 1.81 T_c , 2.2 T_c).

Appendix D

Analytic Expression of the Meson Exchange

For the meson exchange in chapter 6 we need to consider the integral

$$\Upsilon(Q,P) = \int \frac{d^3 j}{(2\pi)^3} \frac{\mathcal{T}^a + \mathcal{T}^b_i \, j_i + \mathcal{T}^c_{ij} \, j_i \, j_j}{\boldsymbol{j}^2 \left((\boldsymbol{j}+\boldsymbol{q})^2 + \omega_Q^2\right) \left((\boldsymbol{j}+\boldsymbol{p})^2 + \omega_P^2\right)} \tag{D.1}$$

with

$$\mathcal{T}^a = \omega_Q \, \omega_P \, \gamma_4 \, \gamma_\nu \, \gamma_4 - \omega_Q \gamma_4 \, \gamma_\nu \, \not{\boldsymbol{p}} - \not{\boldsymbol{q}} \, \gamma_\nu \, \gamma_4 \, \omega_P + \not{\boldsymbol{q}} \, \gamma_\nu \, \not{\boldsymbol{p}} \, , \tag{D.2}$$

$$\mathcal{T}^b_i = -\omega_Q \, \gamma_4 \, \gamma_\nu \, \gamma_i - \gamma_i \, \gamma_\nu \, \gamma_4 \, \omega_P + \gamma_i \, \gamma_\nu \, \not{\boldsymbol{p}} + \not{\boldsymbol{q}} \, \gamma_\nu \, \gamma_i \, , \tag{D.3}$$

$$\mathcal{T}^c_{ij} = \gamma_i \, \gamma_\nu \, \gamma_j \, . \tag{D.4}$$

The following integrals will be needed

$$I^{(\iota_1,\iota_2,\iota_3)} = \int \frac{d^3 p}{(2\pi)^3} \frac{1}{(\boldsymbol{j}^2)^{\iota_1} \left((\boldsymbol{j}+\boldsymbol{q})^2 + \omega_Q^2\right)^{\iota_2} \left((\boldsymbol{j}+\boldsymbol{p})^2 + \omega_P^2\right)^{\iota_3}} \, , \tag{D.5}$$

$$J_i = \int \frac{d^3 j}{(2\pi)^3} \frac{j_i}{\boldsymbol{j}^2 \left((\boldsymbol{j}+\boldsymbol{q})^2 + \omega_Q^2\right) \left((\boldsymbol{j}+\boldsymbol{p})^2 + \omega_P^2\right)} \, , \tag{D.6}$$

$$L_{ij} = \int \frac{d^3 j}{(2\pi)^3} \frac{j_i \, j_j}{\boldsymbol{j}^2 \left((\boldsymbol{j}+\boldsymbol{q})^2 + \omega_Q^2\right) \left((\boldsymbol{j}+\boldsymbol{p})^2 + \omega_K^2\right)} \, , \tag{D.7}$$

with expression (D.5) specified to $I^{(1,1,1)}$, $I^{(0,1,1)}$, $I^{(1,0,1)}$ and $I^{(1,1,0)}$. The results for $I^{(1,1,1)}$, $I^{(0,1,1)}$, $I^{(1,0,1)}$ and $I^{(1,1,0)}$ can be obtained using Feynman parametrization and standard

integration techniques. From this we find

$$I^{(1,0,1)}_{(P)} = \frac{1}{(2\pi)^3}\,\frac{2\pi^2}{\sqrt{\boldsymbol{p}^2}}\,\arctan\left(\sqrt{\frac{\boldsymbol{p}^2}{\omega_P^2}}\right) \tag{D.8}$$

$$I^{(1,1,0)}_{(Q)} = \frac{1}{(2\pi)^3}\,\frac{2\pi^2}{\sqrt{\boldsymbol{q}^2}}\,\arctan\left(\sqrt{\frac{\boldsymbol{q}^2}{\omega_Q^2}}\right) \tag{D.9}$$

and

$$I^{(0,1,1)}_{(Q,P)} = \frac{1}{(2\pi)^3}\,\frac{\pi^2}{\sqrt{(\boldsymbol{q}-\boldsymbol{p})^2}}\Bigg\{\arctan\Big(\frac{\omega_Q^2-\omega_P^2+(\boldsymbol{q}-\boldsymbol{p})^2}{2\,\sqrt{(\boldsymbol{q}-\boldsymbol{p})^2\,\omega_P^2}}\Big) + \arctan\Big(\frac{\omega_P^2-\omega_Q^2+(\boldsymbol{q}-\boldsymbol{p})^2}{2\,\sqrt{(\boldsymbol{q}-\boldsymbol{p})^2\,\omega_Q^2}}\Big)\Bigg\} \tag{D.10}$$

$$I^{(1,1,1)}_{(Q,P)} = -\frac{1}{(2\pi)^3}\,\frac{\pi^2}{(\boldsymbol{q}^2+\omega_Q^2)\,\sqrt{-c}}\Bigg\{\arctan\Big(\frac{b}{2\sqrt{-c\,a}}\Big) \tag{D.11}$$

$$- \arctan\Big(\frac{2c+b\kappa}{2\sqrt{-c\,(a\kappa^2+b\kappa+c)}}\Big)\Bigg\} \tag{D.12}$$

with

$$a = \omega_Q^2\,, \tag{D.13}$$

$$b = \omega_P^2+\omega_Q^2+(\boldsymbol{q}-\boldsymbol{p})^2-2\,\omega_Q^2\,\kappa\,, \tag{D.14}$$

$$c = \omega_P^2-\big(\omega_P^2+\omega_Q^2+(\boldsymbol{q}-\boldsymbol{p})^2\big)\,\kappa+\omega_Q^2\,\kappa^2\,, \tag{D.15}$$

$$\kappa = \frac{\boldsymbol{p}^2+\omega_P^2}{\boldsymbol{q}^2+\omega_Q^2}\,. \tag{D.16}$$

A general decomposition of the integral J_i is given by

$$J_i = q_i\,J_1 + p_i\,J_2\,. \tag{D.17}$$

From this we infer

$$q_iJ_i = \boldsymbol{q}^2J_1+(\boldsymbol{q}\cdot\boldsymbol{p})J_2\,, \tag{D.18}$$

$$p_iJ_i = (\boldsymbol{q}\cdot\boldsymbol{p})J_1+\boldsymbol{p}^2J_2 \tag{D.19}$$

and further using the explicit expression eq. (D.6) for the lefthand side

$$q_i J_i = \frac{1}{2} I^{(1,0,1)} - \frac{1}{2} I^{(0,1,1)} - \frac{\omega_Q^2 + \boldsymbol{q}^2}{2} I^{(1,1,1)} , \tag{D.20}$$

$$p_i J_i = \frac{1}{2} I^{(1,1,0)} - \frac{1}{2} I^{(0,1,1)} - \frac{\omega_P^2 + \boldsymbol{p}^2}{2} I^{(1,1,1)} . \tag{D.21}$$

Solving the system of equations (D.18) and (D.19) with eqs. (D.20) and eq. (D.21) yields

$$J_1 = \frac{1}{\beta_1\beta_2 - \alpha^2} \Big\{ I^{(1,0,1)}\,\beta_2 - I^{(1,1,0)}\,\alpha - I^{(0,1,1)}\,(\beta_2 - \alpha) - I^{(1,1,1)}\,(Q^2\,\beta_2 - K^2\,\alpha) \Big\} , \tag{D.22}$$

$$J_2 = \frac{1}{\beta_1\beta_2 - \alpha^2} \Big\{ I^{(1,1,0)}\,\beta_1 - I^{(1,0,1)}\,\alpha - I^{(0,1,1)}\,(\beta_1 - \alpha) - I^{(1,1,1)}\,(K^2\,\beta_1 - Q^2\,\alpha) \Big\} \tag{D.23}$$

where $Q^2 = \boldsymbol{q}^2 + \omega_Q^2$ and $P^2 = \boldsymbol{p}^2 + \omega_P^2$ and we used the abbreviations

$$\alpha = 2\,\boldsymbol{q}\cdot\boldsymbol{p}\,, \qquad \beta_1 = 2\,\boldsymbol{q}^2\,, \qquad \beta_2 = 2\,\boldsymbol{p}^2\,.$$

Next we consider a general decomposition of the integral L_{ij}:

$$\begin{aligned} L_{ij} = & \frac{\delta_{ij}}{3}\, I^{(\delta)} + \left(q_i\, q_j - \delta_{ij} \frac{\boldsymbol{q}^2}{3} \right) I^{(q)} + \left(p_i\, p_j - \delta_{ij} \frac{\boldsymbol{p}^2}{3} \right) I^{(p)} \\ & + \left(p_i\, q_j + q_i\, p_j - 2\,\delta_{ij} \frac{\boldsymbol{q}\cdot\boldsymbol{p}}{3} \right) I^{(qp)} . \end{aligned} \tag{D.24}$$

In order to obtain from this the result for L_{ij} we proceed a similar strategy as we did before. To this end we determine $q_j q_i L_{ij}$, $p_j p_i L_{ij}$ and $q_j p_i L_{ij}$ once from expression (D.24) and once from (D.7). The resulting system of equations is somewhat unpleasant and we therefore only state the result

$$I^{(\delta)} = I^{(0,1,1)}_{(Q,P)}, \tag{D.25}$$

$$I^{(q)} = \frac{1}{\Delta^2} \Big(2\,A\,\boldsymbol{p}^4 - 4\,C\,\boldsymbol{p}^2\,(\boldsymbol{q}\cdot\boldsymbol{p}) + B\big(\boldsymbol{p}^2\,\boldsymbol{q}^2 + (\boldsymbol{q}\cdot\boldsymbol{p})^2\big) \Big), \tag{D.26}$$

$$I^{(p)} = I^{(q)}(q \to p) = \frac{1}{\Delta^2} \Big(2\,B\,\boldsymbol{q}^4 - 4\,C\,\boldsymbol{q}^2\,(\boldsymbol{q}\cdot\boldsymbol{p}) + A\big(\boldsymbol{p}^2\,\boldsymbol{q}^2 + (\boldsymbol{q}\cdot\boldsymbol{p})^2\big) \Big), \tag{D.27}$$

$$I^{(qk)} = \frac{-1}{\Delta^2} \Big(2\,A\,\boldsymbol{p}^2\,(\boldsymbol{q}\cdot\boldsymbol{p}) - C\,(\boldsymbol{p}^2\,\boldsymbol{q}^2 + 3\,(\boldsymbol{q}\cdot\boldsymbol{p})^2) + 2\,B\,\boldsymbol{q}^2\,(\boldsymbol{q}\cdot\boldsymbol{p}) \Big) \tag{D.28}$$

where we used

$$\Delta = \left((\boldsymbol{q}\cdot\boldsymbol{p})^2 - \boldsymbol{p}^2\,\boldsymbol{q}^2\right), \tag{D.29}$$

$$A = \frac{1}{2}\,q_j\,E_{j(P)} - \frac{1}{2}\,q_j\,A_{j(Q,P)} - \frac{\boldsymbol{q}^2+\omega_Q^2}{2}\,q_j\,J_{j(Q,P)} - \frac{\boldsymbol{q}^2}{3}\,I^{(0,1,1)}, \tag{D.30}$$

$$B = \frac{1}{2}\,p_j\,E_{j(Q)} - \frac{1}{2}\,p_j\,A_{j(Q,P)} - \frac{\boldsymbol{p}^2+\omega_P^2}{2}\,p_j\,J_{j(Q,P)} - \frac{\boldsymbol{p}^2}{3}\,I^{(0,1,1)}, \tag{D.31}$$

$$C = \frac{1}{2}\,p_j\,E_{j(P)} - \frac{1}{2}\,p_j\,A_{j(Q,P)} - \frac{\boldsymbol{q}^2+\omega_Q^2}{2}\,p_j\,J_{j(Q,P)} - \frac{\boldsymbol{q}\cdot\boldsymbol{p}}{3}\,I^{(0,1,1)} \tag{D.32}$$

and in addition

$$E_{j(P)} = \int \frac{d^3j}{(2\pi)^3}\frac{j_j}{\boldsymbol{j}^2((\boldsymbol{j}+\boldsymbol{p})^2+\omega_P^2)}, \tag{D.33}$$

$$A_{j(Q,P)} = \int \frac{d^3j}{(2\pi)^3}\frac{j_j}{((\boldsymbol{j}+\boldsymbol{q})^2+\omega_Q^2)((\boldsymbol{j}+\boldsymbol{p})^2+\omega_P^2)} \tag{D.34}$$

with the corresponding expressions for $E_{j(Q)}$. Finally the analytic expressions for E_j and A_j are given by

$$E_{j(P)} = \frac{p_j\,\pi^2}{\boldsymbol{p}^2\,(2\,\pi)^3}\left\{\frac{\boldsymbol{p}^2+\omega_P^2}{\sqrt{\boldsymbol{p}^2}}\,\arctan\left(\sqrt{\frac{\boldsymbol{p}^2}{\omega_P^2}}\right) - \sqrt{\omega_P^2}\right\}, \tag{D.35}$$

$$A_{j(P,Q)} = \frac{\pi^2}{(2\pi)^3}\left\{(q_j-p_j)\,\frac{\sqrt{\omega_Q^2}-\sqrt{\omega_P^2}}{(\boldsymbol{q}-\boldsymbol{p})^2} + \left[(q_j-p_j)\,\frac{\omega_P^2-\omega_Q^2}{2\,((\boldsymbol{q}-\boldsymbol{p})^2)^{3/2}} - \frac{q_j+p_j}{2\,\sqrt{(\boldsymbol{q}-\boldsymbol{p})^2}}\right]\times \right.$$
$$\left.\left(\arctan\left(\frac{(\boldsymbol{q}-\boldsymbol{p})^2+\omega_P^2-\omega_Q^2}{2\sqrt{(\boldsymbol{q}-\boldsymbol{p})^2\,\omega_Q^2}}\right) + \arctan\left(\frac{(\boldsymbol{q}-\boldsymbol{p})^2-\omega_P^2+\omega_Q^2}{2\sqrt{(\boldsymbol{q}-\boldsymbol{p})^2\,\omega_P^2}}\right)\right)\right\}. \tag{D.36}$$

$$\tag{D.37}$$

Collecting everything together we obtain the final result:

$$\Upsilon(Q,P) = \mathcal{T}^a\,I^{(1,1,1)}_{(Q,P)} + \mathcal{T}^b_i\,J_{i(Q,P)} + \mathcal{T}^c_{ij}\,L_{ij(Q,P)} \tag{D.38}$$

$$= \left[\mathcal{T}^a\,I^{(1,1,1)}_{(Q,P)} + \mathcal{T}^b_i\left(q_i\,J_{1(Q,P)} + p_i\,J_{2(Q,P)}\right) + \mathcal{T}^c_{ij}\left(\frac{\delta_{ij}}{3}\,I^{(\delta)} + \left(q_i\,q_j - \delta_{ij}\frac{q^2}{3}\right)I^{(q)}\right.\right.$$
$$\left.\left. + \left(p_i\,p_j - \delta_{ij}\frac{\boldsymbol{p}^2}{3}\right)I^{(p)} + \left(p_i\,q_j + q_i\,p_j - 2\,\delta_{ij}\frac{\boldsymbol{q}\cdot\boldsymbol{p}}{3}\right)I^{(qp)}\right)\right]. \tag{D.39}$$

This expression is inserted in the qDSE and the corresponding projection on the scalar function yields the self-energy Σ_B in (6.21).

Appendix E

Numerical Implementation

For the numerical computation of the quark propagator we project the Dyson-Schwinger equation on the dressing functions A, C and B. The corresponding projection is given by

$$A(P) = 1/(4\boldsymbol{p}^2)\,\mathrm{Tr}_D(\gamma\cdot\boldsymbol{p}\,S^{-1}(P))\,, \tag{E.1}$$

$$B(P) = 1/4\,\mathrm{Tr}_D(S^{-1}(P))\,, \tag{E.2}$$

$$C(P) = 1/(4\omega_n)\,\mathrm{Tr}_D(\gamma_4 S^{-1}(P))\,. \tag{E.3}$$

The quark Dyson-Schwinger equation can then formaly be written as

$$A(P) = Z_2 + \Sigma_A(P) \tag{E.4}$$

$$B(P) = Z_2\,Z_m m(\mu) + \Sigma_B(P) \tag{E.5}$$

$$C(P) = Z_2 + \Sigma_C(P) \tag{E.6}$$

where $\Sigma_{A,B,C}(P)$ denote the self-energies. These are given by a loop expression with a sum over Matsubara frequencies, $T\sum_{n_q}$, and an integration over three momentum, $\int\frac{d^3q}{(2\pi)^3}$. A self-consistent solution is found using the conventional fixed point iteration method. The loop integral and Matsubara sum is regularized using a sharp cutoff Λ such that the integration and summation extends to momenta and frequencies with $\omega_q^2+q^2\leq\Lambda^2$. This is requisite to restore O(4) invariance at perturbative momenta as well as in the limit of zero temperature. We explicitly verified that the resulting renormalized quark propagator is independent of the size of the ultraviolet cutoff by increasing/decreasing the cutoff by an order of magnitude. The summation over Matsubara frequencies is explicitly performed only for a few frequencies, typically $|n|\leq 30$, and the remaining sum is approximated by an integral that can be done with standard Gauss-Legendre integration

$$T\sum_{|\omega_n|\leq\Lambda} f(\omega_n^2) \sim 2T\sum_{n=0}^{N} f(\omega_n^2) + \frac{1}{\pi}\int_{\pi T 2N}^{\Lambda} d\omega_n\, f(\omega_n^2)\,. \tag{E.7}$$

Here we assumed $f(\omega_n) = f(-\omega_n) = f(\omega_{-(n+1)})$ which is the case for the dressing functions A, C, B and the corresponding self-energies when considering usual antiperiodic boundary conditions in temporal direction. Obviously this symmetry reduces the number of calculations for the Matsubara frequencies by one half. The approximation of the sum by an integral turns out to be a very well performing technique as we checked by explicitly summing all frequencies up to the cutoff for some tests. When considering generalized $U(1)$-valued boundary conditions in temporal direction the symmetry $\omega_n \to \omega_{-(n+1)}$ is no longer present. This reduces the numerical performance. The Matsubara summation is then implemented by

$$T \sum_{|\omega_n^\varphi| \leq \Lambda} f(\omega_n^\varphi) \sim T \sum_{\omega_n^\varphi = -N}^{N-1} f(\omega_n^\varphi) + \frac{1}{2\pi} \int_{\pi T(2N + \frac{\varphi - \pi}{\pi})}^{\Lambda} d\omega_n^\varphi \, f(\omega_n^\varphi) - \frac{1}{2\pi} \int_{\pi T(-2N + \frac{\varphi - \pi}{\pi})}^{-\Lambda} d\omega_n^\varphi \, f(\omega_n^\varphi) \tag{E.8}$$

where $\omega_n^\varphi = \pi T(2n + \frac{\varphi}{\pi})$ denote the Matsubara frequencies corresponding to the $U(1)$-boundary conditions. As can be easily checked for $\varphi = \pi$ we obtain antiperiodic boundary conditions and eq. (E.7).

In the three momentum integral the integrands are independent of one angle ϕ and we can perform this integration

$$\int^{\Lambda} \frac{d^3q}{(2\pi)^3} = \frac{1}{(2\pi)^2} \int^{\Lambda} dq \, q^2 \int_0^{\pi} d\vartheta \, \sin\vartheta \, . \tag{E.9}$$

In the framework of our trunctation the ϑ-integration is independent of the dressing functions and can be numerically determined once in advance. Upon integrating over the radial momentum we defined an outer momentum grid for the dressing functions, typically about 26 momenta equidistantly distributed on a logarithmic scale and an inner momentum grid for the loop momentum. The inner momentum grid corresponds to the integration momentum and we use a Gauss-Legendre integration on a logarithmic scale between the outer momentas. In order to obtain the dressing functions for arbitrary momenta we employed a cubic spline interpolation. In the chiral limit we interpolated on a log-scale for the scalar dressing function B. A check of the numerically accuracy revealed that the numerical error on our data estimated with eq. (4.19) is given by

$$\chi = \sum_{n}^{N_\omega} |\Delta S_+^M(i\omega_n)| < 10^{-10} \text{ GeV}^{-2} \, , \tag{E.10}$$

where $\Delta S_+^M(i\omega_n)$ denotes the difference between a calculation with very high accuracy and one with low accuracy. For the high accuray we peformed all Matsubara frequencies explicitly and used 36 grid points for the outer momenta and five momenta between each

two outer momenta. The calculation with less accuracy is performed with 40 explicitly summed Matsubara frequencies, 40 grid points for the remaining Matsubara integration, 26 outer momentum grid points and five momenta between each two outer momenta.

In determining the parameters of the spectral function in chapter 4 we used the GNU-Scientific-Library for nonlinear least squares fitting [132]. This relies on the Levenberg-Marquardt algorithm.

Bibliography

[1] D. J. Gross and F. Wilczek, "Ultraviolet behavior of non-abelian gauge theories," Phys. Rev. Lett. **30** (1973) 1343.

[2] H. D. Politzer, "Reliable perturbative results for strong interactions?," Phys. Rev. Lett. **30** (1973) 1346.

[3] G. 't Hooft, Unpublished talk at the Marseille conference on renormalization of Yang-Mills fields and applications to particle physics, (June 1972).

[4] GSI Darmstadt, "The QCD phase diagram."

[5] P. de Forcrand and O. Philipsen, "The QCD phase diagram for small densities from imaginary chemical potential," Nucl. Phys. B **642** (2002) 290 [arXiv:hep-lat/0205016].

[6] M. D'Elia and M. P. Lombardo, "Finite density QCD via imaginary chemical potential," Phys. Rev. D **67** (2003) 014505 [arXiv:hep-lat/0209146].

[7] Z. Fodor and S. D. Katz, "Lattice determination of the critical point of QCD at finite T and mu," JHEP **0203** (2002) 014 [arXiv:hep-lat/0106002].

[8] C. R. Allton *et al.*, "The QCD thermal phase transition in the presence of a small chemical potential," Phys. Rev. D **66** (2002) 074507 [arXiv:hep-lat/0204010].

[9] R. V. Gavai and S. Gupta, "Pressure and non-linear susceptibilities in QCD at finite chemical potentials," Phys. Rev. D **68** (2003) 034506 [arXiv:hep-lat/0303013].

[10] F. Karsch, B. J. Schaefer, M. Wagner and J. Wambach, "Towards finite density QCD with Taylor expansions," arXiv:1009.5211 [hep-ph].

[11] C. Schmidt, "Lattice QCD at finite density," PoS **LAT2006** (2006) 021 [arXiv:hep-lat/0610116].

[12] O. Philipsen, "The QCD phase diagram at zero and small baryon density," PoS **LAT2005** (2006) 016 [arXiv:hep-lat/0510077].

[13] C. Bernard *et al.* [MILC Collaboration], "QCD thermodynamics with three flavors of improved staggered quarks," Phys. Rev. D **71** (2005) 034504 [arXiv:hep-lat/0405029].

[14] Y. Aoki, G. Endrodi, Z. Fodor, S. D. Katz and K. K. Szabo, "The order of the quantum chromodynamics transition predicted by the standard model of particle physics," Nature **443** (2006) 675 [arXiv:hep-lat/0611014].

[15] F. Karsch, "Recent lattice results on finite temerature and density QCD, part II," PoS **LAT2007** (2007) 015 [arXiv:0711.0661 [hep-lat]].

[16] F. Karsch [RBC Collaboration and HotQCD Collaboration], "Equation of state and more from lattice regularized QCD," J. Phys. G **35** (2008) 104096 [arXiv:0804.4148 [hep-lat]].

[17] S. Borsanyi, Z. Fodor, C. Hoelbling, S. D. Katz, S. Krieg, C. Ratti and K. K. Szabo [Wuppertal-Budapest Collaboration], "Is there still any Tc mystery in lattice QCD? Results with physical masses in the continuum limit III," JHEP **1009** (2010) 073 [arXiv:1005.3508 [hep-lat]].

[18] W. Soeldner, Talk presented at the XXVIII International Symposium on Lattice Field Theory.

[19] M. A. Stephanov, "QCD phase diagram and the critical point," Prog. Theor. Phys. Suppl. **153** (2004) 139 [Int. J. Mod. Phys. A **20** (2005) 4387] [arXiv:hep-ph/0402115].

[20] C. R. Allton *et al.*, "Thermodynamics of two flavor QCD to sixth order in quark chemical potential," Phys. Rev. D **71**, 054508 (2005) [arXiv:hep-lat/0501030].

[21] P. de Forcrand and O. Philipsen, "The chiral critical line of N_f=2+1 QCD at zero and non-zero baryon density," JHEP **0701** (2007) 077 [arXiv:hep-lat/0607017].

[22] Z. Fodor and S. D. Katz, "Critical point of QCD at finite T and mu, lattice results for physical quark masses," JHEP **0404**, 050 (2004) [arXiv:hep-lat/0402006].

[23] B. B. Back *et al.*, "The PHOBOS perspective on discoveries at RHIC," Nucl. Phys. A **757** (2005) 28 [arXiv:nucl-ex/0410022].

[24] I. Arsene *et al.* [BRAHMS Collaboration], "Quark Gluon Plasma an Color Glass Condensate at RHIC? The perspective from the BRAHMS experiment," Nucl. Phys. A **757** (2005) 1 [arXiv:nucl-ex/0410020].

[25] K. Adcox *et al.* [PHENIX Collaboration], "Formation of dense partonic matter in relativistic nucleus nucleus collisions at RHIC: Experimental evaluation by the PHENIX collaboration," Nucl. Phys. A **757** (2005) 184 [arXiv:nucl-ex/0410003].

[26] J. Adams *et al.* [STAR Collaboration], "Experimental and theoretical challenges in the search for the quark gluon plasma: The STAR collaboration's critical assessment of the evidence from RHIC collisions," Nucl. Phys. A **757** (2005) 102 [arXiv:nucl-ex/0501009].

[27] K. Huebner, F. Karsch and C. Pica, "Correlation functions of the energy-momentum tensor in SU(2) gauge theory at finite temperature," Phys. Rev. D **78** (2008) 094501 [arXiv:0808.1127 [hep-lat]].

[28] D. Nickel, "How many phases meet at the chiral critical point?," Phys. Rev. Lett. **103** (2009) 072301 [arXiv:0902.1778 [hep-ph]].

[29] L. McLerran and R. D. Pisarski, "Phases of Cold, Dense Quarks at Large N_c," Nucl. Phys. A **796** (2007) 83 [arXiv:0706.2191 [hep-ph]].

[30] T. Kojo, Y. Hidaka, L. McLerran and R. D. Pisarski, "Quarkyonic Chiral Spirals," Nucl. Phys. A **843** (2010) 37 [arXiv:0912.3800 [hep-ph]].

[31] P. Maris and C. D. Roberts, "Dyson-Schwinger equations: A tool for hadron physics," Int. J. Mod. Phys. E **12** (2003) 297 [arXiv:nucl-th/0301049].

[32] R. Alkofer and L. von Smekal, "The infrared behavior of QCD Green's functions: Confinement, dynamical symmetry breaking, and hadrons as relativistic bound states," Phys. Rept. **353** (2001) 281 [arXiv:hep-ph/0007355].

[33] C. S. Fischer, "Infrared properties of QCD from Dyson-Schwinger equations," J. Phys. G **32** (2006) R253 [arXiv:hep-ph/0605173] and references therein.

[34] C. S. Fischer, A. Maas and J. M. Pawlowski, "On the infrared behavior of Landau gauge Yang-Mills theory," Annals Phys. **324** (2009) 2408 [arXiv:0810.1987 [hep-ph]].

[35] M. T. Strickland, "Dynamical mass generation and confinement at finite temperature,"

[36] C. D. Roberts and S. M. Schmidt, "Dyson-Schwinger equations: Density, temperature and continuum strong QCD," Prog. Part. Nucl. Phys. **45** (2000) S1 [arXiv:nucl-th/0005064].

[37] M. Blank and A. Krassnigg, "The QCD chiral transition temperature in a Dyson-Schwinger-equation context," Phys. Rev. D **82** (2010) 034006 [arXiv:1004.5301 [hep-ph]].

[38] F. Karsch and M. Kitazawa, "Spectral properties of quarks above T_c in quenched lattice QCD," Phys. Lett. B **658** (2007) 45 [arXiv:0708.0299 [hep-lat]].

[39] F. Karsch and M. Kitazawa, "Quark propagator at finite temperature and finite momentum in quenched lattice QCD," Phys. Rev. D **80** (2009) 056001 [arXiv:0906.3941 [hep-lat]].

[40] C. S. Fischer, A. Maas and J. A. Muller, "Chiral and deconfinement transition from correlation functions: SU(2) vs. SU(3)," Eur. Phys. J. C **68** (2010) 165 [arXiv:1003.1960 [hep-ph]].

[41] C. S. Fischer and J. A. Mueller, "Chiral and deconfinement transition from Dyson-Schwinger equations," Phys. Rev. D **80** (2009) 074029 [arXiv:0908.0007 [hep-ph]].

[42] J. A. Mueller, C. S. Fischer and D. Nickel, "Quark spectral properties above Tc from Dyson-Schwinger equations," arXiv:1009.3762 [hep-ph].

[43] C. Vafa and E. Witten, "Restrictions On Symmetry Breaking In Vector-Like Gauge Theories," Nucl. Phys. B **234** (1984) 173.

[44] V. P. Nair, "Quantum field theory: A modern perspective," *New York, USA: Springer (2005) 557 p*

[45] T. Kugo and I. Ojima, "Local Covariant Operator Formalism Of Nonabelian Gauge Theories And Quark Confinement Problem," Prog. Theor. Phys. Suppl. **66** (1979) 1.

[46] T. Kugo, "The universal renormalization factors Z(1) / Z(3) and color confinement condition in non-Abelian gauge theory," arXiv:hep-th/9511033.

[47] C. DeTar and U. M. Heller, "QCD Thermodynamics from the Lattice," Eur. Phys. J. A **41** (2009) 405 [arXiv:0905.2949 [hep-lat]].

[48] S. Ejiri *et al.*, "On the magnetic equation of state in (2+1)-flavor QCD," Phys. Rev. D **80** (2009) 094505 [arXiv:0909.5122 [hep-lat]].

[49] R. D. Pisarski and F. Wilczek, "Remarks On The Chiral Phase Transition In Chromodynamics," Phys. Rev. D **29** (1984) 338.

[50] C. Schmidt, F. Karsch and E. Laermann, "The chiral critical point in 3-flavour QCD," Nucl. Phys. Proc. Suppl. **106** (2002) 423 [arXiv:hep-lat/0110039].

[51] C. Bonati, G. Cossu, M. D'Elia, A. Di Giacomo and C. Pica, "The order of the QCD transition with two light flavors," Nucl. Phys. A **820** (2009) 243C.

[52] A. Ukawa, "QCD PHASE TRANSITIONS AT FINITE TEMPERATURES," Nucl. Phys. Proc. Suppl. **17** (1990) 118 and references therein.

[53] J. Engels, F. Karsch, H. Satz and I. Montvay, "High Temperature SU(2) Gluon Matter On The Lattice," Phys. Lett. B **101** (1981) 89.

[54] J. Kuti, J. Polonyi and K. Szlachanyi, "Monte Carlo Study Of SU(2) Gauge Theory At Finite Temperature," Phys. Lett. B **98** (1981) 199.

[55] L. D. McLerran and B. Svetitsky, "A Monte Carlo Study Of SU(2) Yang-Mills Theory At Finite Temperature," Phys. Lett. B **98** (1981) 195.

[56] A. Roberge and N. Weiss, "GAUGE THEORIES WITH IMAGINARY CHEMICAL POTENTIAL AND THE PHASES OF QCD," Nucl. Phys. B **275** (1986) 734;

[57] A. Cucchieri, A. Maas and T. Mendes, "Exploratory study of three-point Green's functions in Landau-gauge Yang-Mills theory," Phys. Rev. D **74**, (2006) 014503 [arXiv:hep-lat/0605011].

[58] J. J. Rusnak and R. J. Furnstahl, "Two point fermion correlation functions at finite density," Z. Phys. A **352** (1995) 345.

[59] D. Zwanziger, "Vanishing of zero momentum lattice gluon propagator and color confinement," Nucl. Phys. B **364** (1991) 127.

[60] D. Zwanziger, "Renormalizability of the critical limit of lattice gauge theory by BRS invariance," Nucl. Phys. B **399** (1993) 477.

[61] A. Maas, J. Wambach, B. Grüter and R. Alkofer, "High-Temperature Limit of Landau-Gauge Yang-Mills Theory," Eur. Phys. J. C **37**, No.3, (2004) 335 [arXiv:hep-ph/0408074].

[62] A. Maas, J. Wambach and R. Alkofer, "The high-temperature phase of Landau-gauge Yang-Mills theory," Eur. Phys. J. C **42**, (2005) 93 [arXiv:hep-ph/0504019].

[63] A. Cucchieri, A. Maas and T. Mendes, "Infrared properties of propagators in Landau-gauge pure Yang-Mills theory at finite temperature," Phys. Rev. D **75** (2007) 076003 [arXiv:hep-lat/0702022].

[64] K. Lichtenegger and D. Zwanziger, "Nonperturbative contributions to the QCD pressure," Phys. Rev. D **78** (2008) 034038 [arXiv:0805.3804 [hep-ph]].

[65] J. Skullerud and A. Kizilersu, "Quark-gluon vertex from lattice QCD," JHEP **0209** (2002) 013 [arXiv:hep-ph/0205318].

[66] J. I. Skullerud, P. O. Bowman, A. Kizilersu, D. B. Leinweber and A. G. Williams, "Nonperturbative structure of the quark gluon vertex," JHEP **0304** (2003) 047 [arXiv:hep-ph/0303176].

[67] H. W. Lin, "Quark-gluon vertex with an off-shell O(a)-improved chiral fermion action," Phys. Rev. D **73** (2006) 094511 [arXiv:hep-lat/0510110].

[68] A. Kizilersu, D. B. Leinweber, J. I. Skullerud and A. G. Williams, "Quark-gluon vertex in general kinematics," Eur. Phys. J. C **50** (2007) 871 [arXiv:hep-lat/0610078].

[69] R. Alkofer, C. S. Fischer, F. J. Llanes-Estrada and K. Schwenzer, "The quark-gluon vertex in Landau gauge QCD: Its role in dynamical chiral symmetry breaking and quark confinement," Annals Phys. **324** (2009) 106 [arXiv:0804.3042 [hep-ph]].

[70] F. J. Llanes-Estrada, C. S. Fischer and R. Alkofer, "Semiperturbative construction for the quark gluon vertex," Nucl. Phys. Proc. Suppl. **152** (2006) 43 [arXiv:hep-ph/0407332].

[71] C. S. Fischer, F. J. Llanes-Estrada and R. Alkofer, "Dynamical mass generation in Landau gauge QCD," Nucl. Phys. Proc. Suppl. **141** (2005) 128 [arXiv:hep-ph/0407294].

[72] H. D. Politzer, "Effective Quark Masses In The Chiral Limit," Nucl. Phys. B **117** (1976) 397.

[73] V. A. Miransky, "ON DYNAMICAL CHIRAL SYMMETRY BREAKING," Phys. Lett. B **165** (1985) 401.

[74] J. S. Ball and T. W. Chiu, "Analytic Properties Of The Vertex Function In Gauge Theories. 1," Phys. Rev. D **22** (1980) 2542.

[75] M. Le Bellac, *Thermal Field Theory*. Cambridge University Press, Cambridge 1996.

[76] P. Maris, C. D. Roberts and P. C. Tandy, "Pion mass and decay constant," Phys. Lett. B **420** (1998) 267 [arXiv:nucl-th/9707003].

[77] J. Braun, H. Gies and J. M. Pawlowski, "Quark Confinement from Color Confinement," Phys. Lett. B **684**, (2010) 262 [arXiv:0708.2413 [hep-th]];

[78] F. Marhauser and J. M. Pawlowski, "Confinement in Polyakov Gauge," arXiv:0812.1144 [hep-ph].

[79] A. Bender, D. Blaschke, Y. Kalinovsky and C. D. Roberts, "Continuum study of deconfinement at finite temperature," Phys. Rev. Lett. **77** (1996) 3724 [arXiv:nucl-th/9606006].

[80] C. Gattringer, "Linking confinement to spectral properties of the Dirac operator," Phys. Rev. Lett. **97**, (2006) 032003 [arXiv:hep-lat/0605018].

[81] F. Bruckmann, C. Gattringer and C. Hagen, "Complete spectra of the Dirac operator and their relation to confinement," Phys. Lett. B **647**, (2007) 56 [arXiv:hep-lat/0612020].

[82] F. Synatschke, A. Wipf and C. Wozar, "Spectral sums of the Dirac-Wilson operator and their relation to the Polyakov loop," Phys. Rev. D **75**, (2007) 114003 [arXiv:hep-lat/0703018].

[83] F. Synatschke, A. Wipf and K. Langfeld, "Relation between chiral symmetry breaking and confinement in YM-theories," Phys. Rev. D **77**, (2008) 114018 [arXiv:0803.0271 [hep-lat]].

[84] E. Bilgici, F. Bruckmann, C. Gattringer and C. Hagen, "Dual quark condensate and dressed Polyakov loops," Phys. Rev. D **77**, (2008) 094007 [arXiv:0801.4051 [hep-lat]].

[85] C. S. Fischer, "Deconfinement phase transition and the quark condensate," Phys. Rev. Lett. **103** (2009) 052003 [arXiv:0904.2700 [hep-ph]].

[86] J. Braun, L. M. Haas, F. Marhauser and J. M. Pawlowski, "On the relation of quark confinement and chiral symmetry breaking," arXiv:0908.0008 [hep-ph].

[87] B. J. Schaefer and J. Wambach, "Renormalization group approach towards the QCD phase diagram," Phys. Part. Nucl. **39**, (2008) 1025 [arXiv:hep-ph/0611191];

[88] H. Gies, "Introduction to the functional RG and applications to gauge theories," arXiv:hep-ph/0611146;

[89] J. M. Pawlowski, "Aspects of the functional renormalisation group," Annals Phys. **322**, (2007) 2831 [arXiv:hep-th/0512261].

[90] E. Bilgici and C. Gattringer, "Static quark-antiquark potential and Dirac eigenvector correlators," JHEP **0805**, (2008) 030 [arXiv:0803.1127 [hep-lat]].

[91] A. M. Polyakov, "Thermal Properties Of Gauge Fields And Quark Liberation," Phys. Lett. B **72** (1978) 477.

[92] L. Susskind, "Lattice Models Of Quark Confinement At High Temperature," Phys. Rev. D **20** (1979) 2610.

[93] F. Bruckmann, C. Hagen, E. Bilgici and C. Gattringer, "Dual condensate, dressed Polyakov loops and center symmetry from Dirac spectra," PoS **LATTICE2008**, (2008) 262 [arXiv:0810.0899 [hep-lat]].

[94] J. Danzer, C. Gattringer and A. Maas, "Chiral symmetry and spectral properties of the Dirac operator in G2 Yang-Mills Theory," JHEP **0901**, (2009) 024 [arXiv:0810.3973 [hep-lat]].

[95] R. Williams, C. S. Fischer and M. R. Pennington, "anti-q q condensate for light quarks beyond the chiral limit," Phys. Lett. B **645** (2007) 167 [arXiv:hep-ph/0612061].

[96] J. M. Cornwall, R. Jackiw and E. Tomboulis, "Effective Action For Composite Operators," Phys. Rev. D **10** (1974) 2428.

[97] C. S. Fischer and R. Williams, "Beyond the rainbow: effects from pion backcoupling," Phys. Rev. D **78** (2008) 074006, [arXiv:0808.3372 [hep-ph]].

[98] P. V. Buividovich, E. V. Luschevskaya and M. I. Polikarpov, "Finite-temperature chiral condensate and low-lying Dirac eigenvalues in quenched SU(2) lattice gauge theory," Phys. Rev. D **78** (2008) 074505 [arXiv:0809.3075 [hep-lat]].

[99] B. Muller and J. L. Nagle, "Results from the Relativistic Heavy Ion Collider," Ann. Rev. Nucl. Part. Sci. **56**, 93 (2006) [arXiv:nucl-th/0602029].

[100] E. Shuryak, "Physics of Strongly coupled Quark-Gluon Plasma," Prog. Part. Nucl. Phys. **62**, 48 (2009) [arXiv:0807.3033 [hep-ph]].

[101] P. Braun-Munzinger and J. Wambach, "Colloquium: Phase diagram of strongly interacting matter," Rev. Mod. Phys. **81**, 1031 (2009).

[102] U. W. Heinz, "Early collective expansion: Relativistic hydrodynamics and the transport properties of QCD matter," arXiv:0901.4355 [nucl-th].

[103] D. Molnar and S. A. Voloshin, "Elliptic flow at large transverse momenta from quark coalescence," Phys. Rev. Lett. **91**, 092301 (2003) [arXiv:nucl-th/0302014].

[104] R. Schulze, M. Bluhm and B. Kampfer, "Plasmons, plasminos and Landau damping in a quasiparticle model of the quark-gluon plasma," Eur. Phys. J. ST **155** (2008) 177 [arXiv:0709.2262 [hep-ph]];

[105] M. Bluhm and B. Kampfer, "Flavor Diagonal and Off-Diagonal Susceptibilities in a Quasiparticle Model of the Quark-Gluon Plasma," Phys. Rev. D **77** (2008) 114016 [arXiv:0801.4147 [hep-ph]].

[106] W. Cassing, "QCD thermodynamics and confinement from a dynamical quasiparticle point of view," Nucl. Phys. A **791**, 365 (2007) [arXiv:0704.1410 [nucl-th]].

[107] W. Cassing and E. L. Bratkovskaya, "Parton transport and hadronization from the dynamical quasiparticle point of view," Phys. Rev. C **78**, 034919 (2008) [arXiv:0808.0022 [hep-ph]].

[108] E. Braaten, R. D. Pisarski and T. C. Yuan, "Production Of Soft Dileptons In The Quark - Gluon Plasma," Phys. Rev. Lett. **64** (1990) 2242.

[109] A. Peshier and M. H. Thoma, "Quark dispersion relation and dilepton production in the quark-gluon plasma," Phys. Rev. Lett. **84**, 841 (2000) [arXiv:hep-ph/9907268].

[110] P. B. Arnold, G. D. Moore and L. G. Yaffe, "Photon and Gluon Emission in Relativistic Plasmas," JHEP **0206**, 030 (2002) [arXiv:hep-ph/0204343];

[111] P. B. Arnold, G. D. Moore and L. G. Yaffe, "Photon emission from quark gluon plasma: Complete leading order results," JHEP **0112**, 009 (2001) [arXiv:hep-ph/0111107].

[112] D. Nickel, "Extraction of spectral functions from Dyson-Schwinger studies via the maximum entropy method," Annals Phys. **322** (2007) 1949 [arXiv:hep-ph/0607224].

[113] R. Alkofer, W. Detmold, C. S. Fischer and P. Maris, "Analytic properties of the Landau gauge gluon and quark propagators," Phys. Rev. D **70** (2004) 014014 [arXiv:hep-ph/0309077];

[114] R. Alkofer, W. Detmold, C. S. Fischer and P. Maris, "Analytic structure of the gluon and quark propagators in Landau gauge QCD," Nucl. Phys. Proc. Suppl. **141** (2005) 122 [arXiv:hep-ph/0309078].

[115] S. x. Qin, L. Chang, Y. x. Liu and C. D. Roberts, "Quark spectral density and a strongly-coupled QGP," arXiv:1010.4231 [nucl-th].

[116] D. Nickel, J. Wambach and R. Alkofer, "Color-superconductivity in the strong-coupling regime of Landau gauge QCD," Phys. Rev. D **73** (2006) 114028 [arXiv:hep-ph/0603163].

[117] D. Nickel, R. Alkofer and J. Wambach, "On the unlocking of color and flavor in color-superconducting quark matter," Phys. Rev. D **74** (2006) 114015 [arXiv:hep-ph/0609198].

[118] D. Nickel, *Color-superconductivity from a Dyson-Schwinger perspective*. PhD thesis, Technische Universität Darmstadt, 2007.

[119] F. Karsch, "Lattice QCD at high temperature and density," Lect. Notes Phys. **583** (2002) 209 [arXiv:hep-lat/0106019].

[120] F. Karsch, E. Laermann and A. Peikert, "Quark mass and flavor dependence of the QCD phase transition," Nucl. Phys. B **605** (2001) 579 [arXiv:hep-lat/0012023].

[121] A. Ali Khan *et al.* [CP-PACS Collaboration], "Phase structure and critical temperature of two flavor QCD with renormalization group improved gauge action and clover improved Wilson quark action," Phys. Rev. D **63** (2001) 034502 [arXiv:hep-lat/0008011].

[122] M. Alford, J. Berges and J. M. Cheyne, "Critical phenomena from the two-particle irreducible 1/N expansion," Phys. Rev. D **70**, 125002 (2004) [arXiv:hep-ph/0404059].

[123] F. Marhauser, *Confinement in Polyakov gauge and the QCD phase diagram*. PhD thesis (see Appendix B), Ruperto-Carola University of Heidelberg, 2009.

[124] C. S. Fischer, D. Nickel and J. Wambach, "Hadronic unquenching effects in the quark propagator," Phys. Rev. D **76** (2007) 094009 [arXiv:0705.4407 [hep-ph]].

[125] W. J. Marciano and H. Pagels, "Quantum Chromodynamics: A Review," Phys. Rept. **36** (1978) 137.

[126] R. D. Pisarski and M. Tytgat, "Propagation of Cool Pions," Phys. Rev. D **54** (1996) 2989 [arXiv:hep-ph/9604404].

[127] D. T. Son and M. A. Stephanov, "Pion propagation near the QCD chiral phase transition," Phys. Rev. Lett. **88** (2002) 202302 [arXiv:hep-ph/0111100].

[128] G. A. . Baker, B. G. Nickel and D. I. Meiron, "Critical Indices From Perturbation Analysis Of The Callan-Symanzik Phys. Rev. B **17** (1978) 1365.

[129] K. Rajagopal and F. Wilczek, "Static and dynamic critical phenomena at a second order QCD phase transition," Nucl. Phys. B **399** (1993) 395 [arXiv:hep-ph/9210253].

[130] O. Bohr, B. J. Schaefer and J. Wambach, "Renormalization group flow equations and the phase transition in O(N) models," Int. J. Mod. Phys. A **16**, 3823 (2001) [arXiv:hep-ph/0007098].

[131] C. D. Roberts and A. G. Williams, "Dyson-Schwinger equations and their application to hadronic physics," Prog. Part. Nucl. Phys. **33** (1994) 477 [arXiv:hep-ph/9403224].

[132] M. Galassi et al, *GNU Scientific Library Reference Manual* (3rd Ed.), ISBN 0954612078.

Lebenslauf

Name	Jens Andreas Müller
Geburtsdatum	03. Mai 1980
Geburtsort	Ottweiler
Staatsangehörigkeit	Deutsch
Familienstand	Ledig

08/2007 -	Wissenschaftlicher Mitarbeiter am Institut für Kernphysik an der Universität Darmstadt
04/2007	Diplom an der Universität Heidelberg; Gesamturteil: sehr gut
08/2003 - 06/2004	Erasmus Stipendiat an der Universität Uppsala *Degree of Master of Science* der Universität Uppsala, Nov 2004
09/2000 - 04/2007	Studium der Physik an der Universität Heidelberg Vordiplom, Oktober 2002; Gesamturteil: sehr gut
07/1999 - 06/2000	Zivildienst
1999	Schüler am Saarpfalz-Gymnasium Homburg Abschluss: allgemeine Hochschulreife